FUV Spectroscopy of Interstellar and Circumstellar Material

by

Eric Robert Schindhelm

B.S., Physics, University of Maryland, 2003

B.S., Astronomy, University of Maryland, 2003

M.S., Astrophysics, University of Colorado, 2005

A thesis submitted to the

Faculty of the Graduate School of the

University of Colorado in partial fulfillment

of the requirements for the degree of

Doctor of Philosophy

Department of Astrophysical and Planetary Sciences

2011

This thesis entitled:
FUV Spectroscopy of Interstellar and Circumstellar Material
written by Eric Robert Schindhelm
has been approved for the Department of Astrophysical and Planetary Sciences

_____

Prof. James C. Green

_____

Dr. Matthew Beasley

_____

Dr. Kevin France

Date _____

The final copy of this thesis has been examined by the signatories, and we find that both the content and the form meet acceptable presentation standards of scholarly work in the above mentioned discipline.

Schindhelm, Eric Robert (Ph.D., Astrophysical and Planetary Sciences)

FUV Spectroscopy of Interstellar and Circumstellar Material

Thesis directed by   Prof. James C. Green

I have designed, assembled, and calibrated a sounding rocket payload to perform high-resolution FUV spectroscropy. Debate lingers over the existence of a pervasive 1 million K gas in our region of the interstellar medium, the Local Bubble. If this hot gas were present, it would produce O VI upon interacting with the cold cavity wall. As such, O VI serves as a diagnostic for the hot interstellar gas. I designed the Diffuse Interstellar Cloud Experiment (DICE) to measure the O VI (1032,1038 Angstrom) doublet in absorption against two stars on either side of the Local Bubble wall. The instrument is functionally a Cassegrain telescope followed by a modified Rowland-mount spectrograph. With a holographically-ruled grating and a secondary magnifying optic, the spectrograph can achieve high resolving power (R=60,000) in a compact space.

In addition, I have analyzed Carbon Monoxide (CO) emission from Classical T-Tauri star disks using spectra from the HST-Cosmic Origins Spectrograph. The CO is photo-excited by Lyman alpha from the magnetospheric shock. I model this incident Lyman alpha radiation to use as input for a simple CO fluorescence model. Fits to the data constrain CO temperatures and column densities, which can then be compared with other known properties of the disks in our target sample. I find no correlation between this UV-emitting CO and the CO studied at infrared and sub-mm wavelengths between targets.

Dedication

"Though I had success in my research both when I was mad and when I was not, eventually I felt that my work would be better respected if I thought and acted like a 'normal' person."

-John Forbes Nash

For my family and friends, who supported and inspired me along the way.

Acknowledgements

It takes a village to raise a graduate student, and I was no exception. First, I thank my advisors/bosses over the years - Jim, Matt, Kevin, and Web - the quality of your guidance was matched only by your patience. I learned far more than just rocket science. Thanks to each of you for the educational and moral support. You all gave me great opportunities, and I for one would like to believe they were not squandered.

Many brilliant people put countless hours into DICE I and II, for which I am grateful. Bobby Kane mastered Solidworks and pumped out models and drawings like a boss. The Hodgsons, Marty Gould, and the JILA machinists made the DICE structure a reality. Eric Burgh's expertise was "instrumental" during round 2, particularly with the optical alignments. The teams at Wallops and White Sands worked like pros to get everything off the ground. Michael PD Kaiser, Sarah LeVine, Thomas Rogers, Brennan Gantner, Nico Nell, Scott MacDonald, and the other undergraduates did what they must so many times. You guys really made things fun, thank you all.

I'd like to acknowledge NASA for its support of the rocket and my salary over the years. Thank you also to Alex Brown and Greg Herczeg for saving my behind with über-awesome data.

Many helped in non-work-related ways. I thank my parents and Steph for coming out to Boulder when I needed them most. Grandpa Braun, you got me interested in this subject; I hope I've done you proud. Jamie, Nick, Randy, Ted, Steve, and Thomas - thanks for making life outside the lab entertaining. I have been and always shall be your friend.

Again, I thank the lovely Sarah Anne LeVine. You've been so patient and supportive; thanks for keeping me smiling and grounded in reality. You are precious to me.

Contents

Chapter

Appendix

Tables

Table

Figures

Figure

Chapter 1

Introduction

People who like this sort of thing will find this the sort of thing they like.

-Abraham Lincoln

The interstellar medium (ISM) comprises the vast expanse of gas and dust throughout our Milky Way galaxy. It is a complex distribution of matter and energy which we are only beginning to truly understand. The ISM plays an important role in the evolution of galaxies; in it stars are born, live out their lives, and eventually die. Throughout this process material evolves between many phases and is reprocessed along the way. Gas and dust congregate in large molecular clouds to form stars. Heavy elements are fused at their centers, to be later expelled back into the ISM at the end of their lives. Highly energetic supernovae spread energy throughout the ISM, compressing the tenuous material back into clouds to continue the cycle. This thesis focuses on the use of far-ultraviolet spectroscopy to understand the dynamics and composition of ISM gas. An overview of the different phases of the ISM is given in §1.1. The local region of the ISM is explored in §1.2, as well as the debate over whether or not it contains any hot gas. Lastly, §1.3 describes the warm gas in the disks of forming planetary systems.

1.1   The Phases of the Interstellar Medium

The current paradigm of the ISM includes 3 phases: cold gas (molecular and diffuse HI clouds, $T \approx 10-100$ K, $n_H \geq 100$ cm^{-3}), warm and partially ionized intercloud gas ($T \approx 10^4$ - 10^5 K, $n_H \approx 0.1$ cm^{-3}), and a tenuous hot coronal component ($T \approx 10^5$ - 10^6 K, $n_H \leq 0.001$ cm^{-3}) (Cox, 2005).

The combination of *Hipparcos*'s accurate distance measurements to nearby stars (Perryman et al., 1997), and high spectral resolution measurements of absorption and emission lines towards those stars, has painted a detailed picture of the local ISM. Many models of the ISM assume that these phases are in pressure equilibrium (Wolfire et al., 1995). However, supernovae and stellar winds from young stars are capable of disrupting such an equilibrium. In addition, there are disagreements by as much as a factor of 2 between the modeled and measured thermal pressure (Jenkins, 2002). The dynamics of ISM gas have a strong influence on everything from star formation and stellar composition, to the structure of the Milky Way's disk, to the size of our heliosphere. It is therefore crucial to understand the interplay between the different ISM phases. While the turbulent nature of the ISM is still being characterized, the simplified three-phase model serves as a sufficient starting point to describe the overall properties of these phases.

The cold phase, or cold neutral medium (CNM), is comprised of neutral atoms, molecular gas, and dust. This gas typically resides in large diffuse clouds, or gravitationally collapsing molecular clouds. Molecular clouds form when diffuse ISM gas is swept up by supernova blast waves, or compressed by running into the Milky Way's spiral density waves. Shielded from the interstellar radiation field by gas and dust, clumps of these clouds collapse even further to form stars, such as in the molecular cloud in Figure 1.1. Reaching sizes as large as hundreds of light years across, these clouds still only fill 1-5% of the Milky Way disk's total volume, but make up most of its non-stellar baryonic mass. H I 21 cm emission and absorption line surveys have mapped out the CNM within our neighborhood of the Milky Way. Inside the solar circle, $r \sim 8.5$ kpc, approximately half the gas is molecular, while H I and H II regions have been detected as far away as 20 kpc (Snell et al., 2002; Kobayashi & Tokunaga, 2000).

A wall of cold, dense material appears to bound the immediate region of the ISM, the Local Interstellar Medium (LISM). This was first inferred by starlight reddening measurements, demonstrating we are in an underdense region of the ISM (Fitzgerald, 1968). More recent observations and analysis have revealed the LISM's detailed structure. Along sightlines to nearby stars, ground-based observations measured absorption of neutral sodium (Na I), an element abundant in cool gas

Figure 1.1: This cold molecular cloud, enshrouded in the warm diffuse ISM, is being evaporated by the nearby already formed stars in M16 (Hester et al. 1996). n_H is on the order of 10^3 cm^{-3}.

(Sfeir et al., 1999; Lallement et al., 2003). Out to 100 parsecs (pc) from the Sun in most directions Na I is barely present (N(NaI) $\leq 10^{12}$ cm^{-2}), but beyond this distance it appears strongly in absorption. Thus, the Sun is in an underdense cavity in the ISM, dubbed the 'Local Cavity' (LC), and shown in Figure 1.2. Models suggest that a series of supernova explosions could have carved this cavity out of the ambient galactic medium millions of years ago (Fuchs et al., 2006). Winds from OB associations could also have contributed to the expansion. Inside the LC cold clouds are rare (filling factor $\leq 1\%$, although some have been detected with the H I 21 cm line and CO emission (Heiles & Troland, 2003; Chol Minh et al., 2003).

The warm phase, or warm neutral medium (WNM), is predominantly heated by stellar UV radiation (Watson, 1972) and can be co-spatial with the CNM or spread throughout the ISM. Some of the neutral HI in the ISM is warm, and measured in absorption. The other WNM component is neutral and ionized gas, which is generally contained in diffuse clouds. The Sun currently resides in a transition region between two such clouds, the Local Interstellar Cloud and the G cloud (in the direction of the galactic center). As with the CNM, these clouds can be detected in absorption against background stars. The majority of resonance lines of WNM tracers (O I, C II (C$^+$), Si II, N II, etc.) in the interstellar medium fall in the UV, and thus space-based measurements are necessary. Between the Goddard High Resolution Spectrograph (GHRS) and the Space Telescope Imaging Spectrograph (STIS) onboard the *Hubble Space Telescope (HST)*, and the *Far Ultraviolet Spectroscopic Explorer (FUSE)*, sightlines to over 150 stars have been observed (Redfield, 2009). Almost 300 velocity components have been measured within 100 pc of our Sun. An all-sky projection map of these is shown in Figure 1.3.

Through the measurement of multiple ions in these clouds, the physical conditions of the gas have been determined, including the temperature, turbulence, electron and volume density, as well as depletion and ionization factors. Most of the velocity components can generally be traced to the Scorpio-Centaurus stellar association (Frisch et al., 2002). Dynamical models of WNM clouds estimate the average temperatures of these clouds to be between 5300 and 9900 K, with a filling factor of approximately 5-20%. These models are based on typical cloud sizes around a few pc,
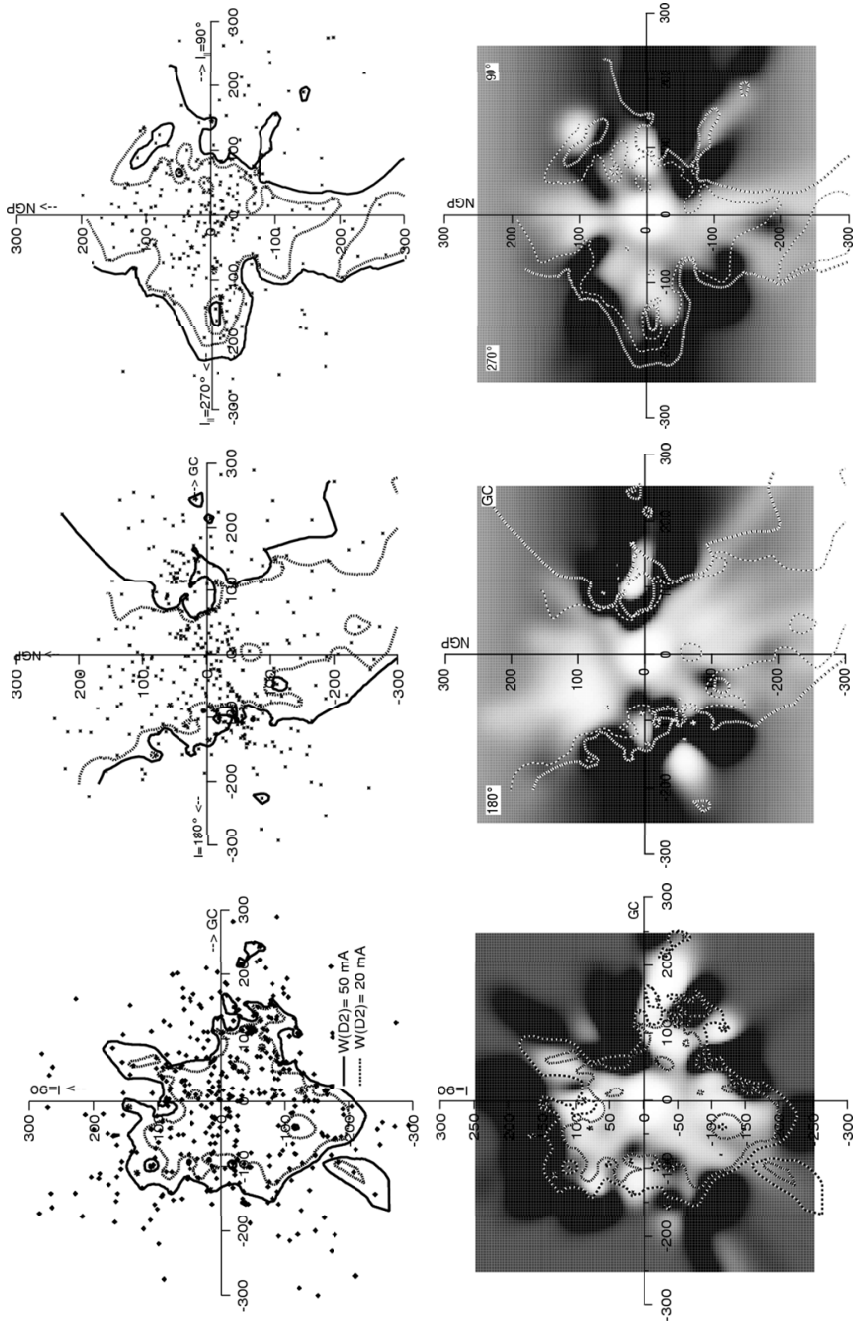
Figure 1.2: Density maps of the LC. The top row shows contours of NaI absorption equivalent widths (in mÅ) in many stellar sightlines. The distance scale is in parsecs. The bottom row shows density maps by converting higher equivalent widths into higher density, where darker shading corresponds to higher cold gas density. The left two column shows a cut of the galactic plane, while the other two columns show cuts perpendicular to the galactic plane. In all figures GC indicates the direction to the Galactic Center, and NGP indicates the direction to the North Galactic Pole Figure from Lallement et al. (2003).
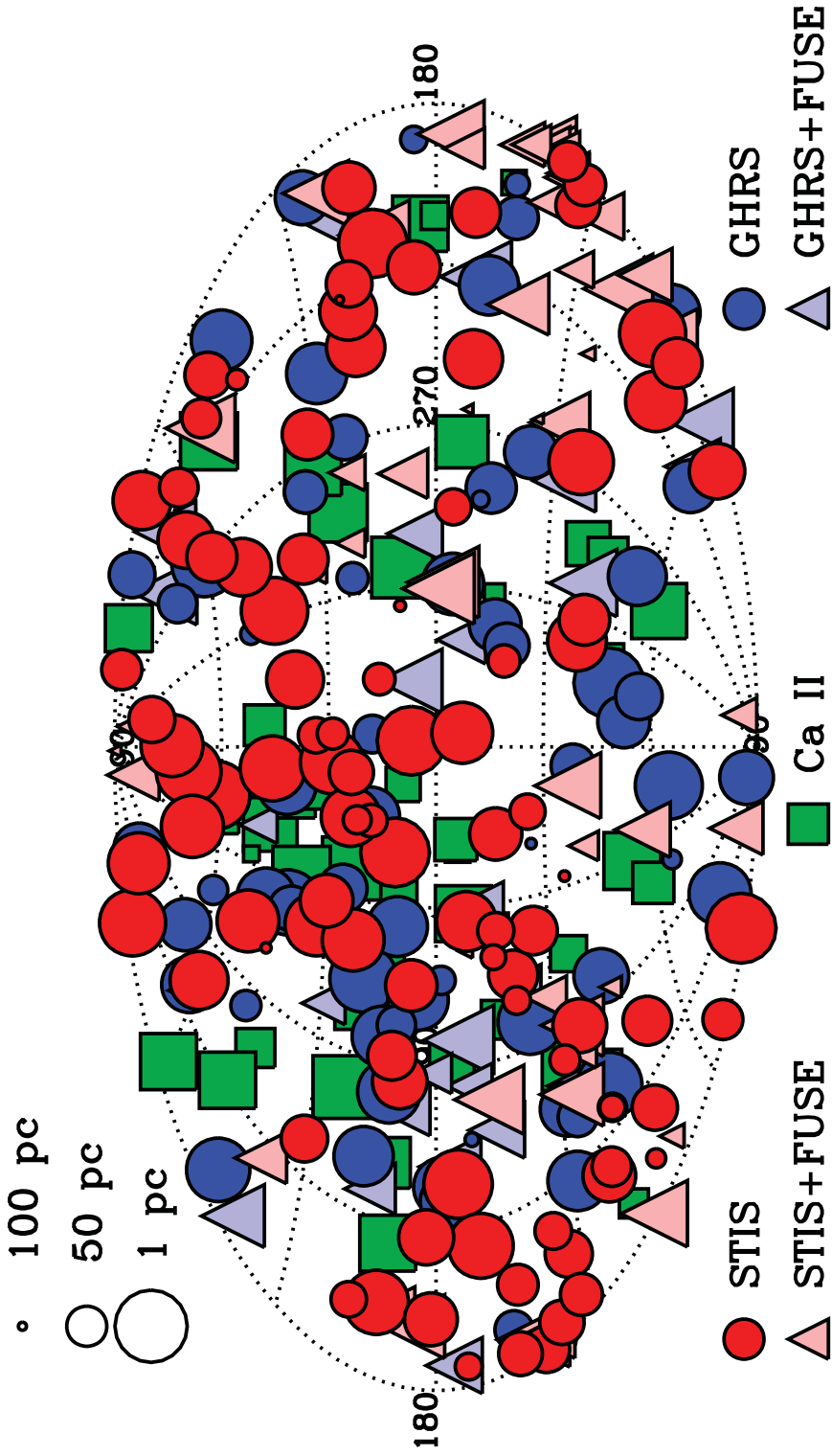
Figure 1.3: Each symbol represents a warm velocity component within 100 pc of the LISM, detected with *HST*-GHRS, *HST*-STIS, and FUSE. Ground-based Ca II measurements are shown as well. Symbol size identifies distance from Earth. Figure from Redfield (2009).

with ellipsoidal shapes. In reality, some clouds appear to be filamentary, although this would not significantly change the gas properties. While the bulk motion of the LISM clouds are similar, random differences between the individual clouds could cause collisions, self-shielding some gas from heating due to the interstellar radiation field. Such activity could be responsible for the few cold clouds detected in the LC (Redfield, 2009).

Finally, the hot phase of the LISM is perhaps the most controversial. Historically, it has been inferred from a diffuse soft X-ray background in the 1/4 keV band originating uniformly across the sky (McCammon & Sanders, 1990). Figure 1.4 shows the *Röntgen Satellite (ROSAT)* All Sky Survey from 0.1 to 0.9 keV. This emission has historically been interpreted as thermal bremsstrahlung radiation from a $T \approx 10^6$ K gas surrounding the solar system. The gas is presumably heated by supernovae and massive star winds. It can also be detected through absorption lines of high ionization atoms. Although its presence inside the LC has recently come under debate (see §1.2.1), strong evidence exists for the presence of such hot gas in nearby regions of the ISM, specifically the large Orion-Eridanus and Loop 1 superbubbles (Williamson et al., 1974; Berkhuijsen et al., 1971). These hot voids are separated from us by dense walls of cold gas, but provide solid evidence in favor of a hot ISM phase.

While the properties of each of these phases are individually understood, it is the combination of the three which is problematic. These phases must coexist throughout the galaxy in such a way to explain its overall properties. For example, pressure equilibrium must be maintained in the LISM in order to support the overlying galactic halo (Cox & Reynolds, 1987). However, there is an imbalance between the measured thermal pressures of the hot gas with the colder components (Snowden et al., 1993; Jenkins, 2002). This disagreement between observation and theory exists in many areas of galactic physics, requiring further investigation.

Understanding the composition and dynamics of the ISM is crucial to creating an accurate picture of how our Galaxy recycles and distributes energy and matter. Knowledge of the Milky Way's ISM can be applied to other galaxies in the Universe. Recent advances in spectral resolution and sensitivity throughout the UV band enable a more powerful exploration of the ISM. In this
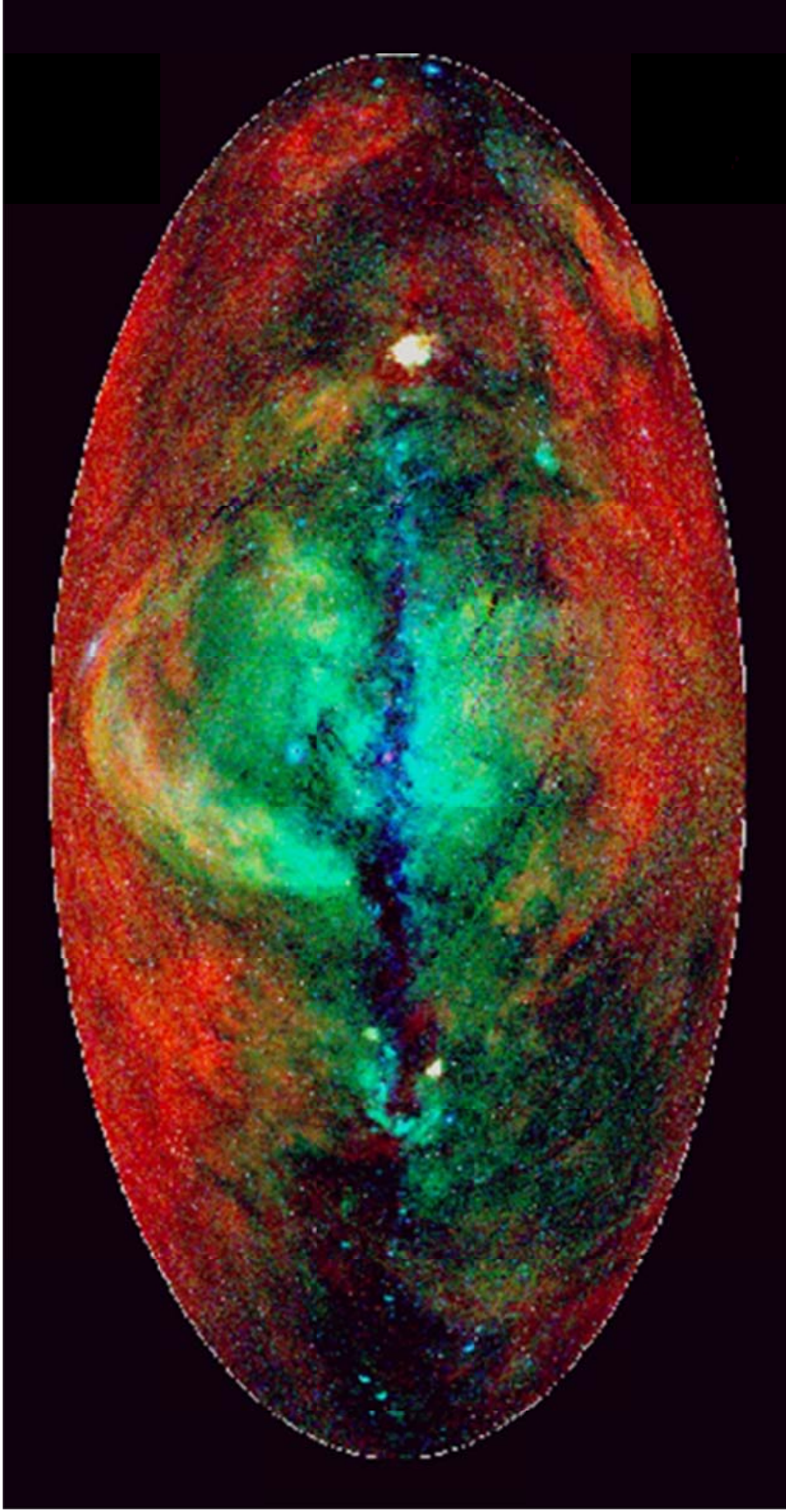
Figure 1.4: 3-color image of the ROSAT Soft X-ray Background All-Sky Survey. Red is 0.1-0.4 keV, green is 0.5-0.9 keV, and blue is 0.9 - 2.0 keV. Figure from Freyberg & Egger (1999).

thesis, I utilize two new instruments to explore two topics pertaining to these ISM phases: the debate over whether or not there is hot gas inside the LC, and the discovery of far ultraviolet Carbon Monoxide (CO) emission in the spectra of T Tauri stars. This encompasses the physical conditions of the LISM from the hottest, most tenuous gas, to the coldest, densest gas from which stars form.

1.2   On the Nature of the Local Bubble

As mentioned in the previous section, ubiquitous soft X-ray emission would seem to imply the existence of hot gas inside the LC. This diffuse soft X-ray emission was initially discovered through sounding rocket experiments (Bowyer et al., 1968; Henry et al., 1968). The emission was more or less isotropic, and was assumed to contain components from extra-galactic sources, the galactic halo, and gas inside the LC. The local contribution peaks around 1/4 keV, and was mapped out by comparing directional emission measurements with distances inside the LC (Snowden et al., 1998). The emission structure agreed with X-ray shadowing of interstellar clouds. This region seemed to be cospatial with the LC, which was being measured through Na I absorption lines at the time. Thus, the term 'Local Hot Bubble (LHB)' was coined, and became synonymous with the LC. Until the last decade, it has been the prevailing model for the LISM.

1.2.1   Controversies With the Hot Local Bubble Model

Recent evidence has brought the LHB model into question. *ROSAT* observations of the comet Hayakutake revealed X-ray emission, a result of charge exchange interactions between neutral cometary atoms and ions from the solar wind (Lisse et al., 1996; Cravens, 1997). This process, known as Solar Wind Charge Exchange (SWCX), prompted an investigation into the implications of such processes on the diffuse soft X-ray background. Temporal variances in the soft X-ray background emission, dubbed 'Long Term Enhancements', were indeed found in the *ROSAT* surveys (Cravens, 2000). When compared to solar proton flux, an impressive correlation appeared which was capable of explaining approximately 50% of the 1/4 keV emission (Cravens et al., 2001; Robertson

& Cravens, 2003), shown in Figure 1.5.

One major debate is over how much SWCX flux contributes to the soft X-ray emission background. More recent studies claim that all the 1/4 keV emission in the galactic disk can be accounted for by SWCX (Koutroumpa et al., 2009). In addition, SWCX models are capable of reproducing all the measured 3/4 keV emission, mostly from O VII (O^{6+}) and O VIII (Koutroumpa et al., 2007). However, not all SWCX models agree; some predict emission which differs in location and distribution from the observed emission (Robertson & Cravens, 2003). Thus there might still have to be some component due to hot gas in the disk LHB. All models agree that soft X-ray emission in the direction of the galactic halo cannot entirely be explained by SWCX (Koutroumpa et al., 2009). Still, these models require further refinement, complemented by higher spectral resolution measurements of diffuse X-ray emission.

Problems also arise when considering predicted emission at longer wavelengths. The measured extreme ultraviolet (EUV) continuum and line emission do not agree with LHB models. With the *Extreme Ultraviolet Explorer (EUVE)*, Jelinsky et al. (1995) and Vallerga & Slavin (1998) showed that the lack of line flux required Fe depletion or a non-collisional ionization equilibrium model. Results from the *Cosmic Hot Interstellar Plasma Spectrometer (CHIPS)* concurred, finding an emission measure much less than expected from a $T = 10^6$ K gas (Hurwitz et al., 2005). The data and model are shown in Figure 1.6. Assuming collisional ionization equilibrium, high depletion of specific high ionization state metals (such as Fe VIII and Fe IX) is required to match the measured spectrum. However, the Wisconsin group sounding rocket-borne measurements do not entirely agree with *EUVE* or *CHIPS* data (McCammon et al., 2002). Their calorimeter recorded more Fe IX emission than the other instruments, providing additional evidence in favor of the LHB model.

If SWCX accounts for the majority of the soft X-ray background, the required temperature for the hot diffuse gas would be lower. While in better agreement with the EUVE and CHIPS observations of EUV emission, a lower gas temperature could not explain the Wisconsin rocket measurements. However, it could solve the previously mentioned pressure equilibrium problems between the different ISM phases. These controversies must be resolved to have a complete model
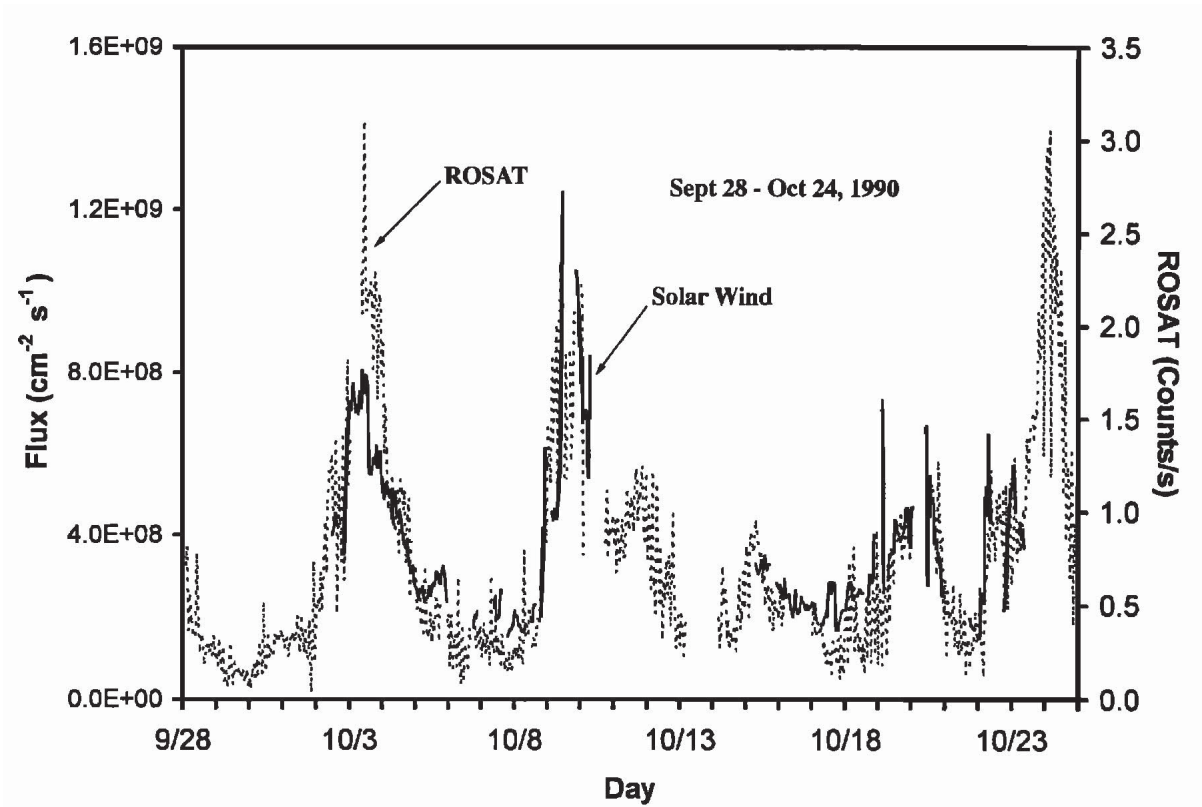
Figure 1.5: Evidence of correlation between 1/4 keV emission with heliospheric charge exchange reactions. Solar wind proton flux measured at 1 AU (solid line) plotted relatively over the *ROSAT* 1/4 keV long term enhancements. Figure from Cravens et al. (2001).
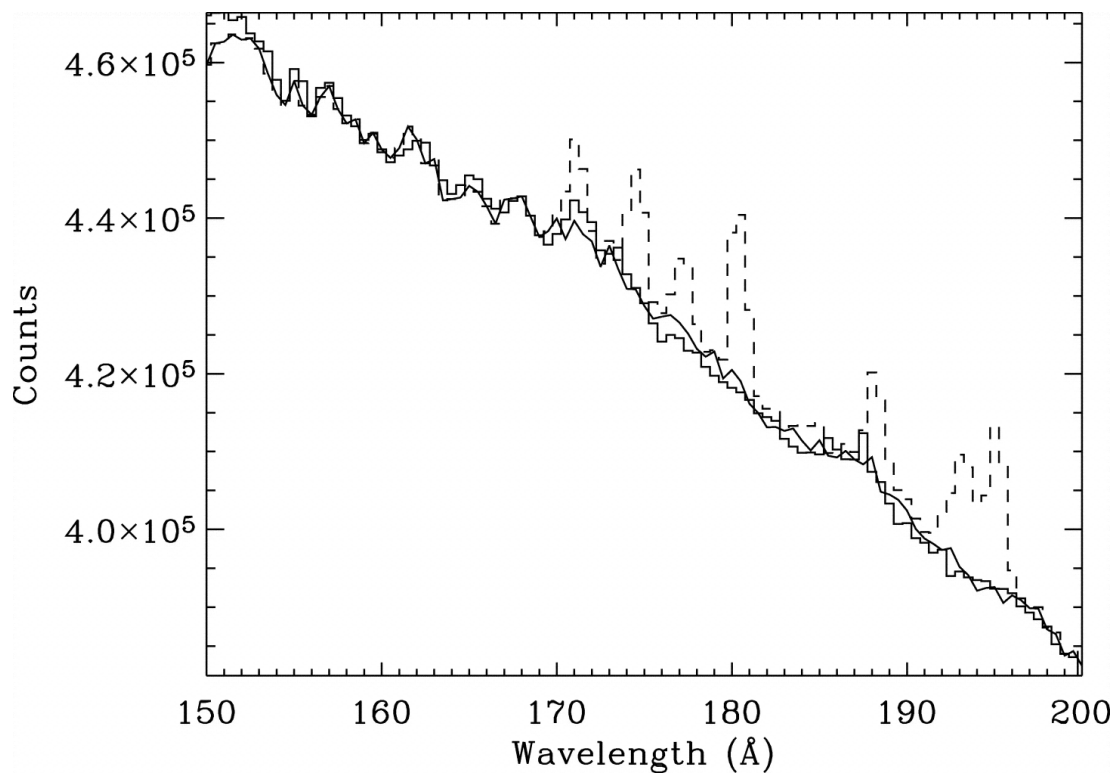
Figure 1.6: *CHIPS* spectrum (solid histogram), charged-particle background spectrum (solid line), and hot Local Bubble model emission (dashed histogram). The undetected lines would be expected from highly ionized Fe in a $T \sim 10^6$ K gas. Figure from Hurwitz et al. (2005).

of the LISM. Interstellar gas in the immediate solar neighborhood is easier and more reliable to study than that in the more distant ISM. It therefore provides a laboratory to test our ISM models, which can then be expanded to elsewhere in the Milky Way and to galaxies far far away.

1.2.2   O VI As a Probe of Hot Gas in the ISM

If there is a pervasive hot gas in the Local Bubble, an interface should exist between the cold and hot components of the ISM. An excellent way to study this boundary is to measure the absorption of O VI, a gas formed by collisional ionization at an intermediate temperature of $\sim 3x10^5$ K. These temperatures would be present in the interaction region between hot and cold gas. Early observations agreed with this model; surveys with *Copernicus* first mapped out the distribution of O VI in the LISM through its absorption towards nearby stars (Jenkins, 1978). In those data sets, no correlation was found between stellar and O VI radial velocities, implying that the O VI gas is likely interstellar, not circumstellar, in origin. Based on measured distances to the background stars at the time, it appeared that O VI, and hence far hotter gas, indeed resided within the LC.

Later analysis of the *Copernicus* data revealed complications and limitations in the methods of the original study. *Hipparcos*'s accurate distance measurements to nearby stars (Perryman et al., 1997) placed some of the O VI measurements outside the LC. Those that were within the LC were spread too randomly throughout to model exactly how the O VI was being formed. It was not until *FUSE* that more sensitive measurements were made of nearby white dwarfs (Oegerle et al., 2005; Savage & Lehner, 2006). White dwarf spectra are considerably cleaner than those of the early-type stars used in *Copernicus* surveys, free of many confusing contaminating features. With many more reliable sightlines to map the O VI, a number of positive detections were made.

The higher S/N FUSE spectra placed doubt on the assumption that the O VI was interstellar. A recent study by Barstow et al. (2009) analyzed *FUSE* observations of white dwarfs, including some from the Oegerle et al. (2005) survey. Using a newer version of the *FUSE* pipeline, they claimed that some O VI features disappeared entirely. For most targets, any O VI detected could be attributed to the stellar photospheres, and the only O VI detections in their study were located

outside the Local Bubble. Welsh & Lallement (2008) concurred; *FUSE* absorption spectra towards 17 early-type stars only inferred O VI above and below the Galactic disk ($+30° < b < $ -30°). Such results would imply that in the LISM, the Galactic plane is mostly devoid of O VI, and hence any hot gas.

Even with these higher accuracy measurements there is disagreement. Barstow et al. (2010) published analysis of a full sample of $\sim$80 *FUSE* white dwarfs. With this larger sample, they found no correlation between O VI detection and location in the galactic plane or halo as suggested by Welsh & Lallement (2008). Their distribution is shown in Figure 1.7. There is almost no O VI detected within the immediate 50 pc surrounding the sun; nearly all O VI detected is close to, or on the other side of, the cold LC wall as currently defined by Welsh et al. (2010). The interpretation is that a supernova remnant which evolves in a pre-existing cavity would expand and heat that material (Shelton, 1999; Fuchs et al., 2006), forming transition-temperature ions like N V and O VI at the cavity boundary. The cavity gas would soon cool, but leave behind some of these ions. This agrees with the model in which the immediate ISM is devoid of any hot gas, explaining why the many WNM clouds detailed in Redfield & Linsky (2008) do not exhibit any significant cospatial O VI. Further study of O VI at the LC wall can reveal the formation processes involved and put additional constraints on these models. Therefore, I designed a spectrograph to record high resolving power (R ($\lambda/\delta\lambda$) = 60,000) spectra of the O VI doublet (λ = 1032,1038 Å). I explain this in detail in Chapter 2.

1.3   Probing Star and Planet Formation with UV Spectroscopy

Stars form inside cold, dense molecular clouds. The initial conditions inside the parent molecular cloud determine everything from stellar mass and composition, to the nature of potential planetary systems. Models of stellar formation have advanced in the last decade, taking into account turbulence throughout the clouds (McKee & Ostriker, 2007). However, they are not fully capable of reproducing all phenomena observed in stars, such as the close orbits of "hot Jupiters". Since the discovery of the first hot Jupiter by Marcy & Butler (1995), planetary detection and formation has
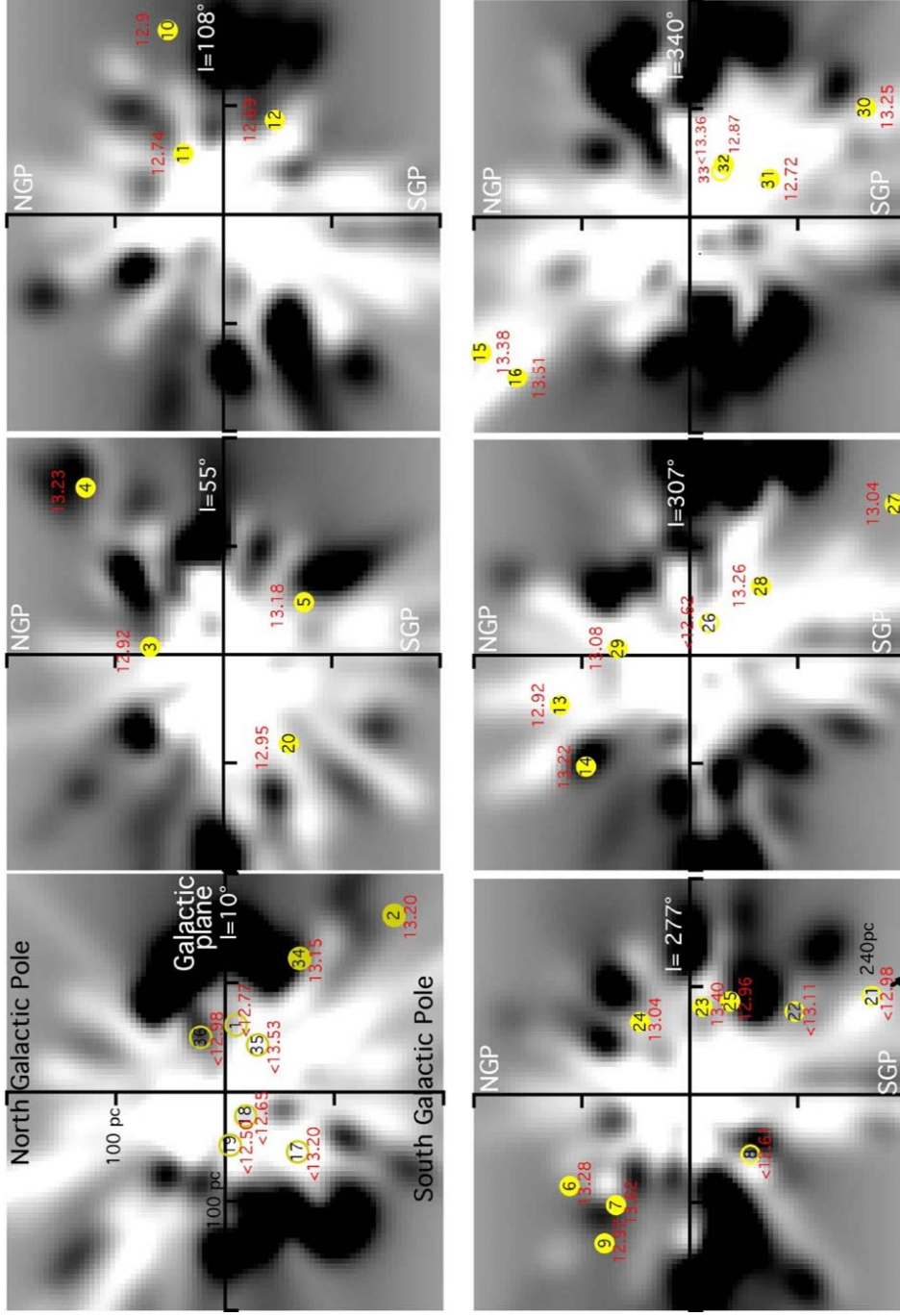
Figure 1.7: O VI detections (filled yellow circles) and non-detections (empty yellow circles) plotted over density maps of the LISM. Darker regions correspond to higher densities. Figure from Barstow et al. (2010). Black numbers inside circles are references internal to Barstow et al. (2010). Red numbers are Log(N_{OVI}).

become one of the leading fields in astronomy. Explaining the great diversity of planetary systems requires a great deal of observational and theoretical investigation. Observing the epoch of giant planet formation is crucial for constraining both models of star and planet formation, as the two processes are closely linked.

1.3.1 Proto-Stellar Evolution

The evolutionary states of pre-main sequence stars are categorized by their spectral energy distributions (SEDs) between 2 and 25 μm (Lada & Wilking, 1984; Lada, 1987; Andre et al., 1993). Figure 1.8 shows a schematic representation of this process. In their early stages, these forming stars are deeply shrouded in their parent molecular clouds, with high extinction ($A_v \geq 100$). These collapsing cores have SEDs which peak in the far-IR and mm, and are designated Class 0. Still too cool at the core for nuclear fusion ($T \approx 30K$), the conversion of gravitational energy into thermal energy is responsible for the excitation of molecular rotation states. CO emission is capable of escaping the clouds, enabling further cloud collapse and observation of the process.

As the cloud collapses, conservation of angular momentum causes a disk to form over a few hundred thousand years. Emission increases at mid- and far-IR wavelengths, dominated by the warming dust. This evolved protostar is classified as Class I. By the time the star is $\sim$1 - 2 million years (Myr) old most of the collapsing gas has fallen onto the star or its disk, and visible to mid IR emission from the star can be seen. At this stage, the object is classified as a Class II protostar. Amongst the Class II group, low-mass ($M < 2M_\odot$) stars are designated classical T Tauri Stars (CTTSs), while intermediate mass ($M = 2 - 8M_\odot$) stars are known as Herbig Ae/Be stars (Herbig, 1960). CTTSs are typically identified by their variable broad Hα (equivalent width (EW) >3 Å) and Ca II H and K emission lines. In addition, they exhibit high Li abundances. These are typically used to estimate age due to its dependance on temperature as the star evolves; however recent evidence suggests that varying accretion can affect Li abundances independent of age (Baraffe et al., 2010). The SEDSs also contain distinct mid-IR excess emission above the stellar spectra, due to warm dust grains orbiting the star at $r \leq 20$ AU.
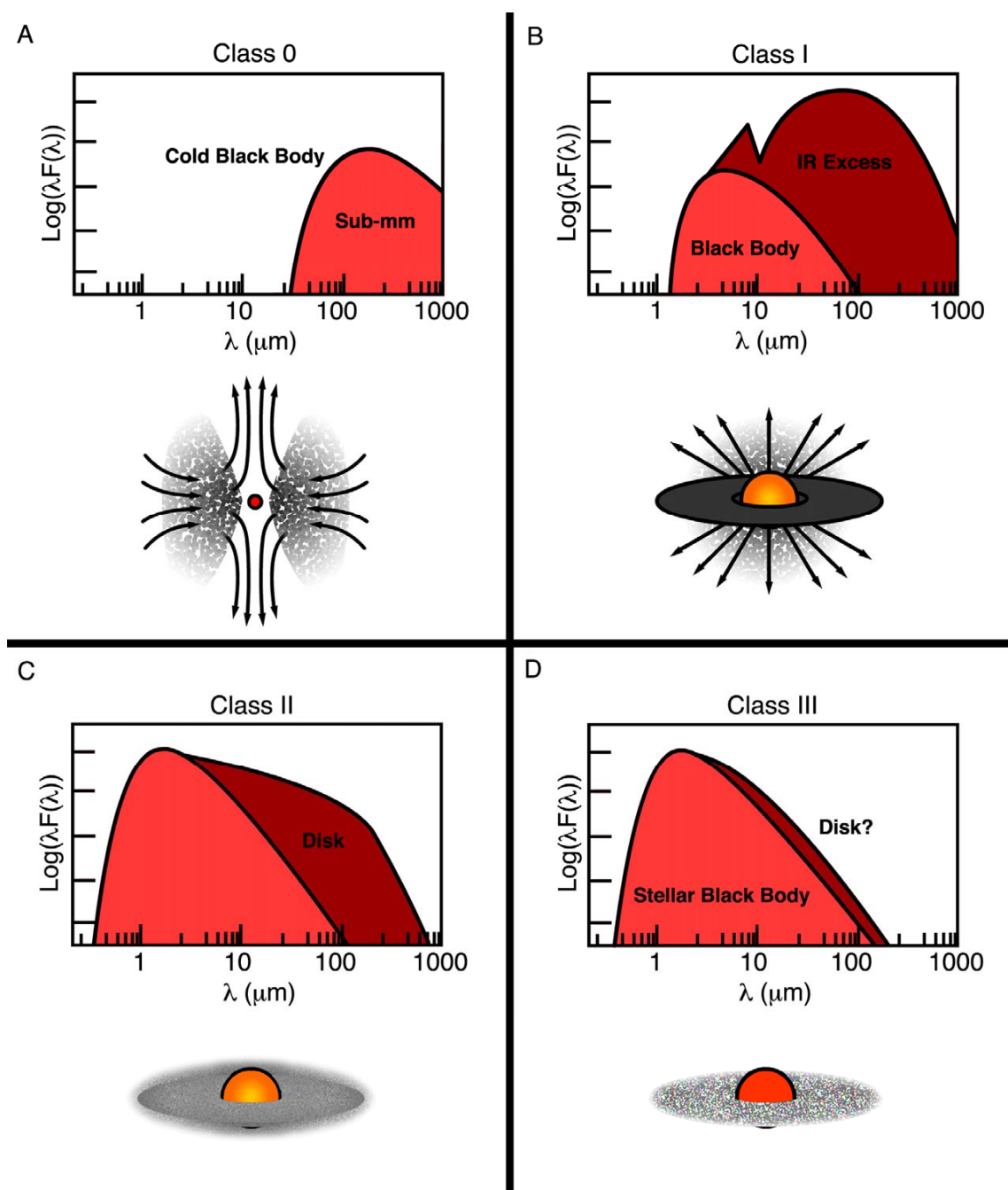
Figure 1.8: The four classes of young stellar objects. A: In Class 0, cold gas and dust fall in towards the star and emit in the sub-mm. B: A disk begins forming during the Class I phase, with added emission from a pre-stellar blackbody. C: In the Class II, or classical T-Tauri star phase, the disk is fully collapsed, and accretion of material onto the star continues. D: By the Class III phase, accretion has ceased, and all evidence of gas, and most of the dust, is gone.

Over the next ∼10 Myr of the star's life, gas and dust slowly accrete onto the star, draining the disk. Typical accretion rates are $\dot{M}= 10^{-12}$ - $10^{-6} M_{\odot} yr^{-1}$ (Hartmann et al., 1998; Gullbring et al., 1998). In addition, the ∼1 μm dust particles (which create the near-IR SEDs) aggregate into larger particles, decreasing the IR excess. In some CTTSs, jets and winds form due to magnetic fields and the evaporation of disk material from stellar radiation. Images of these are shown in Figure 1.9. Eventually accretion ceases, and as the gas disappears, so does line emission from the inner disk. In a survey of near-IR excess flux, Haisch et al. (2001) confirmed that the "disk fraction", the fraction of stars with disks at a given age, decreases over a timescale of several Myrs. Protostars at this later stage ($t > 10$ Myr) are referred to as weak-lined T Tauri Stars (WTTSs), distinguished by lower Hα emission EW (<3 Å) and little excess IR radiation from dust. Some objects show less flux in the near- and mid-IR, and are considered "transitional" objects between CTTSs and WTTSs (Najita et al., 2007). SED models predict this deficit to be a result of a hole in the inner disk, where material has been cleared out. In addition, they tend to show lower accretion rates per disk mass than CTTSs, due to material cleared from the disk.

After 8 - 10 Myrs, most of the gas has accreted onto the star, been blown away by winds and/or jets, or formed into gas giant planets. Core accretion giant planet formation models require timescales of millions of years (Inaba & Ikoma, 2003; Lissauer et al., 2009); as this corresponds to the timescale over which T Tauri gas disks disappear, it is important to fully understand the relationship between the proto-planetary gas and these planets. T Tauri stars present an excellent opportunity to study the transition phase between a molecular cloud and a main sequence star with a planetary system. Detailed observations of these objects can constrain models of terrestrial and Jovian planet formation. However, due to the great variety of dynamical processes (accretion, turbulence, jets, winds, etc.) at work, many observational and theoretical techniques are required to create an accurate picture of these evolving disks.
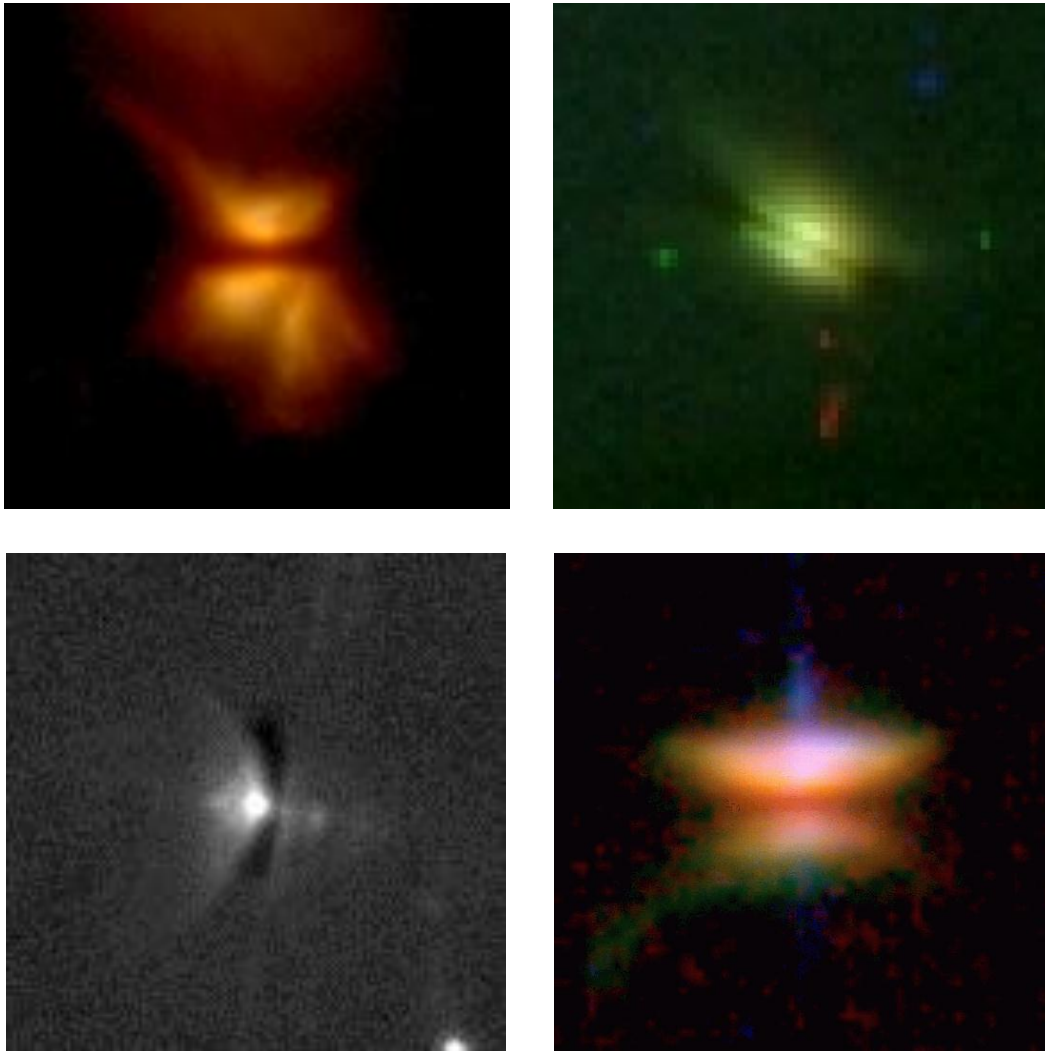
Figure 1.9: HST NICMOS, ACS, and WFPC 2 images of CB 26 (upper left), Orion 473-245 (upper right), Orion 216-0939 (lower left), and HH 30 (lower right). Dark disks, as well as outflows and jets can be seen. Images from Sauter et al. (2009), Ricci et al. (2008), Smith et al. (2005), and Watson & Stapelfeldt (2004).

1.3.2   Structure of T Tauri Star Systems

A diagram of a typical T Tauri disk is shown in Figure 1.10 (Dullemond & Monnier, 2010). It identifies important regions by radius, composition, and observable emission processes. Generally, the wavelength of emitted radiation is proportional to the orbital semi-major axis of the emitting material. Although Figure 1.10 depicts the disk out to 100 AU, the full disk can extend outward to as much as ∼1000 AU. The outer disk (>10 AU) region has been imaged for many targets from radio to visible wavelengths. Cold dust in the disk emits strong thermal continuum radiation in the FIR and mm. Rotational transitions from cold molecular gas are also observable at those wavelengths. Closer in to the star (∼1 - 10 AU), the planet formation region is best probed in near to mid-IR emission from rovibrational molecular lines and warmer dust. In some systems, stellar radiation can heat gas and dust on the surface of the disk, causing it to puff up and have a flared structure. Thermal emission models of flat or flared gas/dust disks match the excess emission seen in T Tauri stars (Chiang & Goldreich, 1997; Men'shchikov & Henning, 1997; D'Alessio et al., 1998).

The inner disk (≤1 AU; Figure 1.11) is a transition region to a pure gas disk. Visible and ultraviolet light dominate the emission in this area, although an IR continuum is present. This has been confirmed with an interferometric imaging survey of several CTTSs: the size of the emission region shrinks with wavelength (Eisner et al., 2007). Inner disk dust has been shown to contain more silicates than in the outer disk (van Boekel et al., 2004). These silicates form from conglomerations of smaller grains, and likely lead to planetesimal formation. The "dust inner rim" is the boundary where temperatures have risen enough to destroy the dust (likely sublimation at 1000 - 1500 K), leaving behind only gas, and is generally assumed to be in local thermodynamic equilibrium (Najita et al., 2003). Energy for heating is believed to come from a magnetospheric accretion shock at the proto-stellar surface (Calvet & Gullbring, 1998; Costa et al., 2000; Ardila et al., 2002). Stellar magnetic fields control the disk material, causing it to accrete onto the star in a funnel flow. From the outer disk edge to the stellar surface, these protoplanetary systems span a large range of size, density, and temperatures. The properties of dust and gas in the disk at different radii and heights
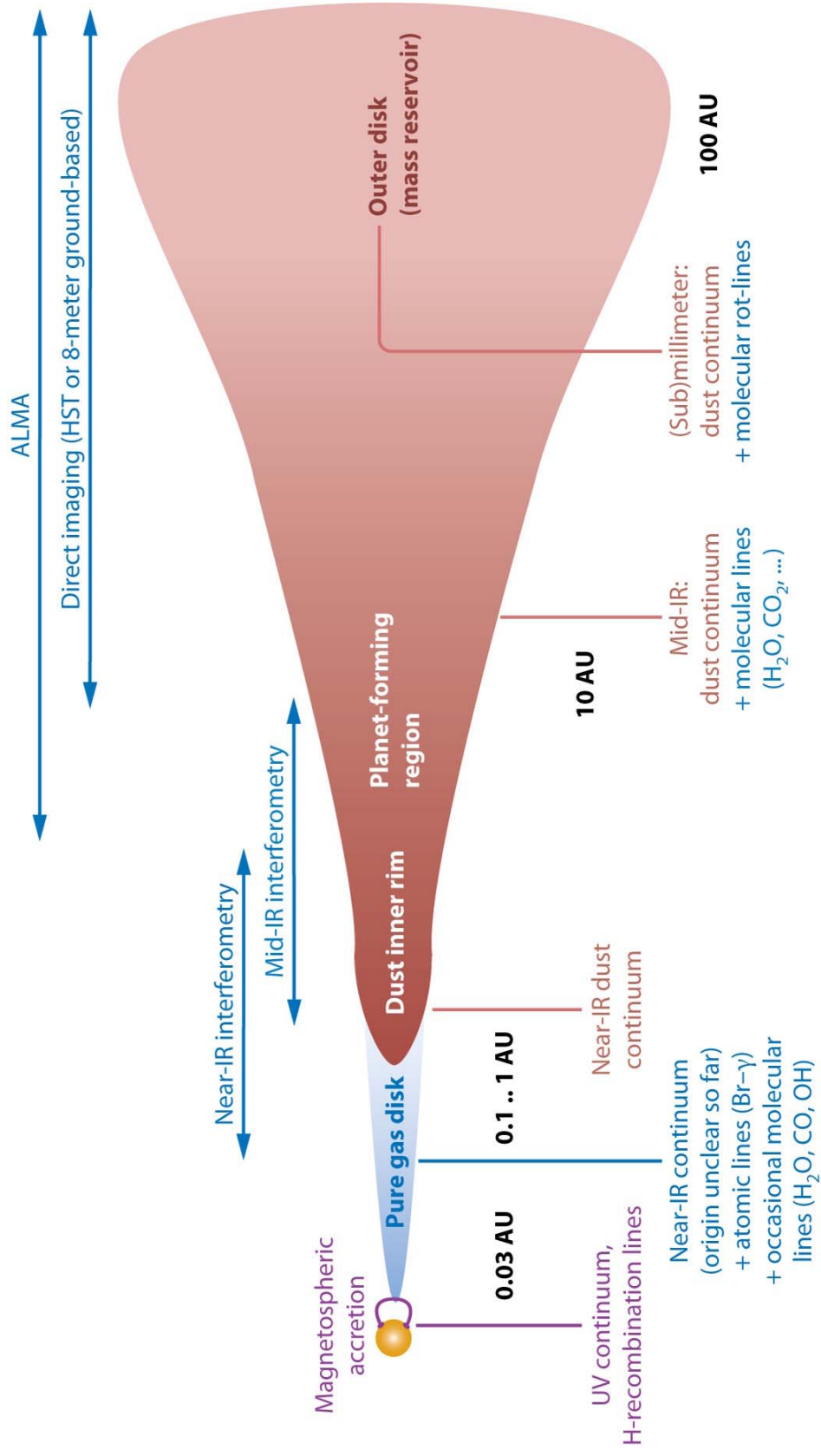
Figure 1.10: Overview diagram of T Tauri circumstellar disk, labelling which imaging techniques are used to probe each region (above), as well as the particular emission processes involved (below). Figure from Dullemond & Monnier (2010).

can impact stellar and planetary formation.

Until recently, dust has been the primary observable in T Tauri stars, and has been used to derive many disk properties. As the disk dust is optically thin at far-IR and millimeter wavelengths, the emission can be used to estimate the dust mass. Using typical interstellar gas/dust ratios ($\sim$100), disk masses from 0.001 - 0.3 $M_\odot$ have been measured (Andrews & Williams, 2005, 2007). Features of the SED can reveal much about dust properties in the disk. For example, the slope of the (sub) millimeter emission changes depending on grain size, as different sized-grains emit strongest at particular wavelengths. In addition, the SED can indicate radial regions where dust is absent; a deficit of emission between 2μm and 8μm is due to a lack of hotter dust that should be within a few AU of the star. In this way, the dust is a powerful probe of hidden processes in CTTSs.

With far-IR and mm imaging, measuring the SED at different radii enables the characterization of dust properties as a function of orbital radius, and can even imply the presence of planets or protoplanets. Figure 1.12 shows 1.3 mm and 2.8 mm emission maps of two CTTSs, RY Tau and DG Tau (Isella et al., 2010). By calculating the dust opacity of the inner regions, they found that the dust has likely been reprocessed, growing as large as 20 μm in diameter. In planetary formation models this type of grain growth is an important first step. Transitional objects with cleared inner dust holes are also believed to host planets or to be forming planets. Andrews et al. (2009) surveyed 1 Myr old circumstellar disks in the Ophiuchus star-forming region, finding several objects with large inner regions ($\sim$20-40 AU) cleared of dust. Hughes et al. (2009) reported similar findings in the GM Aur disk.

Based on interstellar gas to dust ratios, one expects gas to dominate the mass of the disk. However, gas has proven far more difficult to observe than the dust. The most prevelant molecule in disks, H_2, has no permanent dipole moment, thus its vibrational and rotational IR lines are rarely measured (Ramsay Howat & Greaves, 2007). The second-most abundant molecule, CO, emits strongly at these wavelengths, and is most often used to probe the gas component. CO emission is formed at many radii in the disk, and it is uncertain as to whether or not the molecular gas is
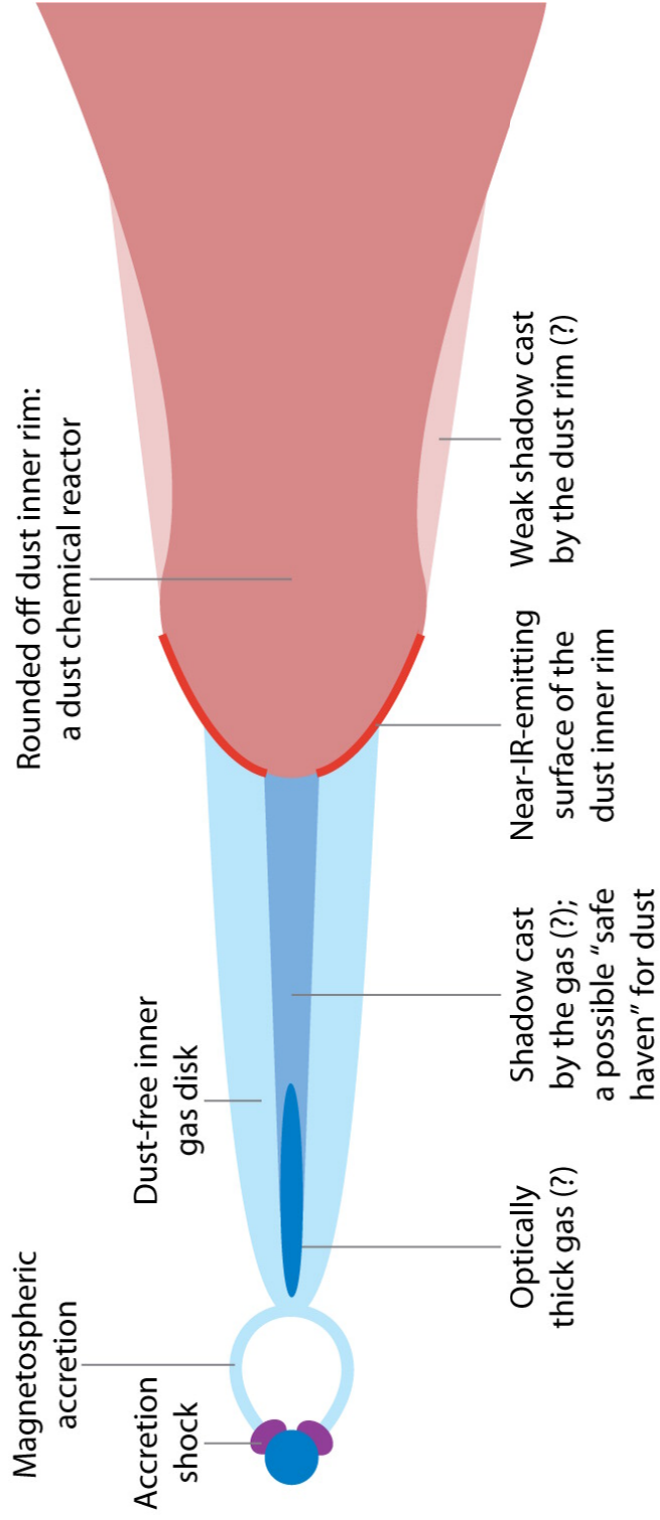
Figure 1.11: Inner ~1 AU of a T Tauri circumstellar disk. Figure from Dullemond & Monnier (2010).
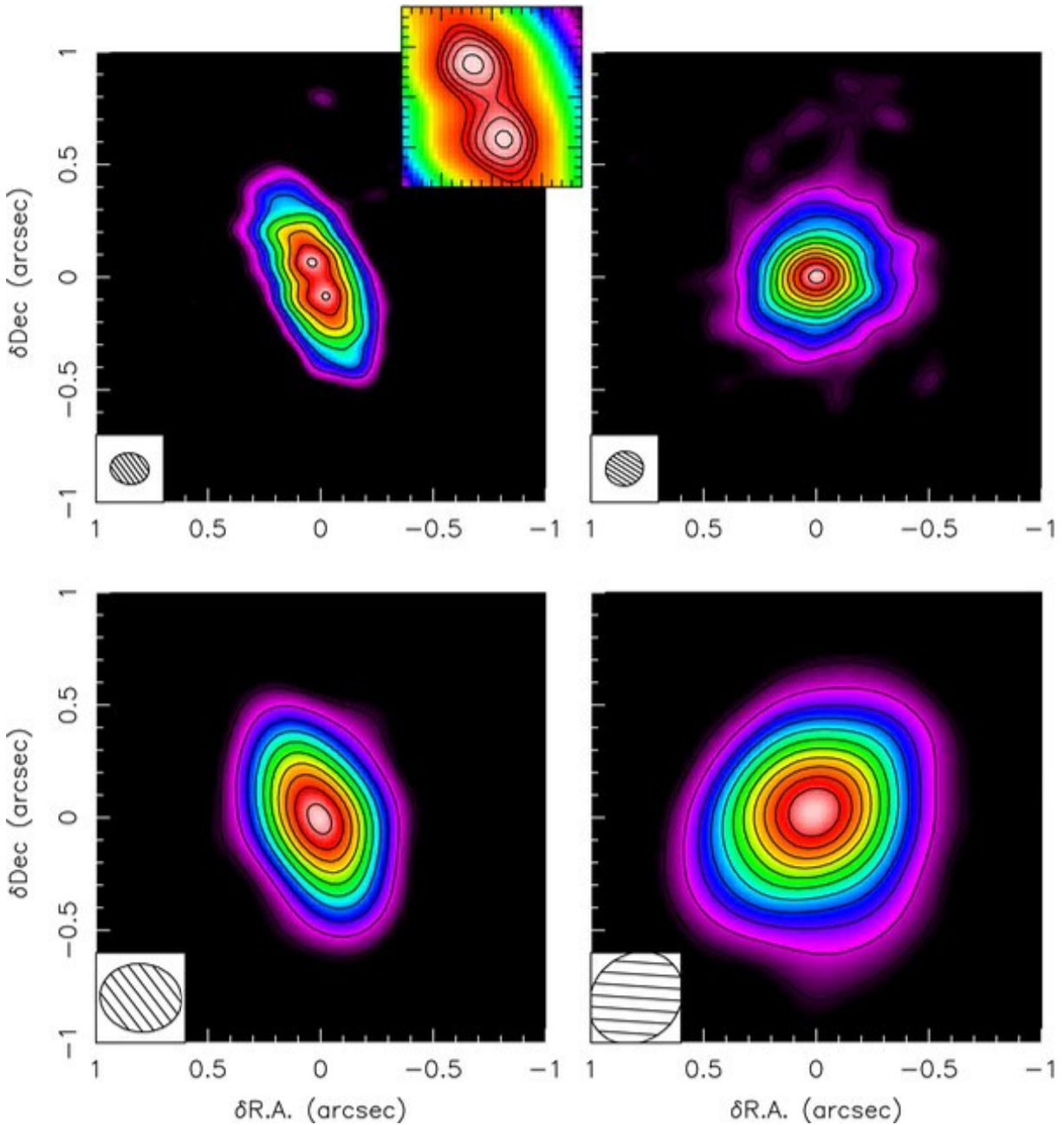
Figure 1.12: 1.3 mm (top) and 2.8 mm (bottom) thermal emission maps of RY Tau (left) and DG Tau (right) taken with CARMA. Color contours represent surface brightness, beginning at 3σ and increasing 4σ for every contour. RY Tau 1.3 mm inset contours begin at 28σ, increasing by 1σ. Synthesized beam sizes are inset in the lower left of each image. Figure from Isella et al. (2010).

distributed differently than the dust (Isella et al., 2007; Hughes et al., 2008). The total gas mass of a disk can be estimated by measuring the CO column density, and then applying an H_2/CO conversion factor. Molecular emission lines also enable the characterization of the disk rotational velocity profiles. Double-peaked features or significantly broadened lines imply Keplarian rotation of the gas, and have been found in multiple surveys of CTTSs (Artemenko et al., 2010).

The inner disk has proven more difficult to understand than the outer disk, due to technological limitations. Most presently studied T Tauri stars are $\geq$ 100 pc away. As such, these inner regions are approximately 10 milliarc seconds (mas) in size on the sky, below the angular resolution limits of current optical and UV instruments. The lack of sufficiently detailed observations, combined with the complexity of the dynamical processes at play, make modeling challenging. Models must consider the distribution of dust with height above the disk plane, the opacity of the gas, heating from stellar radiation compared with emission from thermal blackbody radiation, opacity wavelength dependance with the size of the dust grains, and the balance of condensation and evaporation. The accretion, sublimation, and photodissociation of the inner disk regulates the physical and chemical structure of the outer disk. Models of disk evolution and planetary formation require observational constraints on these processes.

Visible and ultraviolet line emission can be seen along the outer surfaces of the disk, however such atomic and molecular emission predominantly occurs in the inner region of the disk ($r \approx$ 0.01-0.1 AU) (Dullemond & Monnier, 2010). The radiation produced from accretion of the disk is primarily responsible for exciting the atoms and molecules. The majority of the far-UV emission lines are from the strong B-X electronic transitions of H_2 (Herczeg et al., 2002, 2006). H_2 fluorescence from TW Hya is pumped primarily by Lyα emission (Herczeg et al., 2002). Herczeg et al. (2004) found that the H_2 emission most likely came from a T $\approx$ 2500K inner disk ($r \approx$ 2 AU) region. In addition to fluorescent emission, electron-impact H_2 continuum features have been observed in the spectra of several CTTSs. Bergin et al. (2004) first identified this emission just below 1700 Å in the spectra of LkCa 15, GM Aur, and DM Tau. A recent study of HST STIS and ACS data identified broad features in the spectra of several T Tauri stars around 1600 Å (Ingleby et al.,

2009). Figure 1.13 shows the STIS spectrum of TW Hya, convolved to the HST-ACS resolution to compare with ACS targets. They attributed these emission features to electron impact excitation of H_2.

The recently installed Cosmic Origins Spectrograph (COS) onboard *HST* combines high sensitivity with low internal scatter to provide unprecedented S/N UV spectra of these CTTSs. France et al. (2011a) studied spectra of DF Tau and V4046 Sgr, characterizing the molecular and continuum emission. These authors modeled accretion continuua and electron-impact excitation. They also found that far-UV continuum emission from the accretion shock dominates over radiation from the ISM. However, while the longer wavelength continuum emission appears strong, shorter wavelength features are nearly absent. This could be caused by dust attenuation, although some studies have shown that the interaction between the stellar UV radiation and grain evolution could decrease dust presence close to the star (Vasyunin et al., 2011). If this were the case, gas would be responsible for such attenuation. The UV emission clearly plays an important role in the inner regions of CTTS disks, and therefore the process of planetary formation. Such ambiguity regarding the interaction of dust and gas in the inner disk leaves much room for observation and interpretation.

1.4   This Thesis

This thesis explores the above phases of the ISM in two different ways. First, in an attempt to further our understanding of the Local Bubble, I designed a sounding rocket payload to record high resolving power (R $(\lambda/\delta\lambda)$ = 60,000) spectra of the O VI doublet (λ = 1032,1038 Å). Explained in detail in Chapter 2, I describe the instrument design, flight preparations, and flight results of this high-resolution, space-borne instrument. Second, to better understand the process of planetary system formation, I have used the *HST*-COS to survey the molecular properties of protoplanetary disks. I have performed a survey of Carbon Monoxide UV emission features originating in the inner protoplanetary disks of nearby T Tauri stars. I model the CO profiles to constrain temperatures and column densities of the gas. In Chapter 3, I will describe the COS observations, data modeling, and implications for the structure and composition of the inner disk.
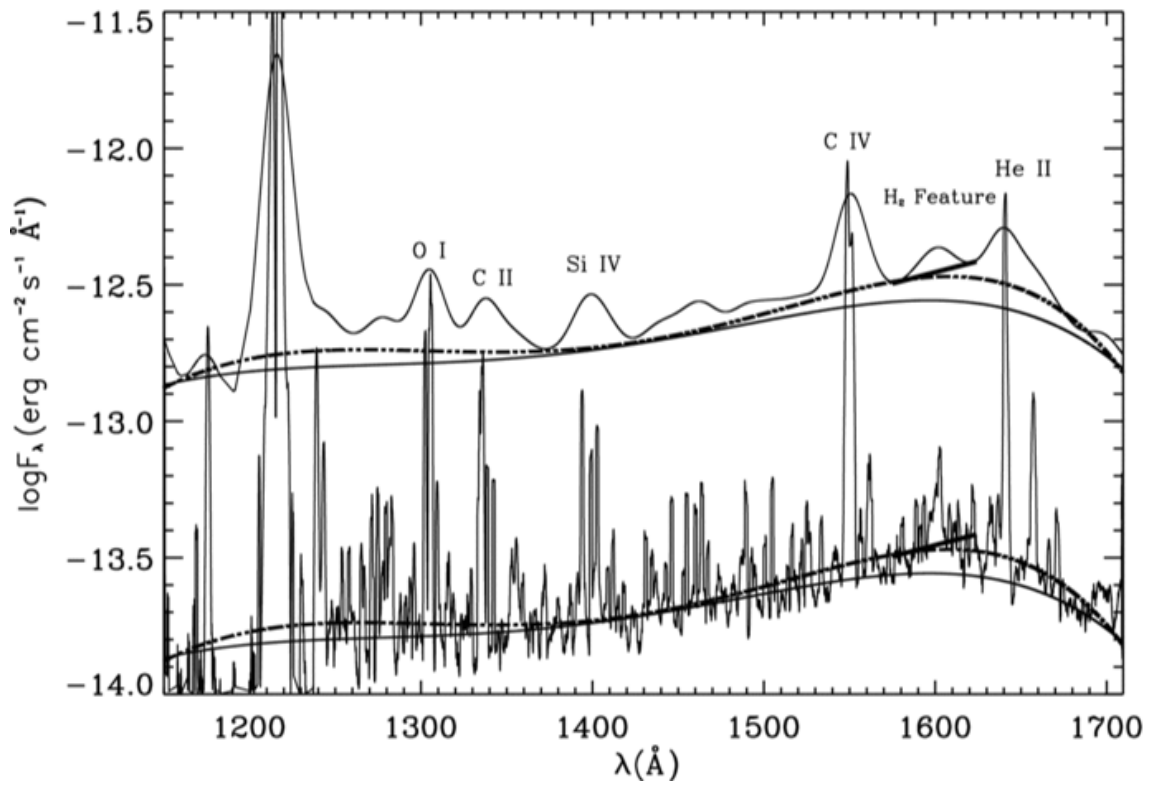
Figure 1.13: *HST* STIS spectrum of TW Hya (bottom), when convolved to *HST* ACS resolution (top), shows a feature at 1600 Å attributed to H_2 electron-impact excited emission. Model continua are overplotted. Figure from Ingleby et al. (2009)

Chapter 2

The Diffuse Interstellar Cloud Experiment

Success is the ability to go from failure to failure without losing your enthusiasm.

\- Sir Winston Churchill

2.1   Introduction

In the Interstellar Medium (ISM), the majority of atomic and molecular resonant transitions lie in the far ultraviolet (Friedman et al., 1994). Interstellar gas resides in clouds and filaments at temperatures ranging from tens to millions of degrees Kelvin. The gas composition and dynamics can be studied through absorption spectroscopy. However, due to the complex structure and dynamics of these clouds, high spectral resolution (< 5 km s^{-1}) and throughput are required to truly probe the systems. Achieving both of these goals simultaneously at UV wavelengths is challenging with current technology. Echelle spectrographs can obtain the necessary resolution with the use of a grating and cross-disperser. Broadband spectra can be obtained by recording multiple orders on a single detector. Unfortunately this design suffers significant signal loss due to the diffraction efficiency of two gratings and often even extra optics. Even the best optic coatings have reflection efficiencies between 30% - 60% below $\sim$1200 Å. Such low throughput vastly limits the ability to observe faint sources. Therefore, to maximize system efficiency the number of optical reflections in a spectrograph must be kept to a minimum.

The Rowland circle mount is advantageous for higher throughput due to a single diffracting optic. In addition, the typical scatter from mechanical rulings can be avoided by using holographic

rulings, reducing overall noise. The holographic recording geometry gives the designer freedom to minimize optical aberrations without resorting to complicated mechanical surfaces. The disadvantage of this approach to high spectral resolution is in the physical limitations of the detector. Holographic solutions can produce extremely narrow spectral lines, however as the spectrum is dispersed in a single dimension, the spatial resolution of current detector technology limits how small a spectral line can actually be detected.

To address these technological challenges, Green et al. (1993) proposed an optical design which introduces a reflecting mirror into a Rowland mount spectrograph. This secondary optic magnifies the spectrum from the grating, enabling resolution better than $5 \, \mathrm{km \, s^{-1}}$ with conventional detectors and gratings. The second reflection reduces overall throughput, however this decrease is small compared with an echelle, while echelle-quality resolution is still possible. Such a system is ideal for the study of faint background sources with narrow absorption lines. With this groundwork in mind, I designed, assembled, and launched the Diffuse Interstellar Cloud Experiment (DICE), a sounding rocket-bourne instrument for measuring the O VI doublet (1032 Å, 1038 Å) at high resolving power (R $\sim$60,000). It is the first spectrograph capable of such high resolution and signal to noise at these wavelengths. This improved optical design tests new technology for use in future space missions.

In this chapter I present the design, alignment, and performance of the instrument. The scientific motivation for the instrument is reviewed in §2.2, and in §2.3 I give an overview of the experiment and its constraints. I describe the spectrograph design in §2.4, and show the alignment and calibration of the instrument in §2.6. In §2.7 I discuss flight results.

2.2   Scientific Motivation

As discussed in Chapter 1 further investigation of O VI in the LISM is necessary to strengthen the model of hot gas in the LB. I have designed an instrument to measure the properties and formation processes of O VI. Our selected target stars, δ and π Scorpii, where chosen due to their brightness. They are separated in the sky by only $\sim$10 pc, with similar distance ($\sim$120 pc) within

parallax errors (Perryman et al., 1997). From Copernicus observations, the O VI column density increases by over a factor of 6 from π to δ Scorpii (Jenkins, 1978). In addition, the Na I column increases from π to δ by an order of magnitude in high-resolution ground-based spectra (Hobbs, 1974). The existence of O VI so close to the cold Na I implies the presence of some heating source. It is therefore likely that a hot/cold gas interface exists between the two stars. The normalized spectra of the Copernicus O VI 1032 Å data are shown in Fig. 2.1 for δ and π Scorpii. The extra absorption in the δ Scorpii profile is assumed to result from gas near the interface.

Proper continuum normalization of the Copernicus data is difficult, as pointing errors during the observations changed flux levels at different portions of the spectrum. However, general features are evident. There is a strong absorption component at $\sim$ -10 to -20 km s^{-1}, at a similar velocity as the cold Na I gas (-12 km s^{-1}) (Hobbs, 1974). With the resolution of Copernicus, it is difficult to calculate an accurate centroid for the component, so the exact O VI velocity relative to the cold Na I is unclear. In addition, the δ Scorpii spectrum shows a broad absorption feature that stretches out to positive velocities. Jenkins (1978) fit the entire absorption feature with a single gaussian, assuming that the O VI is produced in collisional ionization equilibrium through conductive heating or turbulent mixing processes. However, if the O VI is rapidly adiabatically cooled, it would be overionized, producing the observed emission and absorption at cooler temperatures (Indebetouw & Shull, 2004). This would correspond to absorption widths less than 15 km s^{-1}, which would not be distinguishable at the resolution of Copernicus. In addition, typical gas components in the LISM can be separated by velocities as small as 1 - 5 km s^{-1}).

The previous studies were limited by the instrumental capabilities of *Copernicus*. Jenkins (1978) recognized that a more complicated interface could exist at the Local Bubble wall. Multiple gas components could exist in a variety of dynamic states, or different states of ionization. Any one of these could have different implications on the physics of how the O VI is formed, particularly whether or not a 10^6 K gas still exists there. To directly probe these multiple components of warm-hot gas, I designed a spectrograph to observe the O VI doublet in absorption towards these two stars. For reliable analysis of absorption lines, I required simultaneous recording of the entire
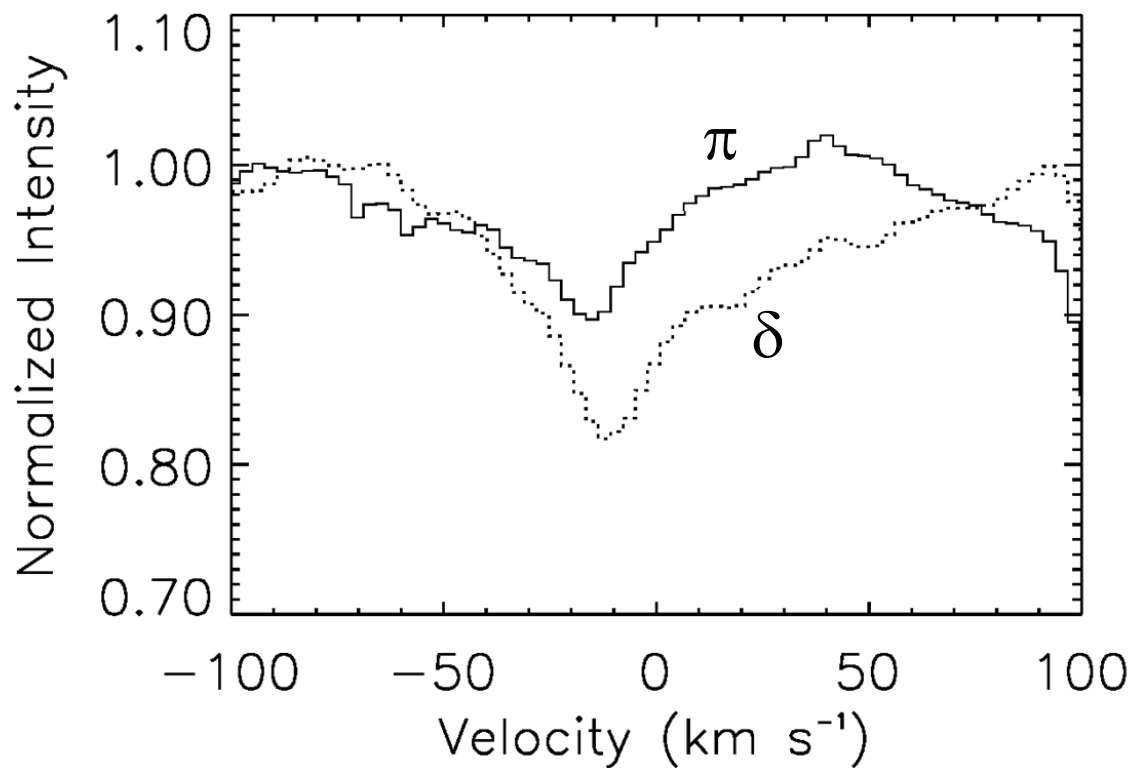
Figure 2.1: Normalized Copernicus O VI 1032 Å data for π (solid) and δ (dotted) Scorpius. Warm-hot gas appears to approach us at approximately the same speed of the cold wall (10 - 20 km s^{-1}). Additional material in the δ Scorpius spectra seems to flow away from us, potentially on the other side of the wall.

spectrum. I defined a resolution requirement of 5 - 15 km s^{-1} to determine column densities, centroid velocities, and Doppler parameters of individual components. These properties can reveal detailed motions of the O VI relative to the cold cavity wall, critical in understanding the formation processes of warm/hot gas in the ISM.

2.3 Instrument Concept and Considerations

The DICE instrument consists of a Cassegrain telescope followed by the previously mentioned modified Rowland spectrograph. Figure 2.2 shows a schematic diagram of the light path through the payload. The telescope focuses light from the star onto a slit, which minimizes wide-field airglow contributions that would otherwise contaminate our spectrum. The spherical grating then disperses the slit image according to the standard Rowland mount geometry: any given wavelength is focused along a circle with the same diameter as the radius of curvature of the grating, according to the grating groove density and angle of incidence. A magnifying optic placed in the dispersed beam gives the spectrograph a longer focal length in a compact space, achieving higher resolution at the detector.

A Cassegrain telescope was chosen for several reasons. Its typical small size met with our goals of a compact payload. Because we were using a slit as an entrance aperture for the spectrograph, we were not concerned about its small field of view or off-axis performance. The Cassegrain lends itself to the cylindrical payload skins, so the focus can be accessed behind the telescope, as opposed to the side in a Newtonian. In addition, field curvature is less for a Cassegrain over a Gregorian, which is advantageous due to the thickness of the slit and machining tolerances. The slit itself adds benefits to the system in addition to simply providing a spectrograph aperture. The image of the star can be monitored in-flight on the slit substrate with a Xybion ISS-255 intensified video camera. This is necessary, as the intial target acquisition of the Attitude Control System (ACS) is only accurate to a couple arcminutes; real-time steering is necessary to point the spot onto the slit.

The optical system can be parameterized as depicted in Figure 2.2. The telescope primary and secondary mirrors have radii of curvature R_1 and R_2, respectively, and are separated by d_{ps}.
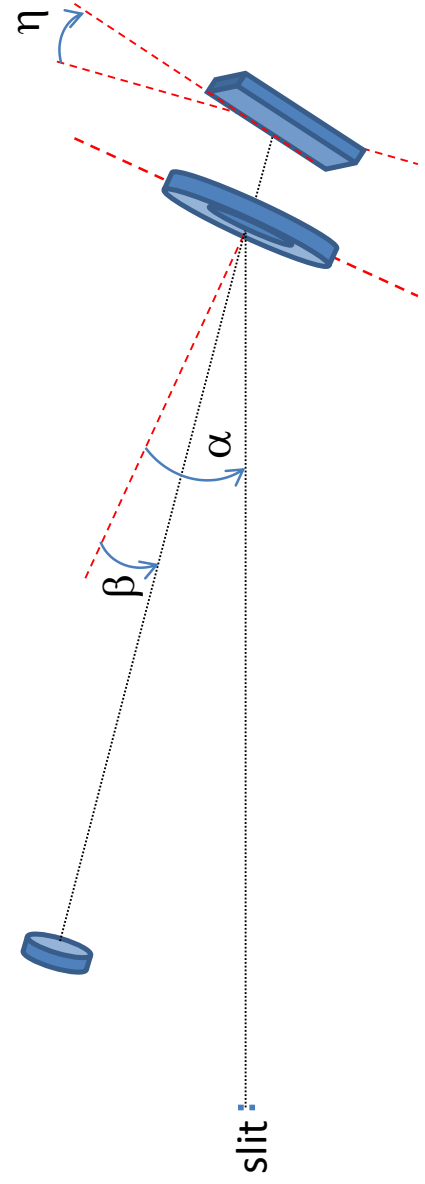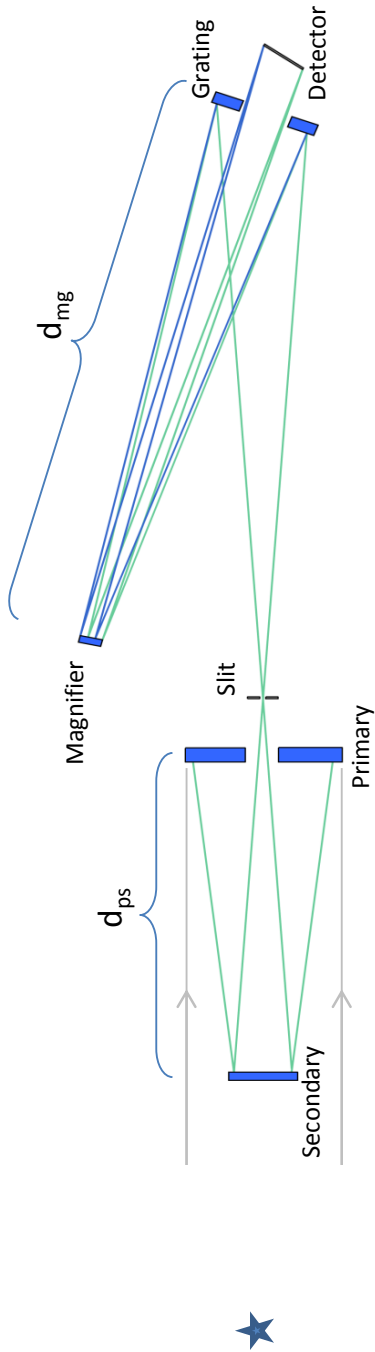
Figure 2.2: Top: Ray diagram for the payload optics (not to scale). Light enters the system from the left. The telescope primary and secondary focus the star onto a slit, whose image is then dispersed off the grating and reflected off the magnifier onto the detector. The blue and green lines represent 1020 Å and 1040 Å, respectively. Bottom: Geometry of the spectrograph, from the slit to the detector. The black dotted line shows the light path, while the red dashed lines show axes.

The primary eccentricity e_1 was fixed at 1 for a Cassegrain design, and the back focal distance to 100 mm to leave room for mechanical structure and alignment purposes. The secondary eccentricity e_2 and primary diameter D_1 are determined by further constraints, discussed below. The magnifier and grating are separated by distance d_{mg}, and the grating was chosen to be a sphere ($e_g = 0$). With the goal of designing a relatively compact spectrograph, I chose a grating radius of curvature R_g of 1000 mm. I fixed the detector center at 100 mm behind the grating, again to accomodate mechanical structure and the alignment process. The grating groove spacing σ, diffraction angles α and β, magnifier radius of curvature R_m and eccentricity e_m, and detector angle η relative to the magnifier's optical axis are in part constrained by the physical size (diameter and length) of the sounding rocket payload, and are discussed in §2.4.

In addition to physical constraints, the other chief driver for our instrument design was the desire to use an existing detector to record the spectrum. The detector spatial resolution limits the maximum detectable spectral resolution. I used a pre-existing microchannel plate (MCP) detector to record the spectrum in flight. The 60-mm x 10-mm MCPs are lead silicate glass, perforated with microscopic $\sim 10\mu$m holes. The top plate is coated with cesium iodide (CsI), a photocathode that produces an electron upon the collision of a photon. The CsI provides $\sim$30% efficiency around 1032 - 1038 Å. Three MCPs are stacked in total, in a "z" pattern, in which the holes are oriented at angles relative to one another. Photoelectrons from the photocathode are accelerated by 5750 V across the MCPs, impacting on the channel surfaces. The end result is an electron shower which lands on a double delay-line anode below. The two delay lines are laid down in a cross-wedge pattern. The X position is determined by how long it takes the signal to go from the photon event to the sides of the delay line. The charge ratio between the two delay lines yields the Y position, although less accurately. In X the spatial resolution is approximately $\sim$ 35 microns, and in Y it is $\sim$ 100 microns; I use X as the spectral dimension.

This minimum spatial resolution defines our magnification requirement, when combined with a desired bandpass and a given grating. I chose a bandpass of 1020 Å to 1040 Å to fit our science requirements. This is a wide enough range to record both lines of the O VI doublet (1032 Å, 1038

Å) and register a deuterated molecular hydrogen (HD) line at 1022 Å. A weak HD line contaminates the 1032 Å O VI feature; therefore it is necessary to measure HD separately to remove confusion from the O VI. Covering this bandpass at R = 60,000 over a 60 mm detector requires ~50 μm resolution elements. However, the dispersion of a grating with a radius of curvature of 1000 mm and 4500 grooves/mm (chosen for a compact spectrograph and reasonable industry standards) is roughly 2.5 Å per mm. With the detector spatial resolution of 35 μm this limits R below 12,000. At R = 60,000 a line is 7μm wide; thus the secondary spectrograph optic must provide a magnification of 7.

The telescope size was also a consideration in the spectrograph design. Sufficient size is necessary to collect enough light for high S/N, however a small primary diameter gives more freedom to the grating dispersion; shifting the optical axis away from payload center allows for higher values of α. Therefore I calculated the minimum telescope collecting area to achieve S/N = 25, assuming optic and detector efficiencies, as well as the expected target countrates. The optimal optic coating at these wavelengths is lithium fluoride (LiF), which is typically $\sim$ 60% efficient in a single reflection (Hunter et al., 1971). Under our desired instrument design of 4 Al/LiF-coated optics, a first-order grating efficiency of 30%, and 30% detector quantum efficiency, $\sim$ 1% of the incident flux is collected.

Additional throughput was assumed to be lost at the slit, due to in-flight pointing capabilities and our optical alignment limitations. The ACS system utilizes a camera to track where the payload is pointed; as the camera recognizes any change in pointing, it commands the gas jets to fire in such a way as to reaquire the correct pointing. This results in miniscule drifts during flight. Typical pointing drift is approximately 1" s^{-1}, so I chose this to be the angular size of the slit for the telescope. Our alignment facility is reliably capable of 2" focusing, meaning a 75% loss through the slit. Combining these factors with the expected count rate yields an estimated number of photons per spectral resolution element. From the International Ultraviolet Experiment (IUE) Mulitimission Archive at STScI (MAST) data, I conservatively predicted a flux of approximately 1.0x10^{-8} ergs cm^{-2} s^{-1} Å^{-1} for each target. Assuming 150 seconds on target a minimum effective

collecting area of ~2 cm^2 is necessary to achieve our required S/N. This provides an additional degree of freedom for the spectrograph design, allowing the entire optical system to shift around in the payload.

2.4   Spectrograph Design

With all of these constraints in mind, I set out to design a spectrograph to meet our science goals. Mechanically ruled gratings cannot sufficiently correct aberrations for this task without utilizing highly aspheric substrates, so the grating had to be holographically ruled. This utilizes the interference of light on a glass grating substrate to form the necessary grooves in a photoresist material. I followed the formalism of Noda et al. (1974) to find the optimal recording source solution. The geometry for holographic recording is shown in Figure 2.3. Light enters the spectrograph through a slit at point A, and the grating forms a focus at point B. Relative to the vertex of the grating O, r and α define the position of the entrance slit. r' and β define the position of the focus for a given wavelength. C and D are the positions of the recording light sources; r_c, γ, r_d, and δ define their positions. By carefully choosing these positions I can minimize optical aberrations to achieve our design goals.

To determine the optimal spectrograph parameters, the grating surface is characterized as a power-series expansion:

$$x = \sum_{i=0}^{\infty} \sum_{j=0}^{\infty} a_{ij} y^i z^j \tag{2.1}$$

where the a_{ij} are coefficients for a power expansion in the y and z directions. Since the grating surface is spherical, only the a_{20} and a_{02} terms are non-zero. The combination of the physical surface of the optic with the interference pattern of the recording sources determines the course of a photon through the spectrograph. For a ray of wavelength λ, the light path F from the spectrograph slit entrance A to the final focus point B is
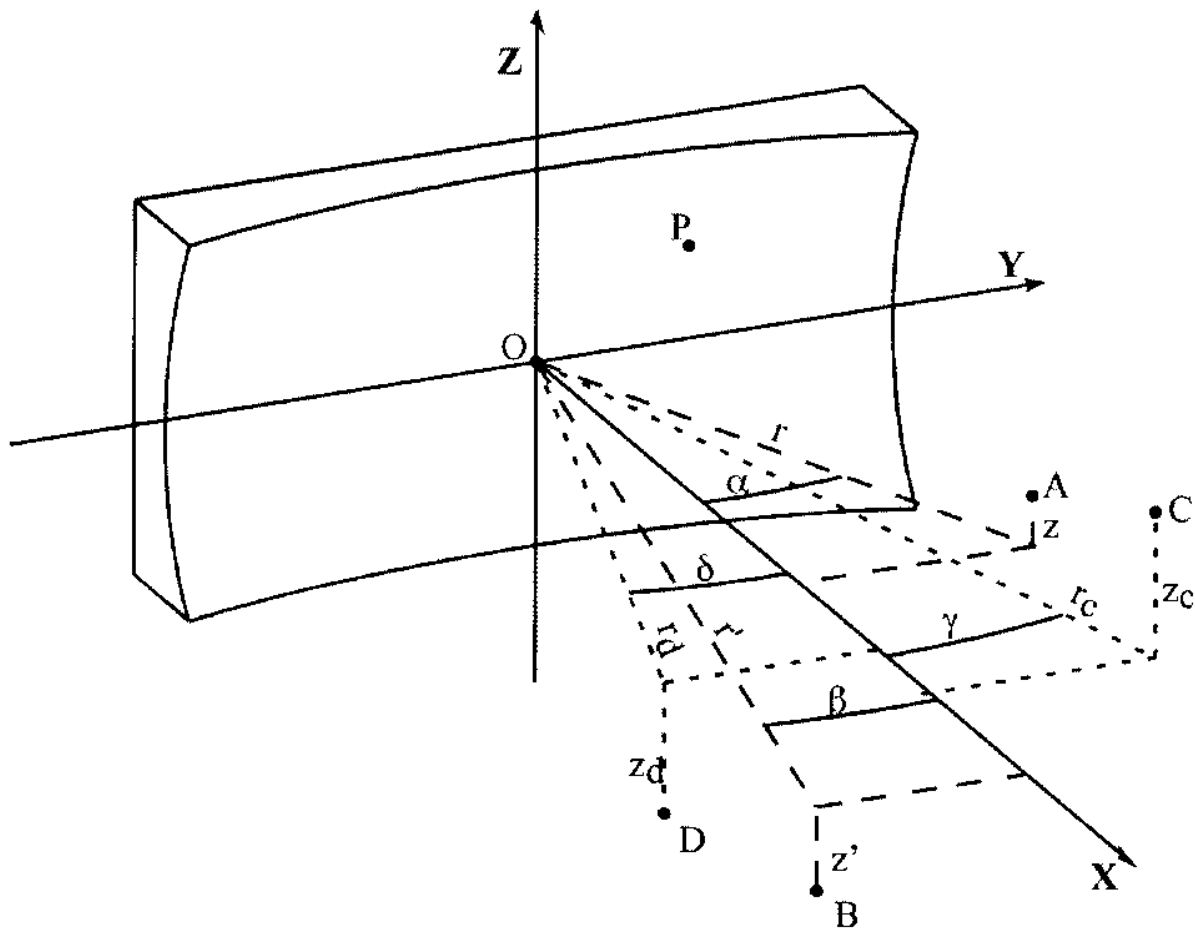
Figure 2.3: Geometry for holographic grating. Point A represents the slit, which is diffracted to point B based on the physical surface of the grating, as well as the interference pattern created by lasers at points C and D. Other parameters are explained in text. Figure from Beasley et al. (2004)

$$F = <AP> + <BP> + \frac{m\lambda}{\lambda_0}[(<CP> - <DP>) - (<CO> - <DO>)] \tag{2.2}$$

where P is a given point on the grating. F can be described in a power expansion as

$$F_{ijk} = M_{ijk} + \frac{m\lambda}{\lambda_0}H_{ijk} \tag{2.3}$$

where the subscripts i, j, and k correspond to the x, y, and z dimensions. λ_0 is the wavelength of the recording laser, and m is the diffraction order. The mechanical term M_{ijk} is dependent on the position of the source and image relative to the grating center, and the positions of the recording laser sources determine the holographic term H_{ijk}. For our desired spectrograph, I ignore the z dimension. The 0th through 3rd order terms in the other two dimensions dominate:

$$F_{000} = r + r' + \frac{m\lambda}{\lambda_0}[r_c - r_d] \tag{2.4}$$

$$F_{100} = -sin\alpha - sin\beta + \frac{m\lambda}{\lambda_0}[-sin\gamma + sin\delta] \tag{2.5}$$

$$F_{200} = \frac{cos^2\alpha}{r} + \frac{cos^2\beta}{r'} - 2a_{20}(cos\alpha + cos\beta) + \frac{m\lambda}{\lambda_0}\left[\frac{cos^2\gamma}{r_c} - \frac{cos^2\delta}{r_d} - 2a_{20}(cos\gamma - cos\delta)\right] \tag{2.6}$$

$$F_{020} = \frac{1}{r} + \frac{1}{r'} - 2a_{02}(cos\alpha + cos\beta) + \frac{m\lambda}{\lambda_0}\left[\frac{1}{r_c} - \frac{1}{r_d} - 2a_{02}(cos\gamma - cos\delta)\right] \tag{2.7}$$

$$M_{300} = \left[\frac{T(r,\alpha)}{r}\right]sin\alpha + \left[\frac{T(r',\beta)}{r'}\right]sin\beta - 2a_{30}(cos\alpha + cos\beta) \tag{2.8}$$

$$H_{300} = \left[\frac{T(r_c,\gamma)}{r_c}\right]sin\gamma - \left[\frac{T(r_d,\delta)}{r_d}\right]sin\delta - 2a_{30}(cos\gamma - cos\delta) \tag{2.9}$$

$$T(r,\alpha) = \frac{cos^2\alpha}{r} - 2a_{20}(cos\alpha) \tag{2.10}$$

These equations are purely for the Rowland mount, with only a grating in the system. The addition of a second optic greatly complicates the analytic solution and resulting equations. Thus,

I utilized the Interactive Ray Trace (IRT) software, a series of IDL routines capable of tracking light rays through a system with a holographically-ruled grating. I use the end ray distribution as a merit for optimization. I do, however, use Equations 2.4 - 2.10 to determine a starting point for the optimization in parameter space. Spectral resolution is our chief concern, thus I choose to ignore any constraints on astigmatism. Therefore F_{200} and F_{300} are the dominant aberrations which must be minimized. To do so I first set F_{200} and F_{300} to zero at a single wavelength λ_{opt} (I chose $\lambda_{opt} = 1030$ Å, the bandpass center), and then use the freedom introduced by the recording source locations to minimize aberrations elsewhere in our spectral bandpass. Rearranging F_{200} yields a formula for r_c:

$$r_c = \frac{cos^2\gamma}{\frac{\lambda}{m\lambda_0}(\frac{cos^2\gamma}{r} + \frac{cos^2\beta}{r'} - 2a_{20}(cos\alpha + cos\beta)) + \frac{cos^2\delta}{r_d} + 2a_{20}(cos\gamma - cos\delta)} \tag{2.11}$$

and rearranging F_{300} leads to a quadratic solution for r_d of the form

$$ar_d^2 + br_d + c = 0 \tag{2.12}$$

where:

$$a = \frac{\lambda_0}{m\lambda}(2M_{200}a_{20}tan\gamma + \frac{\lambda_0}{m\lambda}M_{200}^2 sec\gamma tan\gamma - M_{300}) + 2X_2 a_{20}tan\delta + + X_2^2 sec\gamma tan\gamma \tag{2.13}$$

$$b = 2a_{20}(cos\delta sin\delta - cos^2\delta tan\gamma) + cos^2\delta sec\gamma tan\gamma(2X_2 - \frac{M_{200}\lambda_0}{m\lambda}) \tag{2.14}$$

$$c = cos^4\delta sec\gamma tan\gamma - cos^2\delta din\delta \tag{2.15}$$

and

$$X_2 = 2a_{02}(cos\gamma - cos\delta) \tag{2.16}$$

Finally, the angle γ can be written as a function of groove spacing σ and δ:

$$\gamma = sin^{-1}(sin\delta - \frac{\lambda_0}{\sigma}) \qquad (2.17)$$

In this way, for a fixed α, β, R_g, and σ, varying γ can find the minimum value for F. With R_g already set at 1000 mm, I can further constrain α, β, and σ with the physical limitations of the 17.25" diameter rocket payload skins. For a given separation of the grating and magnifier d_{mg}, the grating can only be tilted so far before the magnifier runs into the skin. The magnifier acts similar to the secondary optic of a Cassegrain telescope, therefore the standard Cassegrain equations give us a starting value for d_{mg}:

$$d_{mg} = \frac{m_m R_g}{m_m + 1} \qquad (2.18)$$

I have already chosen the transverse magnification of the secondary m_m to be 7, in order to achieve the required spectral resolution. The last necessary variable for optimization is the magnifier radius of curvature, which comes from the standard Cassegrain equations:

$$R_m = \frac{2m_m(R_g - d_{mg})}{m_m - 1} \qquad (2.19)$$

My optimization routine combines the standard IDL function AMOEBA with IRT to search for the best combination of spectrograph parameters. In essence, the program evaluates the raytrace based on a merit function, and then explores parameter space using a downhill simplex method. For my optimization merit function I used the root-mean-squared (rms) value in the spectral direction (X). As I chose to ignore astigmatism, the Y rms is unconstrained in our merit function. I force the optimizer to check the X rms of our important spectral lines at 1022, 1032, and 1038 Å. Our optimizer is readily capable of achieving much higher resolution than our goal at one of these three lines, but at the sacrifice of the other two. This merit function ensures sufficient resolution across our bandpass. For tolerancing, I required that the rms of each line remain below the resolution limit for up to 50 μm piston of either the magnifier or grating. With the intended spring-mounting system for the optics (discussed in §2.5), the finest control possible over the optics' position is $\sim$10

- 20 μm, thus this tolerancing gave room for ease of alignment. R_g and e_g were held fixed while all other spectrograph parameters were allowed to vary.

The parameters for the final design are shown in Table 2.1. The ray trace spot diagrams are shown in Figure 2.4 for the wavelengths of interest. The majority of the rays are concentrated into tall lines smaller than 50 microns wide, spaced 50 microns apart, achieving $R = 60,000$ in our bandpass. This design has several advantages. Green et al. (1993) found a Cassegrain-like design with a hyperbolic magnifier. However, such an optic is difficult to align, and would create higher order aberrations that make it difficult to achieve high resolution. In my optimizations, I found values for e_m that were very close to zero, or a sphere. The use of a sphere as the magnifying optic greatly improves upon the shortcomings of a hyperbolic optic; for any fixed grating position, any misalignments in its pointing can be corrected by adjusting the magnifier in the direction of the optical axis. Therefore I set $e_m = 0$ to achieve the final numbers listed in Table 2.1. In addition, by ignoring astigmatism in optimization, the resulting tall spectral lines give us a valuable metric for alignment: misalignment of the grating causes the spectral lines to tilt relative to the spectral direction.

Table 2.1: Spectrograph/holographic parameters

Parameter	Value
R_g - grating radius	1000 mm
e_g - grating eccentricity	0
R_m - magnifier radius	-369 mm
e_m - magnifier eccentricity	0
d_{mg} - magnifier-grating distance	858 mm
Grooves/millimeter	4650
α - incident angle	21.28°
β - diffracted angle	6.67°
γ - incident angle of laser source 1	-69.25°
δ - incident angle of laser source 2	44.23°
r$_c$ - distance of laser source 1	-2537 mm
r$_d$ - distance of laser source 2	2106 mm
λ_0 - recording laser wavelength	3511 Å
η - detector angle	-22.6°
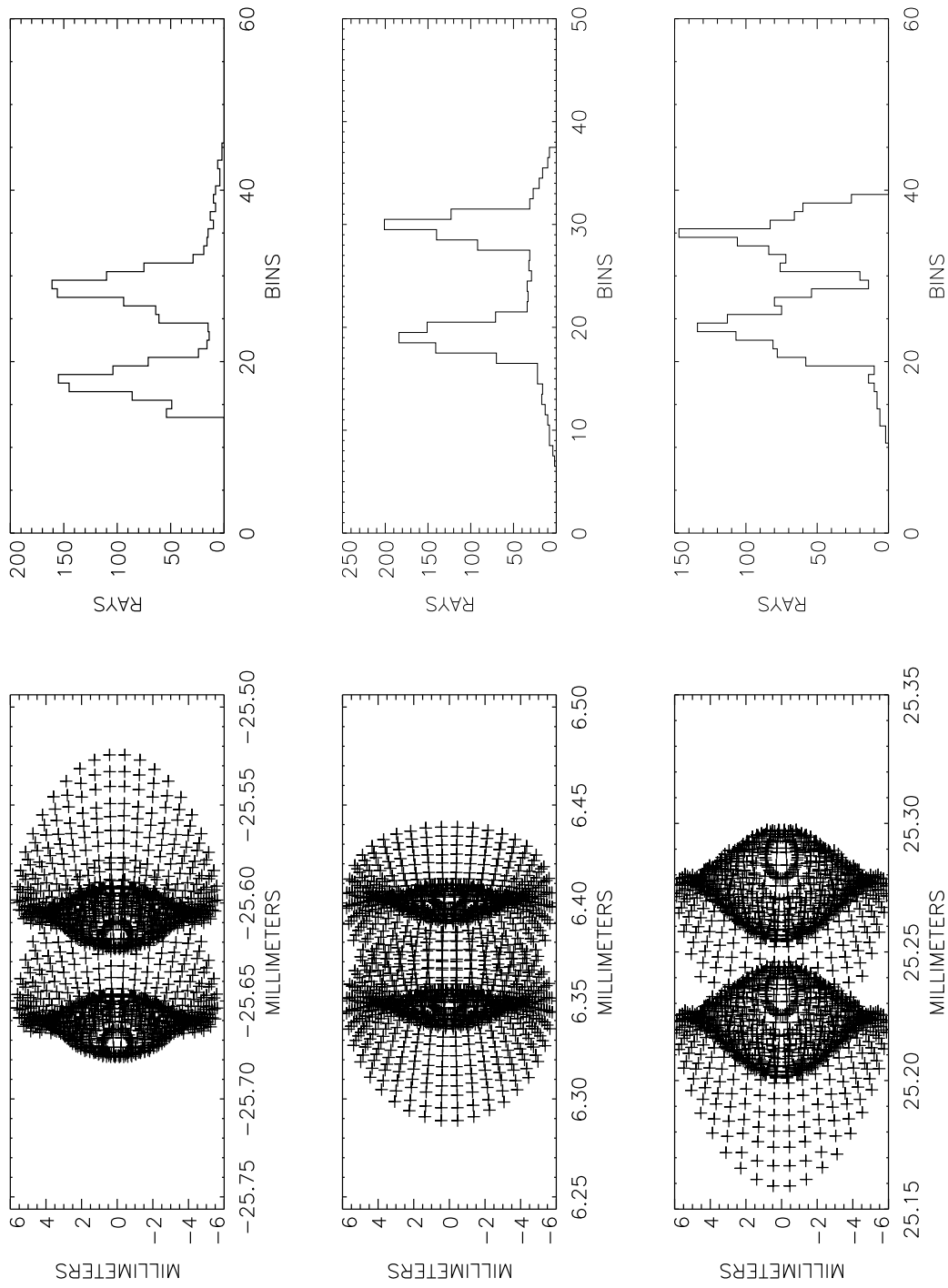
Figure 2.4: Spot diagrams (left) at 1022 Å (top), 1032 Å (middle), and 1038 Å (bottom) on the detector face. Histograms are shown on the right, with axes of number of rays vs. 5μm bins. Spots spaced by 0.017 Å (50 μm) yield a resolving power ($R = \lambda/\delta\lambda$) of 60,000.

42

Table 2.2: Physical optical parameters

Parameter	Value
d_{ps} - primary-secondary distance	500.1 mm
R_1 - primary radius	1730 mm
e_1 - primary eccentricity	1
R_2 - secondary radius	-1863 mm
e_2 - secondary eccentricity	4.1
back focal distance	100 mm
total focal length	1423 mm
plate scale	144.9 arc sec/mm

This design was made possible by allowing the entire optical system to be shifted off center inside the payload. The optical axis is shifted 3 inches from the payload axis, with a telescope primary of 8 inches. This allowed for a greater value of α than would have been possible if the optical axis were coincident with that of the payload. According to our previous calculation of minimum telescope collecting area, an 8 inch primary diameter was sufficient for reaching our desired S/N. The rest of the telescope parameters are listed in Table 2.2. Again, physical limitations determined these numbers. I set a compact overall length d_{ps} and an F/3 primary for ease of alignment and fabrication. The spectrograph required that the slit be no larger than 7 μm, as a magnification of 7 yields a 50 μm line. The already stated requirement that the slit be 1" forces the overall telescope focal length.

2.5   Mechanical Structure and Fabrication

The mechanical structure must allow the optics and detector to be mounted and alignable to within the raytraced tolerances. The telescope optics' final positions are set using three-point spring mounts. The optics are fixed to a mounting plate, which is held in spring compression. The springs are rated for 50 times the weight of the optic to prevent it from moving under 3 sigma g-forces ($\sim$45 g) during launch. Bolts run through the springs into a helicoiled base plate, yielding control of the optics positions to within the required tolerances. With such a mount, tip/tilt and Z positioning is possible. The magnifier's three-point mount is attached to a commercial XY stage,

made by OptoSigma. This enables adjustment of the magnifier in the XY directions relative to the grating/magnifier axis, to focus the spectrum onto the detector.

I chose aluminum for all structural components, as it is affordable and sufficiently strong to withstand typical launch loads. Solidworks models of the payload are shown in Figure 2.5. Large-scale structures position the optics within machine tolerances, all cantilevered off a primary bulkhead. A tube fixes the telescope secondary at the appropriate distance from the primary. In addition, another tube holds the star tracker next to the telescope. A space frame structure holds the spectrograph optics and detector. Six circular 1 inch diameter tubes are mounted to the bulkhead using clamped feet. Similar fixtures are used to attach the structural rings to the tubes. Pins are press-fit through the feet and tubes, constraining motion in the z-direction. The structural rings and disks are 15 inches in diameter, fitting inside the 17.26 inch skins. Vibration testing of the structure showed strong resonances at the top of the spaceframe, so Finite Element Modeling with Solidworks was used to identify which particular resonances in the space frame caused the amplification. This enabled us to design cross-braces to dampen out those resonant frequencies.

All optics in the payload are aluminum, chosen for several reasons. The aluminum is far less fragile than glass, leading to more relaxed mounting systems. Mounting holes can actually be drilled into the optics themselves, which we took advantage of in our mounts. In addition, matching the optic material to the material of the all-aluminum mechanical structure of the payload is beneficial. The equivalent coefficient of thermal expansion eliminates any mismatches between materials, loosening thermal constraints. Finally, aluminum can be diamond-turned to achieve the required surface, easier than grinding glass. Nu-Tek Precision Optical Corporation diamond-turned the optics, plated them with nickel, and re-diamond-turned and polished to ~ 15 Å RMS surface roughness at the correct prescription. The grating blank was sent to Horiba Jobin-Yvon for holographic ruling. The solution required a virtual source, with the first recording source on the opposite side of the grating from the second. To do this practically requires a diverging beam on the same side as the grating face. A glass master was used with photoresist on the concave spherical surface. This was replicated to a convex surface, and then onto the flight blank. All optics were
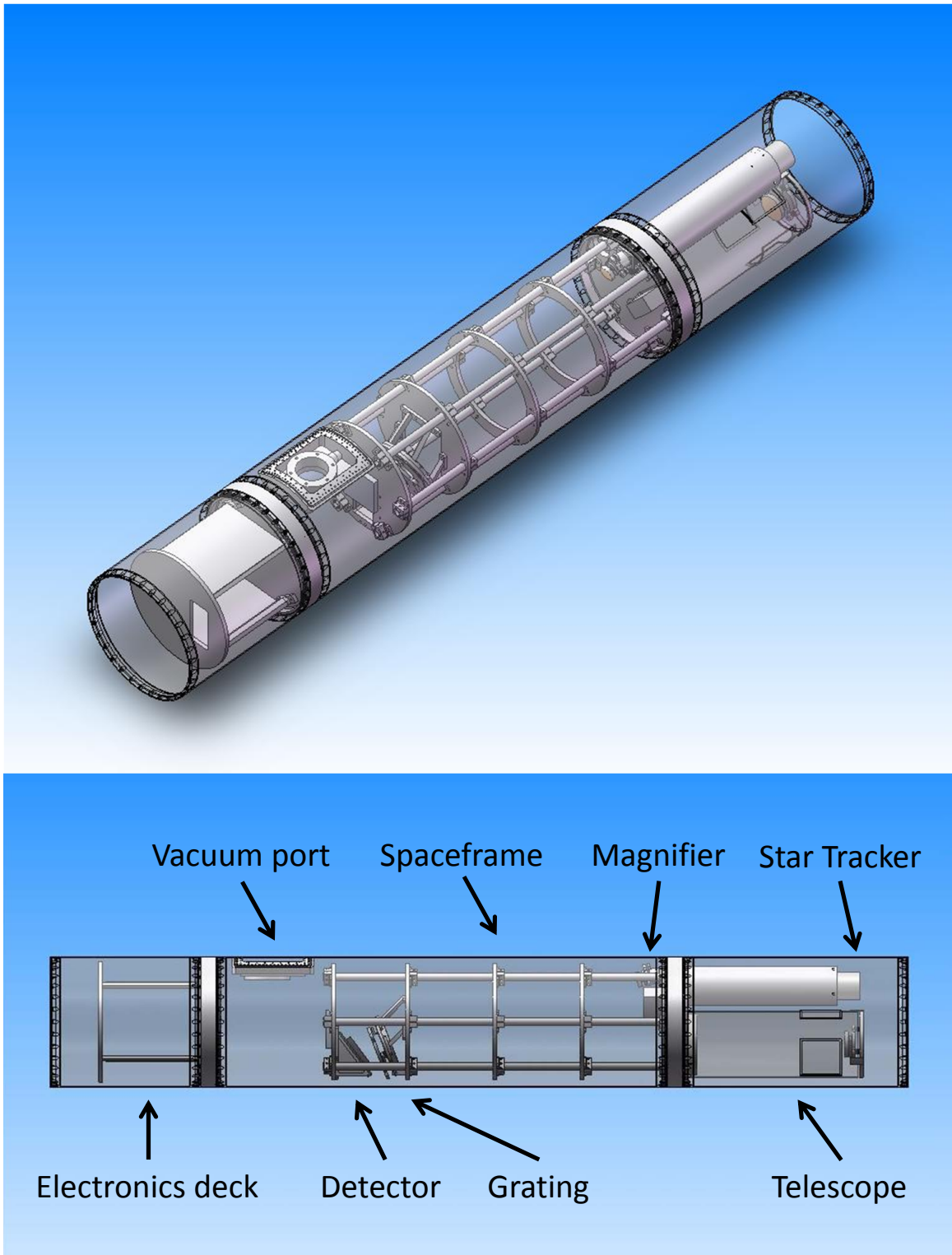
Figure 2.5: Solidworks models of the DICE payload, with transparent skins.

then coated with ∼60 nm of aluminum and ∼15 nm of LiF at Goddard Space Flight Center. I tested the efficiencies of each of our optics prior to alignment, and found them to be approximately 60% reflective.

2.6   Optical Alignment and Calibration

In visible light, I first aligned the telescope to the focal plane slit. There were several potential methods for doing this. Aiming a collimated light source at the telescope and using the Xybion image of the slit plane was a possibility, however the dynamic gain of the Xybion made it difficult to determine the true point spread function of the spot. Using a CCD at the telescope focus would also be difficult due to the minimum size of CCD pixels; I sought a spot size around 7 μm in diameter. In the end I used a knife-edge auto-collimating technique. Described in detail in Burgh et al. (2001), a slit and knife-edge were placed at the focal plane, equidistant from the optical axis. A CCD mounted on a linear stage behind the focal plane imaged the pupil for each position of the knife-edge (see Figure 2.6). I summed each image to measure the drop in intensity. The derivative of such a profile formed an approximate Gaussian line spread function, characterizing the telescope spot size in one direction. This proved to be an appropriate proxy for a full point spread function; by placing a CCD near the focus position of the telescope, I confirmed the spot was symmetric within 15%. Keeping the primary optic fixed relative to the slit/knife-edge plane, I adjusted the secondary position and formed a focus curve. At the best focus position I measured a full width at half maximum of $\sim$ 28 μm, or 4 arcseconds (as) at the telescope plate scale of 6.9 μm as^{-1}. With the slit size of 1.3" by 5.8" this would still allow $\sim$ 30% of the light through to the spectrograph. Due to the brightness of the targets, I found this slit loss to be acceptable.

As there were no convenient zero-order focus points with which to align the spectrograph, I had to do so at vacuum. Our 30 ft. x 3 ft. vacuum chamber has a 24 in. reverse Newtonian collimator inside. A low pressure gas discharge lamp placed behind a pinhole at the focus of the optical system creates FUV light when high voltage is applied to excite the molecules. Our instrument could be put in front of the resulting collimated beam for alignment. I used Ar/H$_2$
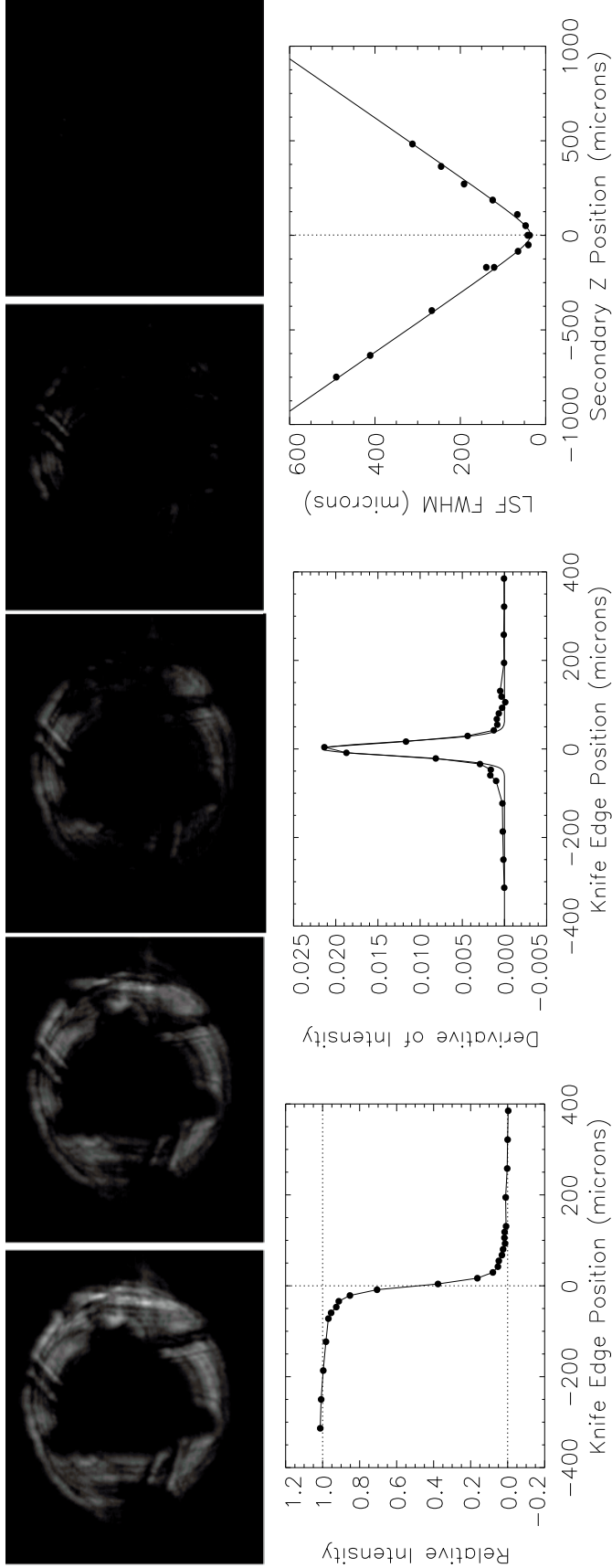
Figure 2.6: Knife-edge alignment of telescope: images of the pupil disappearing as the knife-edge cuts across the slit plane (top). Intensity drop with knife-edge position (bottom left), derivative of intensity (bottom middle), and focus curve (bottom right).

as the gas in the lamp for its Werner and Lyman band lines. H I Lyman β at 1025 Å provided a zeroeth order check of the spectrum's position on the detector. With the instrument inside the vacuum tank pumped down and the gas discharge lamp lit, I moved the spectrograph optics to improve the focus. Ray trace models predicted that any errors in the position of the grating could be corrected by adjusting the magnifier. I designed a mount for the magnifier that utilizes a trio of linear stages: one in the optical axis direction (Z), and the other two (X and Y) orthogonal to each other in the vertex plane of the magnifier.

While aligning the spectrograph, linear actuators were connected to the stages, enabling us to move the magnifier from outside the tank. This made it possible to measure spectra at different X, Y, and Z positions while maintaining vacuum on the payload. I kept the grating fixed in its initial mounting position, and moved the magnifier with the linear actuators. For each position, a spectrum was taken through the detector electronics. I fit Gaussians to the emission lines and assumed those to be the spectral line spread function. I used the average full width at half maximum for lines throughout the spectrum as a diagnostic to form a focus curve. Using this technique, I chose the minimum of the curve as the best z position for the magnifier. The spectrum for this configuration is shown in Figure 2.7. The bright line at left is H I Lyman β, and the rest of the vertical lines are H_2. The diagonal feature at right is field emission typical of these MCP detectors; such noise patterns are repeatable over long periods of time, and can be easily removed from flight data.

The spectrum shows our best measured resolving power of 31,000. The principal limitation to reaching the design goal of the spectrograph was the required small entrance slit size. A tradeoff had to be made between spectrograph resolution and instrument throughput. Any slit wider than 7 μm, when magnified by the factor of seven, would degrade spectral resolution. However, since the slit had to be at a 45° angle to accommodate the slit jaw camera and the slit substrate required a minimum thickness for rigidity, not as much light passed through from the telescope as expected. Due to launch window constraints, I opted for a larger slit, ensuring sufficient throughput while still doubling the resolution of previous observations of our targets. The original design goals were
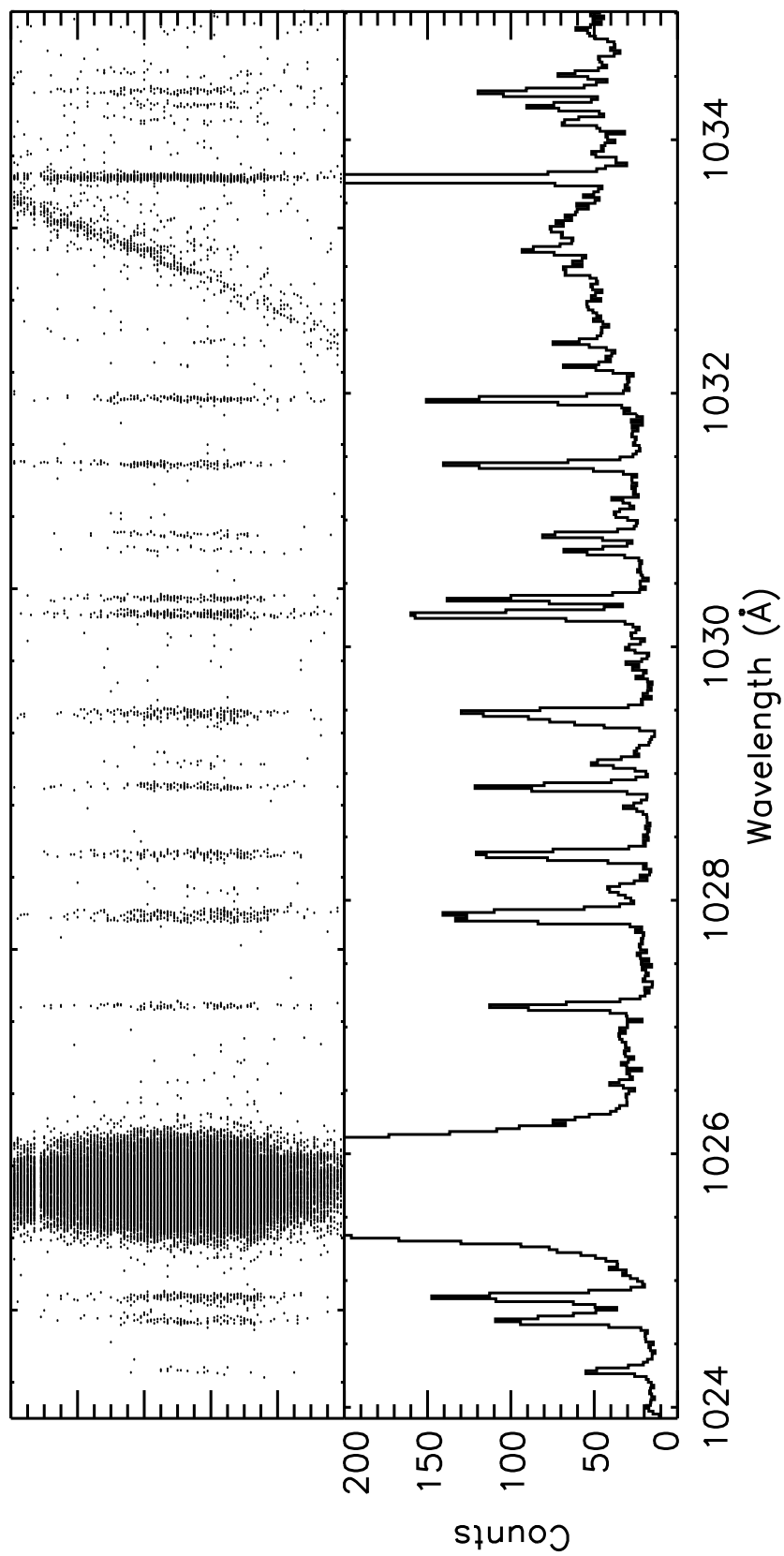
Figure 2.7: Partial detector image (top), and vertically summed H_2 spectra (bottom) for best-aligned position from 1020 Å to 1040 Å, $R \approx 31{,}000$.

5 - 15 km s^{-1} in order to both resolve narrow components and centroid their relative velocities. With $\sim$ 10 km s^{-1} resolution and the predicted S/N of 10, DICE could still outperform previous measurements of these targets.

2.7   Flight Results

DICE was first launched at 1:30 am MDT on on June 27th, 2009. During flight a dual failure occurred. As soon as the high voltage turned on, extremely high count-rates flooded the detector. The electronics that interface between our detector and the flight TM system were not designed to handle these count-rates. As a result, the handshaking between the two systems seized, halting any digital data transfer. Analog instrument diagnostics did reach the ground, however, allowing us to determine the problem. Upon recovery, we tested the instrument and demonstrated how high countrates can seize the flight electronics. However, we were not ever able to determine what caused the event in flight. Additional funding was secured to modify the electronics and refly approximately one year later.

The payload was launched on a Black Brant IX from White Sands Missile Range, at 3:00 am MDT on May 21st, 2010. During flight an anomaly occurred in the Black Brant motor, inducing an extreme vibration that far exceeded our design parameters for the optic mounts. Our optics were held in three-point spring mounts. This allowed the springs to be compressed enough to handle the load of the optics, while at the same time giving us the adjustability to align the optics. I chose the load values to give a safety factor of 4 times the standard vibration levels for a Black Brant IX. The anomaly induced a vibration profile (g^2/Hz) with $\sim$10 to $\sim$1000 times the specification values at specific frequencies. Figure 2.8 shows the accelerometer data in the Z, X, and Y directions. At t $\sim$ 32 seconds into flight, the rapid variances in acceleration can be seen.

During flight the global count rate decreased exponentially, however the noise pattern remained the same. From our pre-flight calibrations, I expected approximately 3,000 stellar spectra counts per second over the entire detector from both stars. During the time when the payload was moving between the two targets (t = +285 to +290 seconds), there was no significant change in
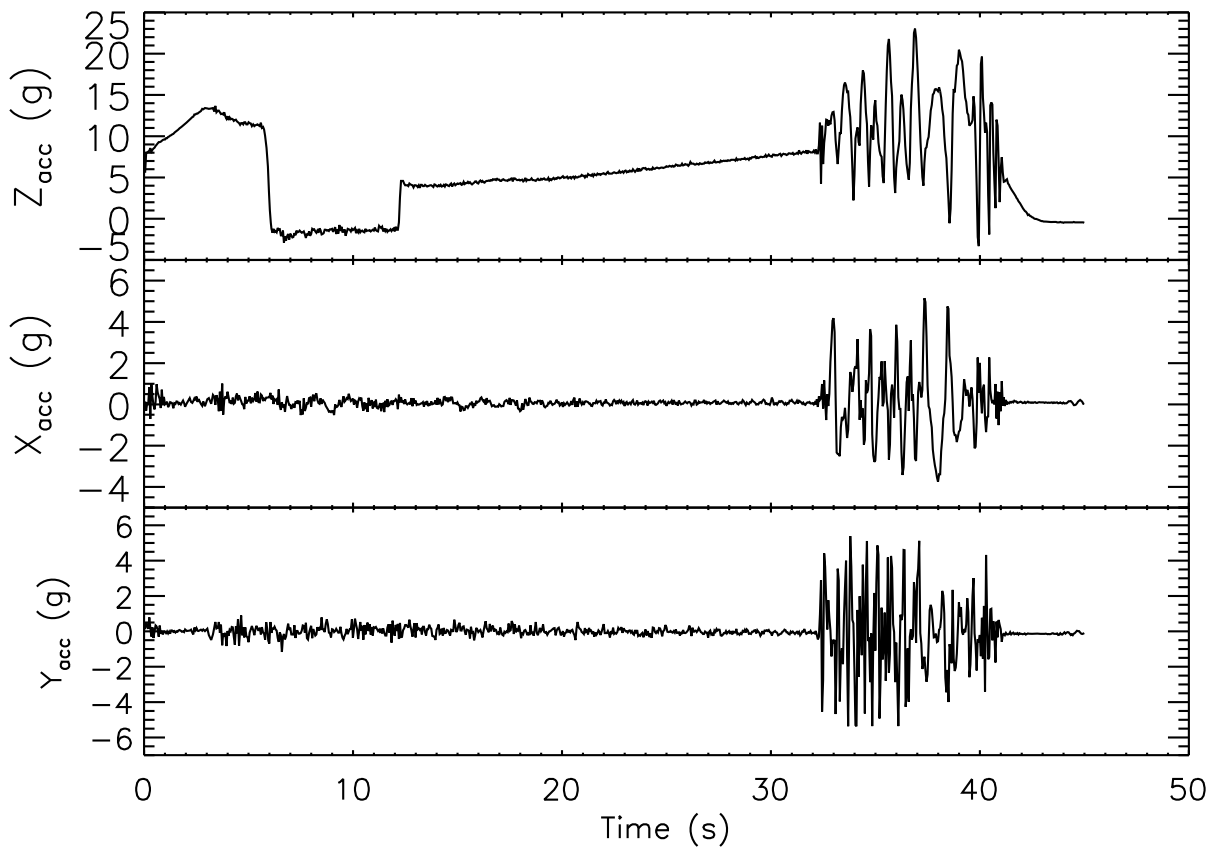
Figure 2.8: Flight accelerometer data for the Z (vertical), X, and Y directions. The burn anomaly occurs at t + 32 seconds.

the count rates. Post-flight calibrations in our vacuum tank facility showed no spectral lines from the H_2 gas in the hollow-cathode lamp. This information, combined with the flight data (detector, accelerometer, and vibrometer), implies that the optics were shaken out of alignment during the burn anomaly. The mysteries of O VI in the Local Bubble remain.

Chapter 3

COS observations of Carbon Monoxide in T Tauri Stars

The evolution of knowledge is toward simplicity, not complexity.

-L. Ron Hubbard

3.1   Introduction

Classical T Tauri stars (CTTSs) provide the opportunity to witness the birth of extra-solar systems. Their collapsed disks of gas and dust are the environments in which Jovian planets form, a process that we are only beginning to understand. From the ground, carbon monoxide (CO) is the easiest molecule to study in emission from these disks, and has been studied from near-IR to mm wavelengths (Salyk et al., 2008; Dutrey et al., 2008). Such observations sample regions from $r_{in} < 1$ AU (Najita et al., 2003) to $r_{out} > 800$ (Piétu et al., 2007). As the second most abundant molecule in the present day (after H_2), CO plays a significant role in extra-solar system formation. As H_2 does not emit strongly, CO is one of the most important tracers of disk gas. CO abundance varies greatly in different environments throughout the Milky Way. In the diffuse ISM, the CO/H_2 ratio ranges from 10^{-7} to 10^{-5} (Burgh et al., 2007); in dense clouds, it lies between 10^{-4} and 10^{-3} (Lacy et al., 1994), while comets in the solar system exhibit a ratio of over 10 (Lupu et al., 2007). During the process of star and planet formation, the CO and H_2 clearly must become removed from the gas phase in a way that increases the CO/H_2 ratio. By probing CO in protoplanetary disks, we can constrain models of solar system formation.

Electronic transitions of CO have recently been identified in the *HST*-COS spectra of several

CTTSs (France et al., 2011b). In each electronic transition, finer energy separations are possible, due to the additional vibrational (designated by v) and rotational (designated by J) modes. The upper and lower vibrational states are denoted v' and v", respectively. Similarly, rotational upper and lower levels are designated by J' and J"). Several vibrational bands of the $A^1\Pi$ - $X^1\Sigma^+$ (Fourth Positive) system have been measured in emission for V4046 Sgr and RECX 11, and in absorption in HN Tau. In CO, the different rotational levels are closely grouped amongst a given vibrational band, thus an entire band is often designated by (v' - v"). Lyα photons produced in the accretion funnel flow excite the CO electrons, populating its $X^1\Sigma^+$ v' = 14 state; the resulting (14 - 2) through (14 - 12) transitions are detected between 1280 Å and 1713 Å. Several bands they identify are shown in Figure 3.1.

In this chapter, as in the figure, I use femto-erg flux units (FEFU, where 1 FEFU = 1x10^{-15} ergs cm^{-2} s^{-1} Å^{-1}) as a standard flux unit. Although many of the individual rotational lines are not resolved, the blended emission bands vary enough with temperature (T_{CO}) and column density (N_{CO}) to place limits on these parameters. In V4046 Sgr, T_{CO} is constrained between 200 and 380 K, and N_{CO} between 3.3 and 7.9 x 10^{18} cm^{-2}. Circumstellar CO can be constrained in absorption as well; assuming a spherical distribution of CO around the star, a collisionally-excited distribution of gas at $T_{CO} = 500 \pm 200$ K is able to reproduce the HN Tau spectrum for $N_{CO} = 2\pm1$x10^{17} cm^{-2}. COS's high sensitivity and moderate spectral resolution also makes apparent the presence of the (v'=0,v"=1) 1600 Å and (v'=0,v"=1) 1713 Å band, which was originally assumed to be purely e-impact excited H$_2$ emission by Ingleby et al. (2009).

I extended this research by studying these and additional targets in greater detail. I present analysis of COS spectra for 12 CTTSs. My aim was to characterize T_{CO} and N_{CO} in a variety of CTTSs, so as to find correlations between the UV-emitting CO and the disk properties that characterize these systems. The UV-emitting CO can also be compared with CO previously detected in these disks with IR and mm radiation. I modeled the Lyα radiation field assuming absorption from an outflow and interstellar H I, using this as an input for simple fluorescence models. These models enabled us to estimate T_{CO} and N_{CO} for targets with strong, high S/N CO emission. For
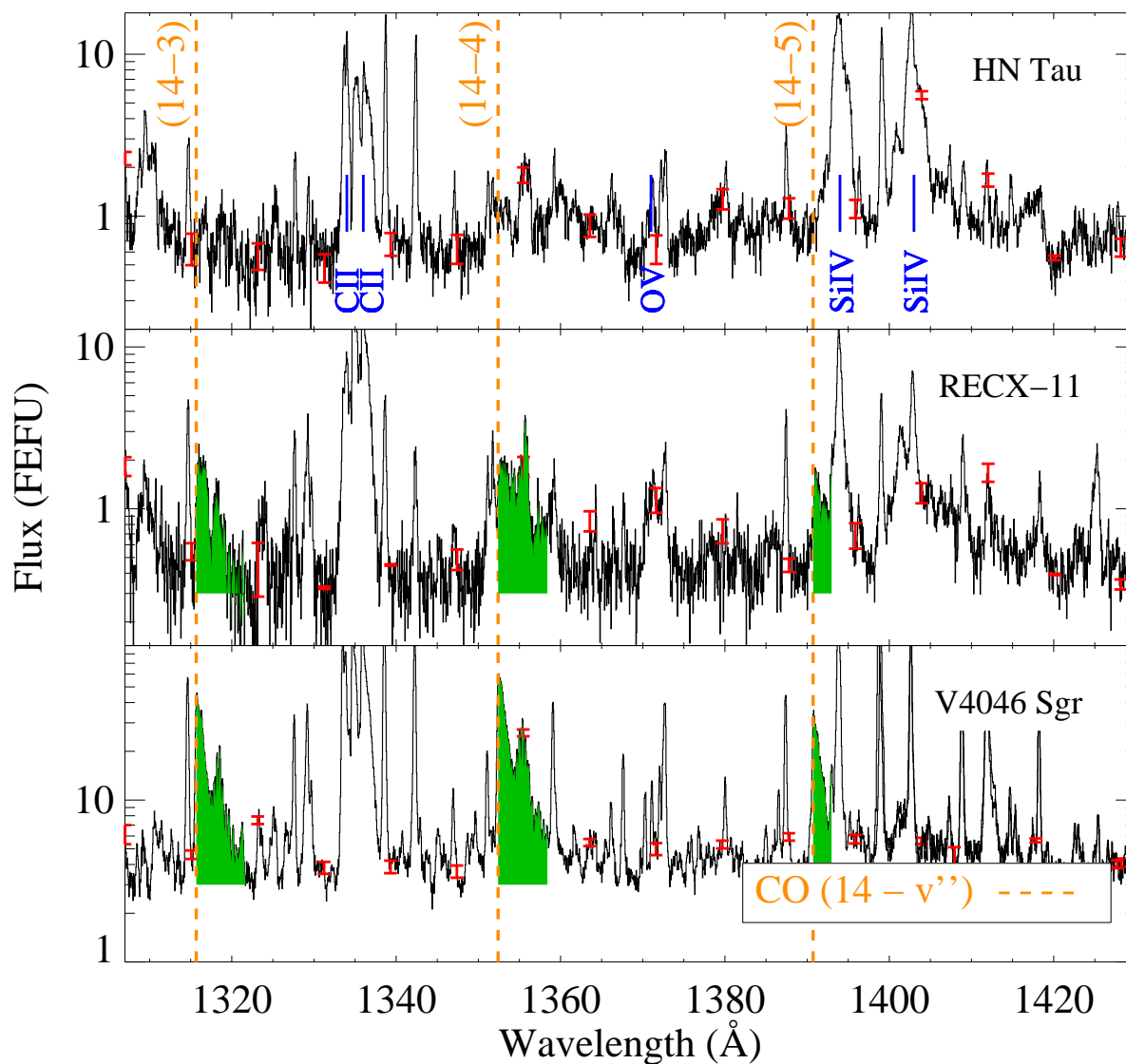
Figure 3.1: CO A-X emission bands in green for three CTTSs. The bandheads (the lowest J transitions) are identified with dashed lines, and contaminating emission lines in blue. Figure from France et al. (2011b)

targets where there is no appreciable evidence of emission above a continuum, I calculated upper limits for the CO column density. In §3.2 I detail the COS observations, as well as the individual targets in this survey. In §3.3 I summarize the methods implemented in France et al. (2011b), describing the physics behind the production of these CO emission bands. I also introduce my model for the Lyα profiles. In §3.4 I discuss the results of this analysis, and my ability to constrain the temperatures and column densities of CO in each of the targets. I compare these empirically derived properties with other previously measured parameters from the literature in §3.5.

3.2   Observations and Targets

I analyzed *HST*-COS spectra of 1 WTTS and 12 CTTSs; the observational parameters are listed in Table 3.1. These were the first targets observed with COS, available at the time of analysis. Spectra from several of these targets have already been presented in the literature. Ingleby et al. (2011) studied accretion rates in RECX11 and RECX1, and Yang et al. (2011) demonstrated Lyα photon absorption and re-emission by H_2 in V4046 Sgr. France et al. (2011a) characterized the continuum emission of V4046 Sgr and DF Tau, while France et al. (2011b) identified CO fourth positive emission and absorption in the spectra of V4046 Sgr, RECX 11, and HN Tau. Each spectra consists of 2-4 orbits with the G130M and G160M gratings (Osterman et al., 2010), yielding a moderate resolving power of $\lambda/\delta\lambda \sim$18,000. As there is no field stop in the instrument, the entire objects were sampled without appreciable spatial resolution relative to the size of the disks.

I used CALCOS, the COS calibration pipeline, to reduce the data and then created coadded spectra from 1140 Å to 1760 Å. Once T_{CO} and N_{CO} were measured, it was important to find any correlations with other properties of the CTTSs which could be useful in future classification. Table 3.2 lists a variety of target parameters relevant to this work. These are the visible extinction (A_V), accretion rates ($\dot{M}$), disk inner radius (R_{in}), and disk mass (M_{disk}). A_V is representative of the dust extinction, which decreases overall flux in the visible and UV. It is necessary for modeling, in order to correctly calibrate flux levels. In main sequence stars, it is determined by comparing the expected stellar blackbody flux with the actual measured spectrum. However, CTTS spectra

Table 3.1: *HST*-COS observing log

Object	R.A. (J2000)	Dec. (J2000)	Date	COS Mode	T_{exp} (s)
RECX 11	08^h 47^m 01.28^s	-78° 59' 34.1"	2009 December 12	G130M	3645
RECX 11	08^h 47^m 01.28^s	-78° 59' 34.1"	2009 December 12	G160M	4514
RECX 15	08^h 43^m 18.43^s	-79° 05' 17.7"	2010 February 5	G130M	3891
RECX 15	08^h 43^m 18.43^s	-79° 05' 17.7"	2010 February 5	G160M	4502
V4046 Sgr	18^h 14^m 10.49^s	-32° 47' 34.2"	2010 April 27	G130M	4504
V4046 Sgr	18^h 14^m 10.49^s	-32° 47' 34.2"	2010 April 27	G160M	5581
DM Tau	04^h 33^m 48.74^s	+18 ° 10' 09.7"	2010 August 22	G130M	3459
DM Tau	04^h 33^m 48.74^s	+18° 10' 09.7"	2010 August 22	G160M	3770
DE Tau	04^h 21^m 55.69^s	+27° 55' 06.1"	2010 August 20	G130M	2068
DE Tau	04^h 21^m 55.69^s	+27° 55' 06.1"	2010 August 20	G160M	1851
HD135344B	15^h 15^m 48.42^s	-37° 09' 16.3"	2010 March 14	G130M	2666
HD135344B	15^h 15^m 48.42^s	-37° 09' 16.3"	2010 March 14	G160M	4836
HN Tau	04^h 33^m 39.37^s	+17° 51' 52.1"	2010 February 10	G130M	5725
HN Tau	04^h 33^m 39.37^s	+17° 51' 52.1"	2010 February 10	G160M	4529
DR Tau	04^h 47^m 06.22^s	+16° 58' 42.6"	2010 February 10	G130M	1704
DR Tau	04^h 47^m 06.22^s	+16° 58' 42.6"	2010 February 10	G160M	1746
DK Tau	04^h 30^m 44.25^s	+26° 01' 24.5"	2010 February 4	G130M	1585
DK Tau	04^h 30^m 44.25^s	+26° 01' 24.5"	2010 February 4	G160M	1971
DF Tau	04^h 27^m 02.81^s	+25° 42' 22.1"	2010 January 11	G130M	4828
DF Tau	04^h 27^m 02.81^s	+25° 42' 22.1"	2010 January 11	G160M	5549
LkCa15	04^h 39^m 17.79^s	+22° 21' 03.1"	2010 February 5	G130M	1712
LkCa15	04^h 39^m 17.79^s	+22° 21' 03.1"	2010 February 5	G160M	1725
GM Aur	04^h 55^m 10.98^s	+30° 21' 59.1"	2010 August 19	G130M	2128
GM Aur	04^h 55^m 10.98^s	+30° 21' 59.1"	2010 August 19	G160M	1861
RECX 1	08^h 36^m 56.12^s	-78° 56' 45.3"	2010 January 22	G130M	2945
RECX 1	08^h 36^m 56.12^s	-78° 56' 45.3"	2010 January 22	G160M	1857

Table 3.2: Target Parameters

Object	Spectral Type	Group	d (pc)	A_V	$\dot{M}(10^{-8}M_\odot yr^{-1})$	i (°)	R_{in} (AU)	$M_{disk}(M_\odot)$	References
RECX 11	K6.5	η Cha	97	0	0.03	70	R_*	< 0.05 − 5	5,10,16
RECX 15	M3.4	η Cha	97	0	0.1	60	R_*	0.05-5	5,11
V4046 Sgr	K5 + K7[4]	Isolated	83	0	1.3	35	4	4.5e	6,9,12
DM Tau	M1	Taurus-Aur	140	0	1.12	36	3	0.05	3,7,13,18
DE Tau	M0	Taurus-Aur	140	0.62	2.64	70	-	0.005	1,14
HD135344B	F4	Isolated	140	0.3	0.54	21	39	0.003	4,17
HN Tau	K5+M4	Taurus-Aur	140	0.65	0.13	> 70	-	0.0007	1,20
DR Tau	K4	Taurus-Aur	140	1.2	3.16	72	0.01	0.02	2,8,15,21
DK Tau	K9 + M0	Taurus-Aur	140	1.42	3.79	70	0.05	0.005	1,21
DF Tau	M1+M3.5[10]	Taurus-Aur	140	0.5	17.69	80	-	0.0004	1,19
LkCa15	K5	Taurus-Aur	140	.62	0.13	48	-	0.03	3,7,13
GM Aur	K7	Taurus-Aur	140	0.96	0.3	54	24	0.025	1,13,18
RECX 1	K7 + M0	η Cha	97	0	-	-	-	-	5

(1) Gullbring et al. (1998); (2) Gullbring et al. (2000); (3) Kenyon & Hartmann (1995); (4) Garcia Lopez et al. (2006); (5) Lawson et al. (2004); (6) Stempels & Gahm (2004); (7) Hartmann et al. (1998); (8) White & Ghez (2001); (9) France et al. (2011b); (10) Ingleby et al. 2011; (11) Sicilia-Aguilar et al. (2009); (12) Rodriguez et al. (2010); (13) Guilloteau et al. (2011); (14) Ricci et al. (2010); (15) Andrews & Williams (2007); (16)Gautier et al. (2008); (17) Brown et al. (2009); (18) Calvet et al. (2005); (19) Ardila et al. (2002); (20) Andrews & Williams (2005); (21) Eisner et al. (2010)

contain excess emission from the accretion shock and disk. Hartigan et al (1989) first devised a method to quantify the amount of veiling in a star, which occurs when continuous emission from the magnetospheric shock fills in intrinsic stellar absorption lines. Thus the accretion spectra can be characterized by measuring the ratio of the observed line to a line expected from an assumed stellar photospheric spectrum.

Accretion rates are typically estimated by measuring the emission due to material funneling into the star. Lawson et al. (2004) run magnetospheric accretion models, constrained by Hα profiles. Generally, the broader and brighter the Hα emission, the higher the accretion rate. These are uncertain to within a factor of 3-5. The Hydrogen Paβ and Brγ transitions are also useful measures of accretion. Veiling is another metric for accretion, as higher accretion rates release more optical and UV continuum radiation, potentially overwhelming photospheric emission.

The disk inner radius is the inner cutoff radius for the disk, inward of which there is no appreciable dust. This inner clearing of material is usually evidence of disk evolution, and could be indicative of planet formation. Radiative transfer models predict SEDs with flux deficits between 2 - 8 μm for disks with inner clearing. High resolution spectral profiles can reveal holes, as the absence of close-in material may correspond to a lack of emission from hot, fast moving gas. Geometric modeling with IR or mm interferometric imaging can also constrain the radius, although spatial resolution is often inadequate for small radii. Frequently multiple methods are combined to yield a self-consistent answer.

The mass of the disk is usually calculated with the IR to mm dust emission, as it is the easiest observable from the ground. H$_2$ dominates the mass of the disk, but the dust acts as a sufficient proxy with certain assumptions. By estimating the mass of the IR-emitting dust, applying dust/gas mass ratios will yield the total mass of the disk. Assuming an optically thin outer disk, its mm emission can be used to model a surface density inward towards the star (Beckwith et al., 1990), and therefore yield an integrated dust disk mass. These masses can be off by a factor of 2, potentially underestimated due to the lack of information about optical thickness in the inner disk. Some use CO measurements combined with an assumed CO/H$_2$ ratio to calculate disk masses; however

photodissociation and freezing can change the ratio from its interstellar value.

I provide a review below of the targets and their properties that have already been studied in the literature. Most targets belong to the η Chamaeleontis and Taurus-Auriga star formation regions, and I describe them by region.

3.2.1 η Chamaeleontis Targets

The η Chamaeleontis cluster is located at a distance of $\sim$97 pc, and was originally identified as a pre-main sequence group through its X-ray emission (Mamajek et al., 1999). Age estimates of its constituent stars range from 4 - 10 Myr (Lawson et al., 2001). It is unusual in several ways when compared to other star forming regions. Sicilia-Aguilar et al. (2009) measured a disk fraction of $\sim$50%, much higher than expected for an older region; previous observations of other clusters imply that disks typically disappear over a timescale of 3-4 Myr (Haisch et al., 2001). This may be linked to the higher percentage of single stars in η Chamaeleontis. In addition, very few brown dwarf or lower mass objects were detected compared to high-mass stars for a typical star formation initial mass function (Luhman, 2004). There is also a higher percentage of disk systems in transition objects than found in other clusters (Megeath et al., 2005). These targets were observed under *HST* program 11616 (P.I. - G. Herczeg).

3.2.1.1 RECX 1

RECX 1 is a binary system comprised of a K7 and M0 star at a separation of 20 AU (Brandeker et al., 2006). I use RECX 1 as a control case, as it does not have a circumstellar gas disk. This is evidenced by its lack of molecular emission lines, and Hα EW of 1.3 Å. Therefore any emission lines found in its spectrum can be considered stellar, and are later noted for line identification in the CTTSs. The details of this process are discussed in §3.3.2.

3.2.1.2   RECX 11

RECX 11's status as a CTTS is controversial; H_2 UV emission implies the presence of gas (France et al., 2011b), but the standard optical accretion indicators are questionable. Lawson et al. (2004) used magnetospheric accretion models to calculate accretion rates and disc inclinations, given previously measured stellar parameters. The Hα *EW* is only 3.0 Å, right at the boundary between CTTSs and WTTSs. On the other hand, RECX 11 also shows a red-shifted infall absorption feature, typical of CTTSs. Hα variability yields velocities for the accreting gas which match infall speeds for the assumed stellar mass, supporting the model of magnetospheric accretion. Its low accretion rate ($\dot{M} = 4\mathrm{x}10^{-11} M_\odot yr^{-1}$) would imply that photoevaporation should have cleared the inner disk, but this is not seen. Ingleby et al. (2011) find similarly low accretion values from *HST* COS data, and argue that negligible planet formation has occured during the disk evolution. From H_2 line profiles, they measure rotational velocities fast enough to be as close as 3 R_*.

3.2.1.3   RECX 15

RECX 15 is a strong accretor; the Hα *EW* is 90.0 Å, and its profile is indicative of a blue-shifted wind component (Lawson et al., 2004). Lawson et al. (2002) recorded time variable emission, finding a 12 day period with fluctuating amplitudes. Accretion models with hotspots on the stellar surface could account for this. The SED implies a continuous disk from close to the stellar surface out to tens of AU or more, where the disk flares strongly (Gautier et al., 2008). In an attempt to measure the disk mass, Ramsay Howat & Greaves (2007) measured the H_2 v=1-0 S(1) emission line. The line width implies an origin at a few AU from the star. Assuming optically thin gas in thermal equilibrium with a temperature of 1500 K at 10-30 AU, they calculated a disk mass of $0.5\mathrm{x}10^{-8} M_\odot$. This mass is low because the H_2 measured is the hot gas, likely only a small fraction of that in the entire disk. Bary et al. (2003) created scaling factors to account for this, which when applied to RECX 15 extend the range to 0.05 - 5 $M_\odot$.

3.2.2   Taurus-Auriga Targets

The Taurus-Auriga complex is one of the nearest star forming regions at a distance of $\sim$140 pc. As such, many studies have been performed on its hundreds of constituent YSOs, providing excellent statistics on star formation. Its paucity of O/B stars, combined with a low interstellar radiation field, enable the persistence of many disks. Disk fractions in the Taurus region have been measured from $\sim$ 45% for low-mass objects (M=0.01-0.3 $M_\odot$) to $\sim$75% for solar-mass stars (Luhman et al., 2010). Kenyon & Hartmann (1995) performed the first comprehensive survey of the region, finding that most of the YSOs are clumped together in dense molecular clouds. Some of these objects have been studied in exceptional detail, while others have only been measured in large surveys. DF Tau was observed as part of the COS GTO program (P.I. - J. Green), and the rest were observed under *HST* program 11616 (P.I. - G. Herczeg).

3.2.2.1   DM Tau

DM Tau is considered to be a transitional disk due to its flux deficit shortward of 8 μm. This disk is unusual in that it has both an inner disk hole and a significant accretion rate. Spitzer spectra imply an inner hole of a few AU with little dust inside this region (0.0007 lunar masses), although with a detectable accretion rate ($\sim$1.3x10$^{-8}M_\odot yr^{-1}$) there must be gas present (Calvet et al., 2005). The clearing may be due to photoevaporation, an already-formed planet, or magneto rotational instability (MRI) clearing. The sparse inner cavity also agrees with the absence of K-band veiling and photospheric NIR emission (Espaillat et al., 2010). In addition, lower limits placed on the inner disk radius with interferometry and photometric K band excess could mean that emission is from scattered starlight rather than dust emission (Pott et al., 2010). The disk exhibits a rich chemistry; organic molecules CO, CN, CS, HCN, HNC, HCO$^+$, C$_2$H, and N$_2$H$^+$ have been measured in emission (Dutrey et al., 1997). The abundances of these molecules show that stellar photons have the strongest influence over their creation and destruction. Bergin et al. (2010) tentatively measured H$_2$O emission, and the line width implies an origin within 10 AU.

3.2.2.2   HN Tau

HN Tau is a binary system (0.7 and 0.4 M$_\odot$) with strong jets that expand with distance from the primary star (Hartigan et al. 2004). Its constituent stars are slightly older than the estimated 1-2 Myr age of the Taurus region, at $\sim$ 2 and 4 Myr for HN Tau A and B, respectively (Kraus & Hillenbrand, 2009). In this work I study only the spectrum of HN Tau A, due to its separation from HN Tau B. While its exact inclination is not known, it does exhibit an unusually large amount of reddening (Furlan et al., 2006), which could imply extra dust from an edge-on disk. M-band observations from NIRSPEC on Keck reveal weak CO emission, but strong absorption (Brown, private communication). In addition, France et al. (2011b) measure CO electronic transition detected in absorption, which would be indicative of disk gas viewed at high inclination.

3.2.2.3   DR Tau

DR Tau is a K4 star with accretion rates that appear to vary by over two orders of magnitude (Gullbring et al., 2000; Johns-Krull & Gafford, 2002). The amplitudes of the measured optical and near-IR variability, combined with its U-band excess, indicate that the emission may come from the disk in addition to the accretion shocks (Eiroa et al., 2002). The mid-IR SED slope and weak 10μm silicate emission suggests that the disk is evolved, although there is not a significant inner hole as is typically found in a transition object (Przygodda et al., 2003). DR Tau shows strong molecular emission at IR wavelengths. Rotational transition emission lines of H_2O are seen, in high Js 20-50, as well as CO and OH at temperatures around 1000 K (Salyk et al., 2008). By modeling the gas as an isothermal LTE ring, the emission radii are 1.0, 0.8, and 0.7 AU for H_2O, CO, and OH, respectively. Time-lapsed CO measurements show variability between emission and absorption, indicating a complicated radiative transfer problem between the accretion shock and the disk (Lorenzetti et al., 2009).

3.2.2.4   DK Tau

DK Tau is a binary system consisting of a K9 and M0 with ~350 AU separation; from mm imaging both appear to have individual circumstellar disks (Jensen & Akeson, 2003). Unlike the majority of binary systems in which both stars contain disks, the A and B disks may be misaligned (Kraus & Hillenbrand, 2009). The disks show evidence of growth of both dust grains and crystalline silicates, unusual for their relatively young age (Furlan et al., 2006). V-band variability has been observed, which can be explained by spot accretion emission on the star (Eiroa et al., 2002), whereas combined spectroscopic photometry of both disks implies there is no variability in disk emission (Eisner et al., 2007). Not much molecular emission has been measured in the DK Tau disks, but Greaves (2005) did detect sub-mm ^{13}CO emission.

3.2.2.5   DF Tau

A binary pair (M1 + M3.5) with 13 AU separation, DF Tau may be as young as 0.1 Myr (Ghez et al., 1997). However, its circumbinary disk shows evidence of dust settling in its SED, typically a sign of significant disk evolution (Sargent et al., 2009). Strong accretion has been measured from a UV continuum (Herczeg et al., 2006), as have UV H_2 emission lines. H_2 appears both in $Ly\alpha$/C IV pumped emission, and in absorption in an outflow (Yang et al., 2011). Herczeg & Hillenbrand (2008) reported less emission and accretion measured than in Herczeg et al. (2006) by 0.1-0.2 dex implying varying accretion rates. This variability implies that most accretion occurs in the heavier primary. DF Tau displays a rich spectrum of CO IR emission lines; the CO (1 - 0) R(3) shows a FWHM of ~ 74 km s^{-1}, implying a close orbit to the star (Najita et al., 2003). Greaves (2005) also detect sub-mm emission from ^{13}CO.

3.2.2.6   LkCa15

LkCa15 is a pre-transitional CTTS with a ringed gap in its disk. From mid-IR imaging the inner rim of the outer dust disk is calculated to be 46 AU, and the outer rim of the inner disk is ~10 AU (Thalmann et al., 2010). Hydrodynamic models suggest that a 13 - 21 M_J planet at a

radius of 14 - 28 AU could explain the observed gap. Espaillat et al. (2008) agree with such an assessment by ruling out other methods of creating disk gaps and holes; MRI clears disk material from the inside-out, contradictory to the presence of an inner disk. Similarly, photoevaporation cannot account for the inner disk if it were to be responsible for the large 46 AU outer disk rim. Najita et al. (2003) measured fundamental CO emission as close as 0.1 AU, agreeing with the Thalmann et al. (2010) detection of dust at the dust sublimation radius. Spitzer Mid IR emission is indicative of grain composition similar to that found in the interstellar medium, unusual for such an older system (Watson et al., 2009).

3.2.2.7   GM Aur

GM Aur is a massive transition disk; the Spitzer Infrared Spectrograph (IRS) SED is best explained by 0.02 lunar masses of dust within a 5 AU inner disk, and an outer disk with a 24 AU inner radius (Calvet et al., 2005). An already formed planet most likely explains the gap over the other possibilities of grain growth, photoevaporation, and Magneto-Rotational Instability (MRI) clearing. Using Keck interferometry, Akeson et al. (2005) estimate a truncation of the inner dust disk at 0.2 AU, approximately the dust destruction radius for GM Aur's measured stellar properties. Gas emission reveals even more about the structure and composition of this CTTS. Salyk et al. (2007) measured near-IR CO emission within $0.2^{+0.4}_{-0.2}$ AU, at high rotational temperatures, coincident with the measured dust inner rim. Ne II, an excellent gas tracer, was measured in the surrounding disk at the systemic velocity of 14.8 km s^{-1} (Najita et al., 2009). Along with a profile broadened by rotational velocity, this would suggest an origin from the disk as in TW Hya Herczeg et al. (2004).

3.2.3   Isolated Targets

Two of the targets do not reside in star-forming regions. V4046 Sagittarius was observed as part of the COS GTO program (P.I. - J. Green). It is a ∼9 Myr old CTTS, a closely orbiting (∼ 9 R$_\odot$ separation) binary at a distance of 83 pc. The dust continuum emission implies a hole

of radius 0.2 AU, and a peak of 37 K dust grains $\sim$40 AU from the center (Jensen & Mathieu, 1997). Models of a Keplarian disk in hydrostatic equilibrium imply an inclination angle of 33-37° for a central binary mass of 1.4 - 1.8 M$_\odot$ (Stempels & Gahm, 2004; Quast et al., 2000). The disk appears to be coplanar with the central binary stars (Monin et al., 2007). Kastner et al. (2008) measured molecular mm emission lines from CO, HCN, CN, and HCO$_+$; the double peaked CO profiles confirm Keplarian rotation. Rodriguez et al. (2010) imaged the system in ^{12}CO(2-1) and ^{13}CO(2-1) millimeter emission, measuring the molecular disk extent to $\sim$ 370 AU and mass of $\sim$ 110 Earth masses. They calculated the gas mass from the measured CO line intensities and a CO/H$_2$ ratio of 10^{-4}. Quast et al. (2000) detected photometric variability from the Hα profile, implying changing rates of accretion.

HD 135344B was observed under *HST* program 11828 (P.I. - A. Brown). It is part of a visual binary, and has a disk with a gap from .45 to 45 AU (Brown et al., 2007). Grady et al. (2009) performed a comprehensive study of this system using HST coronography, FUV spectra and images, X-ray spectra, and SED modeling. They measure an inner ring of warm dust from 0.08 - 0.31 AU, agreeing with the submm imaging. There is also weak silicate emission, potentially due to grain growth. Interferometric and SED fitting imply that the inner and outer disks are inclined to one another. CO has been detected in emission inside the hole out to $\sim$15 AU, although no other molecules are seen (Pontoppidan et al., 2010; Brown et al., 2009). The distribution of gas column densities agree with models of a jovian planet orbiting between 10 and 20 AU, although photoevaporation without shielding dust could also decrease the CO (Pontoppidan et al., 2008). The fact that the CO (v'=2 - v"=1) transition is not detected, while the (v'=1 - v"=0) is, would suggest that the CO is not UV fluoresced.

3.3   Methods and Analysis

3.3.1   Lyα-pumped CO emission

Characterizing the nature of the UV-emitting CO in these disks requires a knowledge of their column density N_{CO} and temperature T_{CO}. In order to calculate these values for the sample, I use a method similar to that implemented by France et al. (2011b). Here I briefly summarize their technique. For the target V4046 Sgr, Figure 3.2 provides an overview of the process by which CO absorbs and then re-emits Lyα photons. The CO A - X (14 - 0) rotational transitions are shown in the top panel. The ground state rotational levels, J", are plotted as a function of wavelength for the Q branch (J'-J"=0), R branch (J'-J"=1), and P branch (J'-J"=-1). In the cold circumstellar disk environment, the CO population is predominantly in its ground vibrational state (v' = 0). The middle panel of Figure 3.2 shows the (14 - 0) transitions overlaid on the V4046 Sgr Lyα profile. Terrestrial Lyα airglow is subtracted out. With the v'=14 state of the A electronic level populated by Lyα photons, the electrons rapidly (A(v' - v") $\sim 10^5 - 10^7$ s^{-1}) fall down to lower vibrational states of the X electronic level, according to the appropriate branching ratios.

The bottom panel shows one of the resulting emission bands, (14 - 3) at 1315 Å. An H$_2$ emission line lies at $\sim$1314.6 Å, but a strong sawtooth profile is evident starting at $\sim$1315.6 Å. This edge, or bandhead, is due to the lower J" levels, which pile up at this wavelength as seen in the top panel. The higher rotational levels are better resolved, and can be seen as more distinct individual features. These are identified by the R(J") states underneath the individual features. The nature of the (14 - 3) emission can be explained by the Lyα profile: the "middle" J" states (such as R(J") = 6 - 15) fall at wavelengths where there is depleted Lyα flux. As there are fewer photons to absorb, there are less in emission.

The green curve on the bottom panel shows their best-fit model CO flux, calculated by using the observed Lyα profile as the incident radiation field. This was a reasonable assumption, as there is negligible extinction (A$_V \sim$ 0) towards the target, and therefore little N$_H$ (< 1x10^{18} cm^{-2}). to absorb additional flux in the profile. The Lyα emission is absorbed by the CO as per the standard
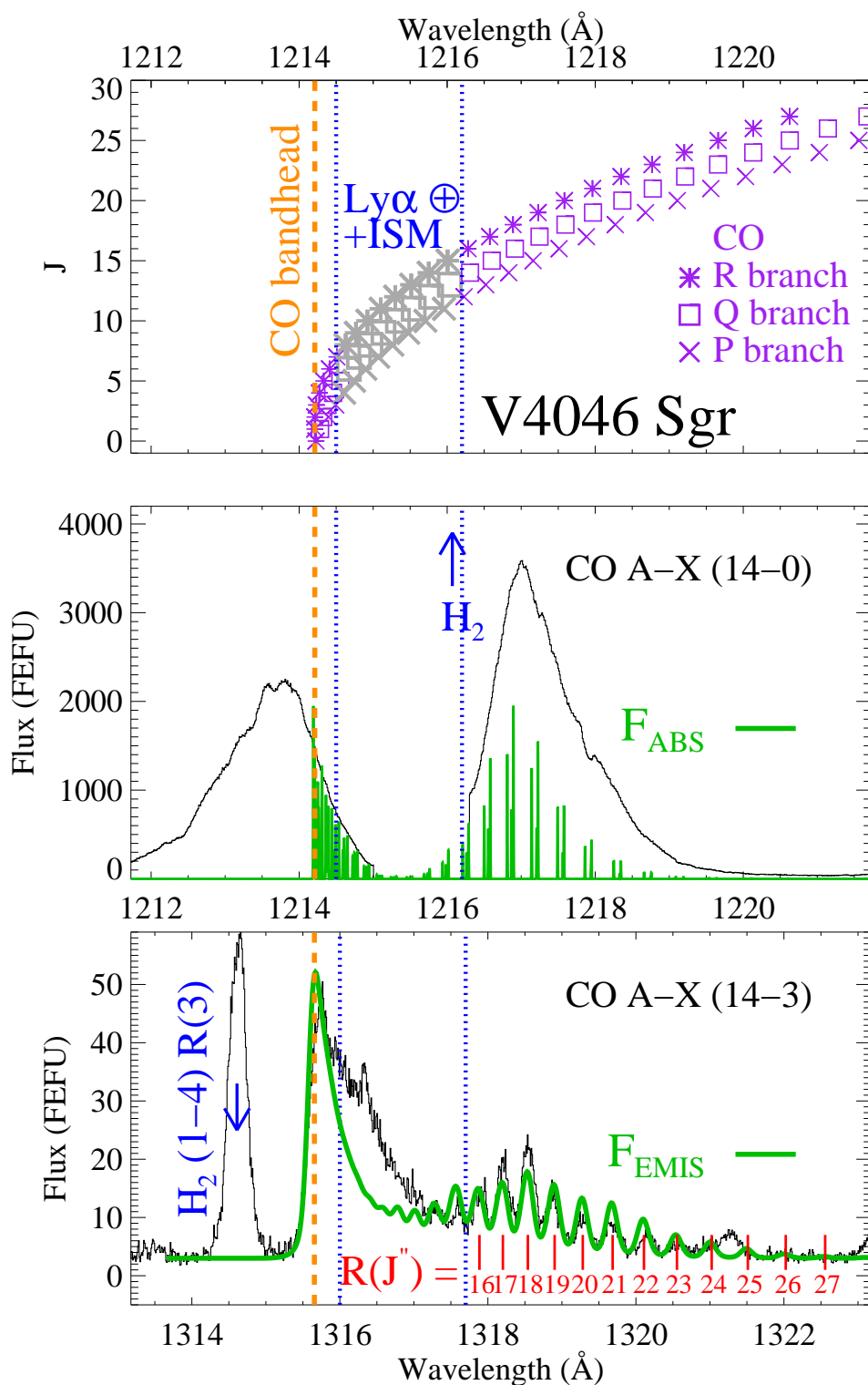
Figure 3.2: Top: Wavelength positions for the different J level absorption transitions of the CO (14 - 0) band. Middle: V4046 Sgr Lyα emission profile. Terrestrial Lyman α has been zeroed out. Green vertical lines indicate absorption transition positions. Bottom: 1315 Å (v'=14,v"=3) emission band resulting from Lyα pumping. Higher J emission transitions are marked in red, and green shows best-fit model from France et al. (2011b).

radiative transfer equation:

$$I_\lambda = I_\lambda^0 (1 - e^{-\tau_\lambda}) \tag{3.1}$$

where τ_ν is the CO optical depth:

$$\tau_\lambda = \frac{\pi e^2}{m_e c} f_\lambda N_J \phi(\lambda) \tag{3.2}$$

Here e is the electron charge, m_e the electron mass, and c the speed of light. I use oscillator strengths f_λ, which corresponds to the strength of a transition, from Kurucz (1993), and the Voigt profile $\phi(\lambda)$ is dominated by doppler broadening. This is a reasonable assumption, as the observed line widths (~ 20 km s^{-1}) would require temperatures greater than 10^5 K, much higher than the CO dissociation temperature. N$_J$ is the column density of CO molecules in a rotational state J:

$$\frac{N_J}{N_{CO}} = \frac{(2J+1)e^{-B[J(J+1)]hc/kT_{CO}}}{Q_r} \tag{3.3}$$

where N_{CO} is the total column density of CO in the ground vibrational state v"=0. k is the Boltzmann constant, h is the Planck constant, and B the rotational constant for CO (1.923 cm^{-1}). T_{CO} is the gas temperature, and Q_r is the rotational partition function, kT_{CO}/hcB (Herzberg, 1950). Thus, the resulting spectra are entirely dependant on N_{CO}, T_{CO}, and f_λ, given a certain exciting radiation field. This simple model assumes that the electronic ground state can be described by a thermal population characterized by a single T_{CO}. In order to approximate the Lyα emission hidden by geocoronal Lyα, a parabola was fit to the inside of the profile. This model resulted in the green line of the bottom panel; χ^2 fits constrain N_{CO} and T_{CO} to within $\sim 40\%$.

However, not all CTTSs are alike; the exciting Lyman α radiation fields, N_{CO}, T_{CO}, and corresponding CO emission bands can differ. Figures 3.3 and 3.4 show the Lyman α profiles and 1315 Å CO bands for all the CTTSs in the sample. In DF Tau, weak blueward Lyman α emission correlates to the lack of bandhead emission in its CO band. This correlation between red and blue emission is seen in most targets with significant CO emission. However, attempts to apply the

France et al. (2011b) method to the other targets demonstrate the need for a more sophisticated estimation of the incident Lyα radiation. For example, targets with higher extinction ($A_V > 0.5$) require extremely large amounts of CO ($N_{CO} > 10^{22}$ cm^{-2}) to reproduce the observed 1315 Å emission, implying that interstellar reddening prevents us from measuring the shape and strength of the local Lyα radiation field in these systems.

I therefore introduce a straight-forward model of the physical situation, shown in Figure 3.5, which I use to re-construct the incident radiation. A disk surrounds the protostar, onto which accreting material falls. Lyα emission is created at the funnel flows near the stellar surface, as well as in the photosphere itself. The plot in Figure 3.5 shows the model Lyα profile for V4046 Sgr in red. I approximate the Lyα profile $I_{Ly\alpha}$ as the sum of two gaussians (chosen to simplify parameterization) above a continuum $C_{Ly\alpha}$:

$$I_{Ly\alpha} = C_{Ly\alpha} + I_1(0)e^{-(\frac{\lambda-\lambda_1}{2\sigma_1})^2} + I_2(0)e^{-(\frac{\lambda-\lambda_2}{2\sigma_2})^2} \tag{3.4}$$

where $I_1(0)$ and $I_2(0)$ are the amplitudes (in FEFUS) at the central wavelengths λ_1 and λ_2. I fix λ_1 to be at rest, while λ_2 is a variable parameter, corresponding to the accretion flow emission. An outflow exists between the star and the CO, containing H I which absorbs some of the Lyα photons:

$$I_\lambda^0 = I_{Ly\alpha}e^{-\tau_{out}} \tag{3.5}$$

It is this profile that I use as the incident radiation for the CO in Equation 3.1. The H I column density in this outflow, N_{out}, determines τ_{out} according to Equation 3.2. This radiation is then further absorbed by interstellar H I, producing the emission seen:

$$I_{obs} = I_\lambda^0 e^{-\tau_{ISM}} \tag{3.6}$$

where τ_{ISM} is determined by N_{ISM} at rest velocity. A_V values from Table 3.2 were used to deredden the data, according to the extinction curve from Cardelli et al. (1989). In star-forming regions, a
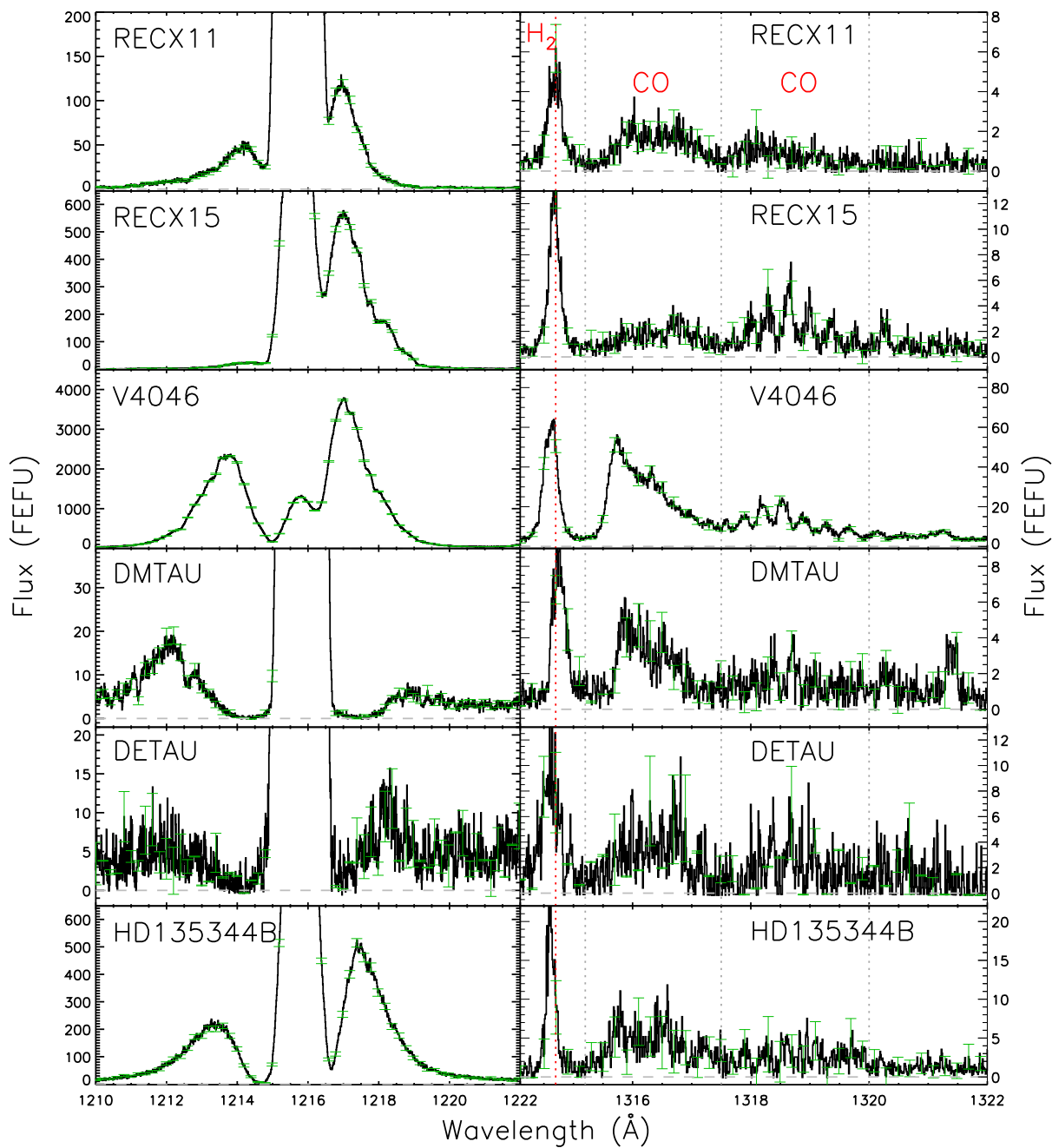
Figure 3.3: Extinction-corrected Lyα profiles (left column) with terrestrial airglow, and CO (14 - 3) emission bands (right) for each of the sample targets. In CO bands, an H_2 line is identified with a vertical dashed red line, and the dashed grey lines bound the blue and red sides of the (14 - 3) band.
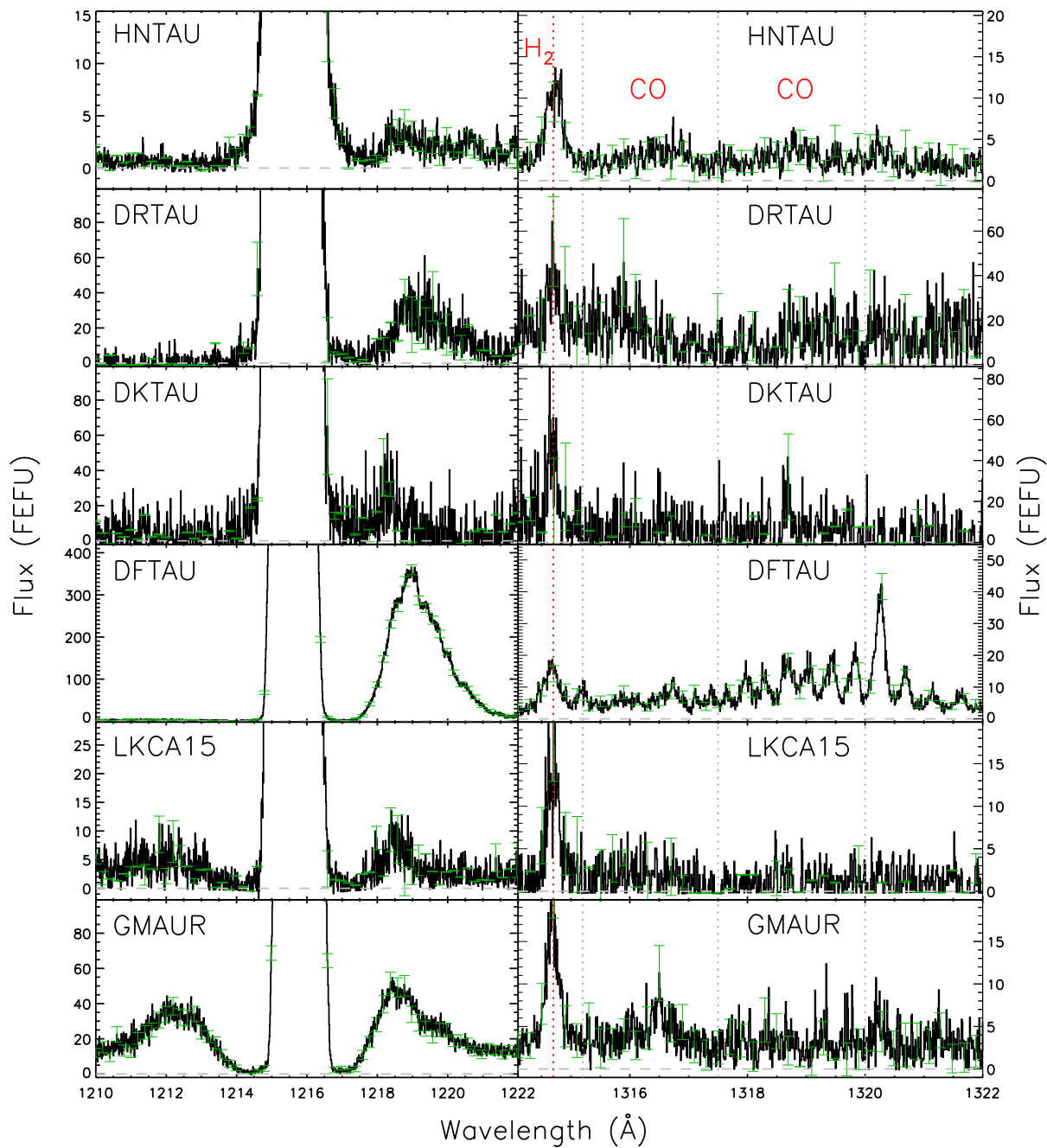
Figure 3.4: Extinction-corrected Lyα profiles (left column) with terrestrial airglow, and CO (14 - 3) emission bands (right) for each of the sample targets. In CO bands, an H$_2$ line is identified with a vertical dashed red line, and the dashed grey lines bound the blue and red sides of the (14 - 3) band.
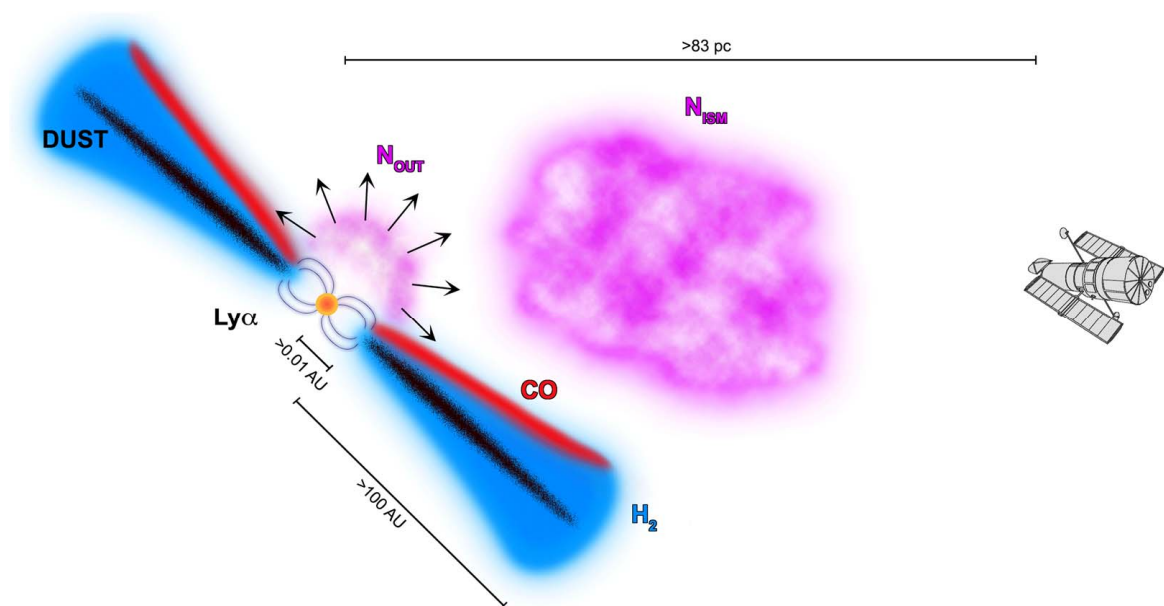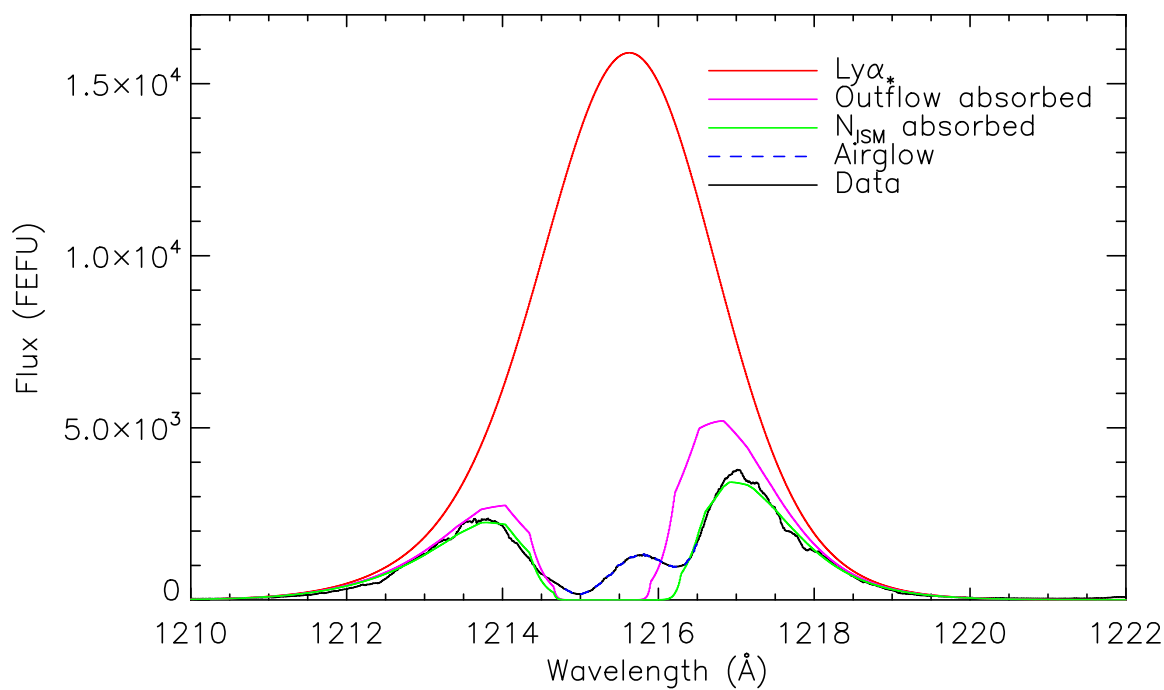
Figure 3.5: V4046 Sgr Lyα data with overlaid model profiles (top), and drawing of disk that produces the flux we see (bottom). Lyα emission (red profile) is created near the star, then absorbed by an outflow (magenta profile), and additionally absorbed by interstellar medium H I (green profile) to produce the observed data. The CO in the disk sees the outflow-absorbed emission.

range of R$_V$ values have been measured, from the interstellar value, 3.1, to as high as 5.5 (Whittet et al., 2001; Chapman et al., 2009). I therefore use an intermediary value of R$_V$ = 4.0.

With the de-reddened data, I perform a Levenberg-Marquardt least-squares fit to this model, allowing $I_1(0)$, $I_2(0)$, σ_1, σ_2, λ_2, v_{out}, N_{out}, and N_{ISM} to vary. To demonstrate the way in which the observed Lyα profile constrains these parameters, I used a Monte Carlo technique to estimate ranges for the fit parameters. For DF Tau, Figure 3.6 shows the results for v_{out} of 40, 60, 80, and 100 km s^{-1} and a single gaussian emission component. The Lyα FWHM ($2.35\sigma_1$) is tightly constrained about 878 km s^{-1} for a 20% variation of Lyα amplitude. This is because the red side of the Lyα red wing constrains the maximum amount of Lyα allowed, before it is absorbed by intervening material. For future discussion, I refer to the Lyα emission on the red side of the absorption trough as the "red wing", and the emission on the blue side the "blue wing".

The remaining three panels show how a given Lyα intensity limits the total amount of absorbing material ($N_{ISM} + N_{out}$) possible. The blue side of the Lyα red wing constrains the total amount of absorbing material required. In this way, it is the combination of Lyα emission and intervening material absorption that is constrained by the data; if there is too much emission, no amount of absorption can bring the resulting profile down to match the red side. Likewise, if there is too much column density, no amount of emission can bring the profile up to meet the blue side. The sharp linear dependency between N_{ISM} and N_{out} in the lower right corner demonstrates how the velocity of the absorber limits the balance between N_{ISM} and N_{out}. The further blueshifted the absorber is, the more N_{out} is required for a given N_{ISM} to combine and absorb enough emission to fit with the blue side.

Due to the number of parameters, there are a variety of combinations which yield a good fit to the data. Therefore I use each Lyα profile for separate fits with the CO band data, with the same model as in France et al. (2011b). Again, I use a Levenberg-Marquardt least-squares fit to the de-reddened data. The variable parameters in the CO model are the gas rotational temperature (T_{CO}), column density (N_{CO}), and the velocity broadening of the absorbing gas (b_{broad}). For a continuum level, I use the average continuum level from nearby areas of the spectrum. For targets
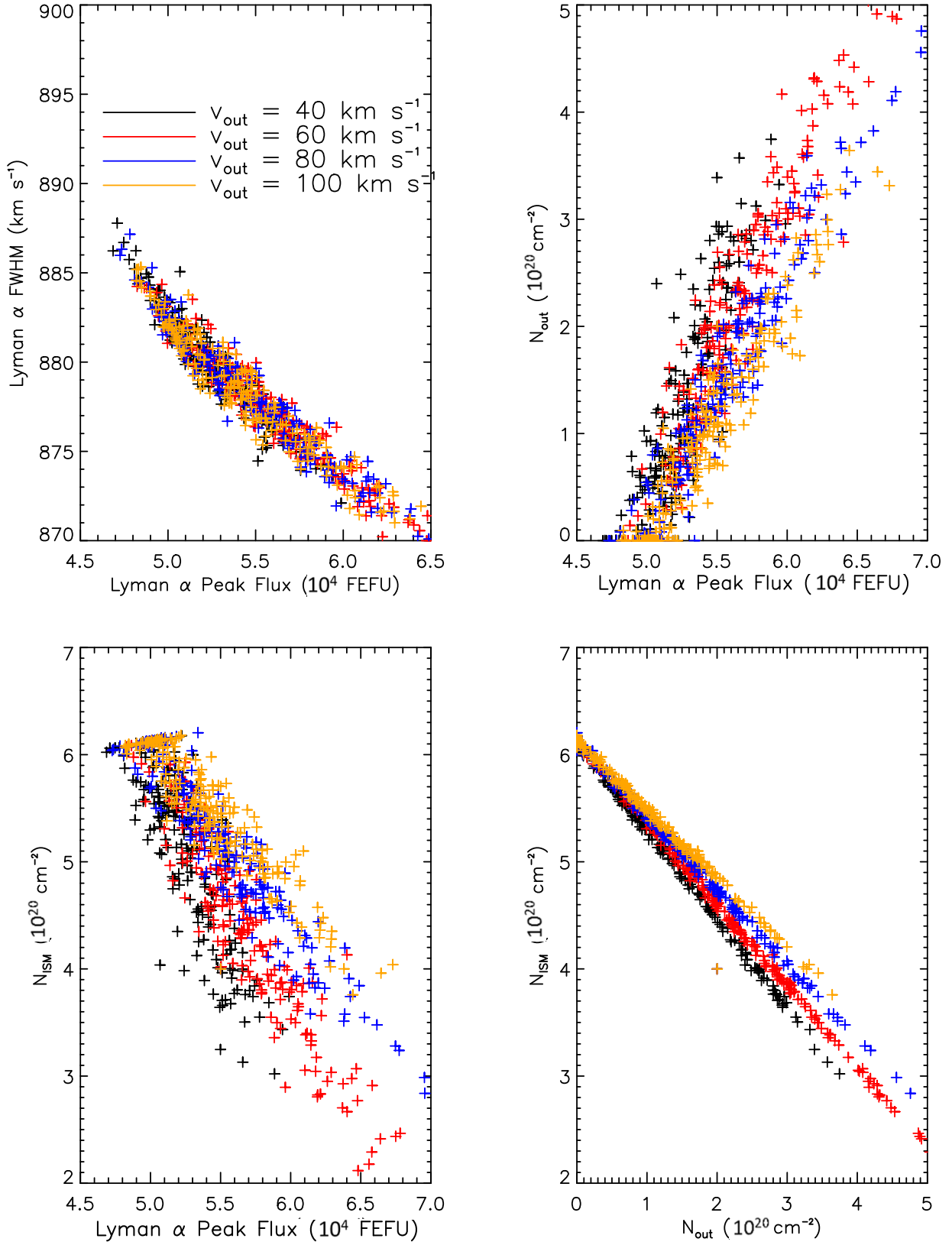
Figure 3.6: Best fit parameters for Monte Carlo fitting of DF Tau Lyα profile. Each color represents a different outflow velocity, which was held constant for fitting.

with marginal to strong emission, the CO bandhead and higher J lines constrain the radial velocity. The results are shown in §3.4.

Several caveats are worth mentioning in this method. Some Lyα profiles had to be fit to spline-interpolated estimations of the data. RECX 15, for example, shows weak absorption features in the red wing. These were identified as H_2 in the spectrum of V4046 Sgr and DF Tau (Yang et al., 2011). While small, such features can affect the least-square fits for data with sufficient S/N spectra. Therefore, I perform spline-interpolations of the unabsorbed portions of the Lyman wings. Also, the 1315 Å region of the spectra are created at the overlap of two detector regions in the instrument. The effect of coadding these two spectra, combined with the low signal to noise, caused some flux error bars to be too small. This unnecessarily weights those points, driving the least squares fits. Thus, any errors that were three times smaller than the average error were set to the value of the standard deviation of the continuum.

3.3.2 Contaminating Emission

There are many emission lines in these spectra from other molecules or atoms which can confuse any attempts to measure CO emission. The bands identified in France et al. (2011b) are listed in Table 3.3. Many of them are detected in several of the targets, but most are heavily contaminated. Fortunately, the strongest CO emission bands contain the fewest contaminating lines in the targets: the 1315 Å (v=14,v=3), 1352 Å (v=14, v"=4), and 1391 Å (v=14, v=5) bands. Herczeg et al. (2002) catalogued H_2 emission in the spectrum of TW Hydrae; I note those lines which fall in these best bands in Table 3.4, along with the integrated fluxes from their paper. They identified a number of "unknown" lines which most likely correspond to the CO emission lines observed in the targets. In addition to the H_2 lines, I use the spectrum of the WTTS RECX 1 (shown in Figure 3.7), to identify chromospheric and transition region lines typical of a solar mass protostar. RECX 1 exhibits neither molecular emission nor evidence of active accretion (Ingleby et al. 2011). Any emission lines present should be due to the star; as low mass YSOs are close in mass and composition, I can expect similar stellar emission from the targets in the sample. These

lines are identified for the wavebands of interest in Table 3.5.

Table 3.3: CO Fourth Positive bands identified in sample CTTSs.

Band ID	λ_0 (Å)	Pumping Source	λ_{pump} (Å)	A(v' - v") (s^{-1})	B(v' - v")
(14 - 2)	1280.5	H I Lyα	1214 - 1220	2.3×10^6	0.04
(14 - 3)	1315.7	H I Lyα	1214 - 1220	8.6×10^6	0.17
(14 - 4)	1352.4	H I Lyα	1214 - 1220	1.5×10^7	0.30
(14 - 5)	1390.7	H I Lyα	1214 - 1220	8.9×10^6	0.17
(14 - 7)	1472.6	H I Lyα	1214 - 1220	5.4×10^6	0.10
(14 - 8)	1516.3	H I Lyα	1214 - 1220	2.9×10^6	0.06
(14 - 10)	1610.1	H I Lyα	1214 - 1220	3.2×10^6	0.06
(14 - 12)	1713.2	H I Lyα	1214 - 1220	2.2×10^6	0.04
(0 - 1)	1597.3	C IV, C I, e$^-$	1544 - 1550, 1657	2.4×10^7	0.33
(0 - 2)	1653.2	C IV, C I, e$^-$	1544 - 1550, 1657	2.0×10^7	0.27
(0 - 3)	1712.4	C IV, C I, e$^-$	1544 - 1550, 1657	1.0×10^7	0.14

The 1390 Å band is strongly contaminated by Si IV and H_2 in all targets, and only the blue side of the band can be used for comparison. The O I in the 1352 Å band appears strongly in over half the targets. Thus I only use the 1315 Å band for fitting all targets. RECX 15, V4046 Sgr, and DM Tau do not display prominent O I emission, so I also fit those bands in these targets. The same Lyα profiles as the 1315 Å band are used for these fits. In the 1315 Å band I choose the fitting regions carefully to avoid the 1316.55 and 1320.22 Å H_2 lines. Table 3.6 lists the fit ranges for each target, for both the Lyα and CO fits. For all targets, it is necessary to include the bandhead, as it constrains N_{CO} for low T_{CO}. Conversely, the high J lines from 1317 to 1320 Å must be included, as they constrain T_{CO} for a given value of N_{CO}. The range between 1316 and 1317 Å is excluded; the fits at these wavelengths are highly uncertain due to lack of knowledge of the pumping flux for those transitions.
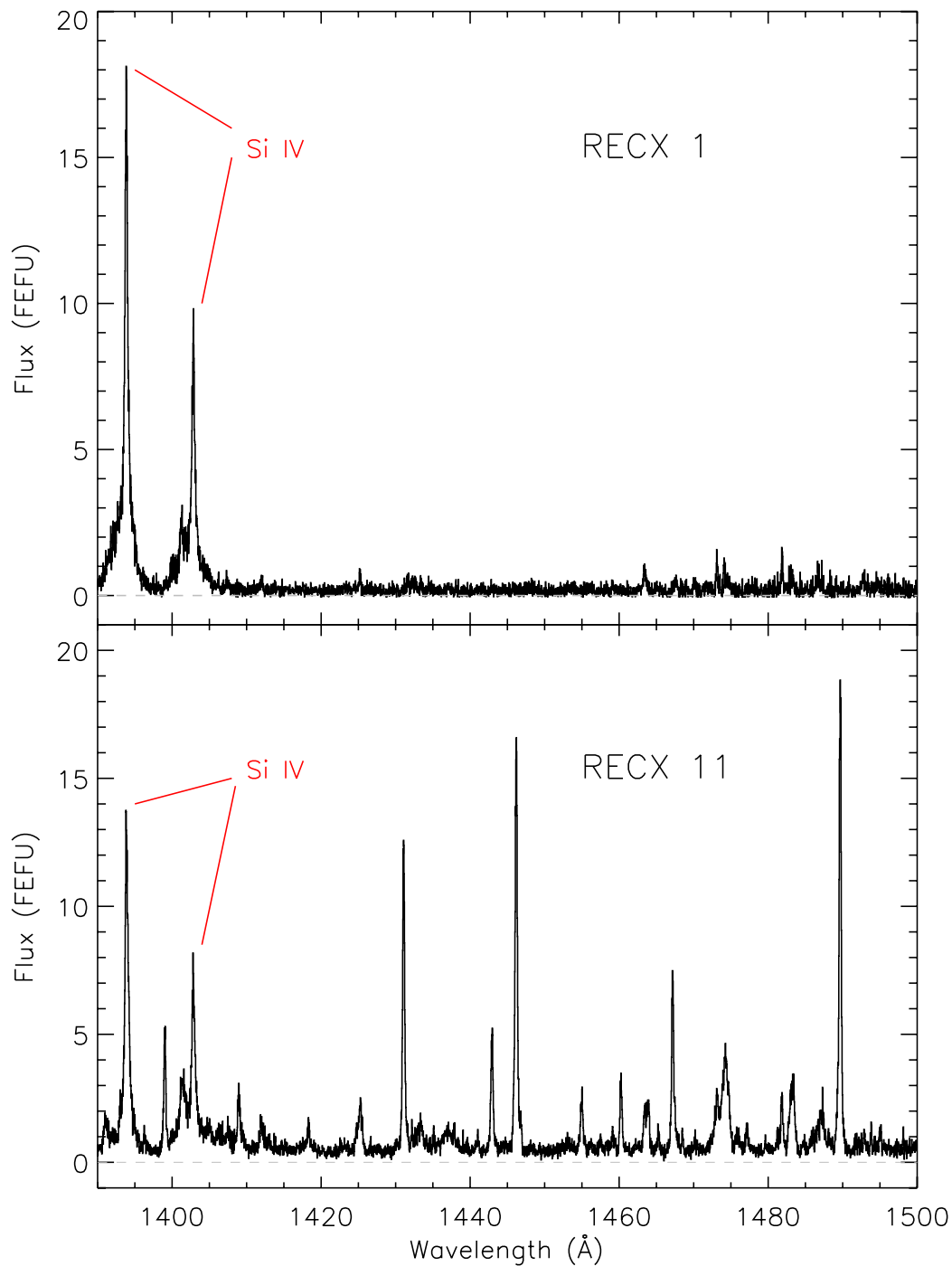
Figure 3.7: COS spectra of the WTTS RECX 1 (top) and CTTS RECX 11 (bottom). H_2 emission lines are seen in the RECX 11 spectra, as expected from a circumstellar gas disk.

Table 3.4: TW Hya H$_2$ Contaminating Emission

Wavelength (Å)	Line ID	Flux (FEFU Å)
1316.55	(4 - 2) P(19)	11.3
1320.22	(3 - 2) P(18)	5.4
1321.25	(1 - 3) R(12)	4.9
1357.51	(2 - 4) P(11)	1.49
1393.00	(4 - 6) P(8)	1.2
1393.79	(0 - 5) R(0)	35.3
1394.02	(0 - 5) R(1)	52.4
1395.26	(0 - 5) R(2)	2.4
1396.28	(0 - 5) P(1)	3.3

Table 3.5: RECX 1 Contaminating Emission

Wavelength (Å)	Flux (FEFU Å)	ID
1319.578	0.036	N I
1351.761	0.7	Cl I
1354.259	1.01	Fe XXI
1355.705	0.46	O I]
1355.805	0.54	O I]
1393.460	7.82	Si IV
1393.897	6.97	Si IV

Table 3.6: Fit Ranges

Object	Band	Lyα Blue (Å)	Lyα Red (Å)	CO Bandhead (Å)	CO Red (Å)
RECX 11	14 - 3	1213.0 - 1214.7	1216.6 - 1219.0	1315.5 - 1316.3	1317.4 - 1320.5
RECX 15	14 - 3	1213.0 - 1214.6	1216.5 - 1219.0	1315.5 - 1316.3	1317.8 - 1320.0
RECX 15	14 - 4	1213.0 - 1214.6	1216.5 - 1219.0	1352.5 - 1353.0	1354.8 - 1356.7
V4046 Sgr	14 - 3	1212.0 - 1215.0	1216.4 - 1219.0	1315.3 - 1315.9	1317.5 - 1320.0
V4046 Sgr	14 - 4	1212.0 - 1215.0	1216.4 - 1219.0	1352.0 - 1352.6	1354.5 - 1356.7
DM Tau	14 - 3	1210.0 - 1213.4	1218.0 - 1222.0	1315.6 - 1316.2	1317.4 - 1320.0
DM Tau	14 - 4	1210.0 - 1213.4	1218.0 - 1222.0	1352.2 - 1352.8	1354.5 - 1356.7
DE Tau	14 - 3	1211.5 - 1213.4	1217.5 - 1220.0	1315.3 - 1316.2	1317.8 - 1320.0
HD135344B	14 - 3	1212.0 - 1214.4	1216.8 - 1219.0	1315.0 - 1316.2	1317.5 - 1320.0
HN Tau	14 - 3	1211.0 - 1213.0	1218.0 - 1221.0	1315.3 - 1316.2	1317.8 - 1320.0
DR Tau	14 - 3	1211.0 - 1213.5	1218.0 - 1223.0	1315.4 - 1316.1	1318.5 - 1320.0
DK Tau	14 - 3	1211.0 - 1213.5	1217.3 - 1221.0	1315.4 - 1316.1	1317.5 - 1320.0
DF Tau	14 - 3	-	1217.3 - 1221.5	1315.7 - 1316.3	1317.0 - 1322.0
LkCa15	14 - 3	1210.0 - 1214.0	1217.3 - 1221.0	1315.4 - 1316.1	1317.5 - 1320.0
GM Aur	14 - 3	1210.0 - 1214.0	1217.5 - 1221.0	1315.4 - 1316.1	1317.5 - 1320.0

3.4   Results

I found strong CO (14 - 3) emission in 4 targets (V4046, RECX 15, DM Tau, and DF Tau), and was also able to fit the (14 - 4) band for three of those targets. DF Tau displayed excess O I emission in its (14 - 4) band, rendering a fit unreliable. RECX 11, DE Tau, and HD 135344B exhibited intermediate CO emission. HN Tau, DR Tau, DK Tau, LkCa 15, and GM Aur showed no significant emission above a continuum; for these targets, I determined upper limits on N_{CO} for a fixed T_{CO}. All column densities are well above the CO abundances expected from interstellar CO/H_2 ratios, assuming the H_2 column density found in TW Hya is representative (Herczeg et al., 2004). In over half of the positive detections, temperatures lie between 200 and 400 K, well below the $\sim$2500 K found for UV-excited H_2 (Herczeg et al., 2004). Interestingly, this is also lower than the rotational temperatures inferred from M-band CO spectra, $\sim$ 1000K (Najita et al., 2003).

Figures 3.8 through 3.17 show the model results for each of the CO detection targets. Parameter sets which resulted in good CO fits are plotted to demonstrate the range of possibilities. A "good" fit was determined, when possible, by χ^2_ν. Fits were excluded with χ^2_ν greater than 95.4 % from the χ^2 probability distribution. This typically removed $\sim$ 30% of the runs. The top panel shows the target's Lyα profile, along with the minimum and maximum incident radiation models that produced good CO model fits. The bottom panel shows the distribution of best fit T_{CO} vs. N_{CO}. Some of these T_{CO} vs. N_{CO} plots show clusters of crosses, such as in Figure 3.11, but such grouping merely results from similar parent Lyα profiles. From nearly identical starting parameters, the fitting routine is capable of finding multiple close minima in parameter space. Individual confidence intervals for each fit are typically smaller than the overall distribution of good fits. For this reason, I determine the listed parameter values from the minimum and maximum parameter values, with the average of the two chosen as the mean value. The CO model shown in the middle panel was chosen for being close to the average value of T_{CO} and N_{CO}, and its parent Lyα profile is shown in the top panel. This particular T_{CO}/N_{CO} combination is identified with a red box in the bottom panel of each figure.

For the models I present here, the gas is assumed to be closely distributed in the disk; thus, increasing N_{CO} can eventually saturate individual lines, limiting how much flux can be absorbed from Lyα. In order to ensure this assumption would not alter the fits, I modified the model so that any given N_{CO} was divided into smaller parcels before absorbing the Lyα photons. The resulting CO emission was then added to produce the model spectrum that was fit to the data. This is equivalent to the CO being spread out in a much wider distribution around the star so that more Lyα can be absorbed. Running the model fits under these assumptions did slightly change N_{CO} and T_{CO} by less than $\sim 20\%$. In addition, I tested the model fits for different CO continuum levels. Varying these continuua by their averaged error only changed the resulting N_{CO} and T_{CO} values by $\sim 15\%$ or less.

Table 3.7 lists the CO fit parameters for all targets. For the best-fit CO models, I list parameter values of the parent Lyα profiles in Tables 3.8 and 3.9. These are determined by taking the average and standard deviation of each parameter. To ensure that no larger or smaller values produced good fits, I tested wide parameter grids. These were different for each target, but generally are 20 - 30 % wider than the range of values in Tables 3.8 and 3.9. The resolution of the grids were limited by the amount of time it took to run the range of simulations; a run for a single set of parameters takes $\sim$20 minutes, and there are nine variable parameters for each run. I used two Lyα emission components for all cases where CO was significantly detected, except RECX 11, where the second component did not significantly improve the fit. In order to minimize grid-search computation time, I used a single Lyα emission component for the non-detections. Details for the fits of each target are discussed in the subsections below.

3.4.1   Strong detections

The V4046 Sgr spectrum has the highest S/N in the sample; thus it simultaneously demonstrates the strengths and limits of this approach. The high S/N made a good fit difficult with a simple combination of Gaussian emission and Voigt-profile absorption components, and thus I chose parameter values from the lowest cluster of χ^2_ν values. Even so, achieving a sufficient fit requires a
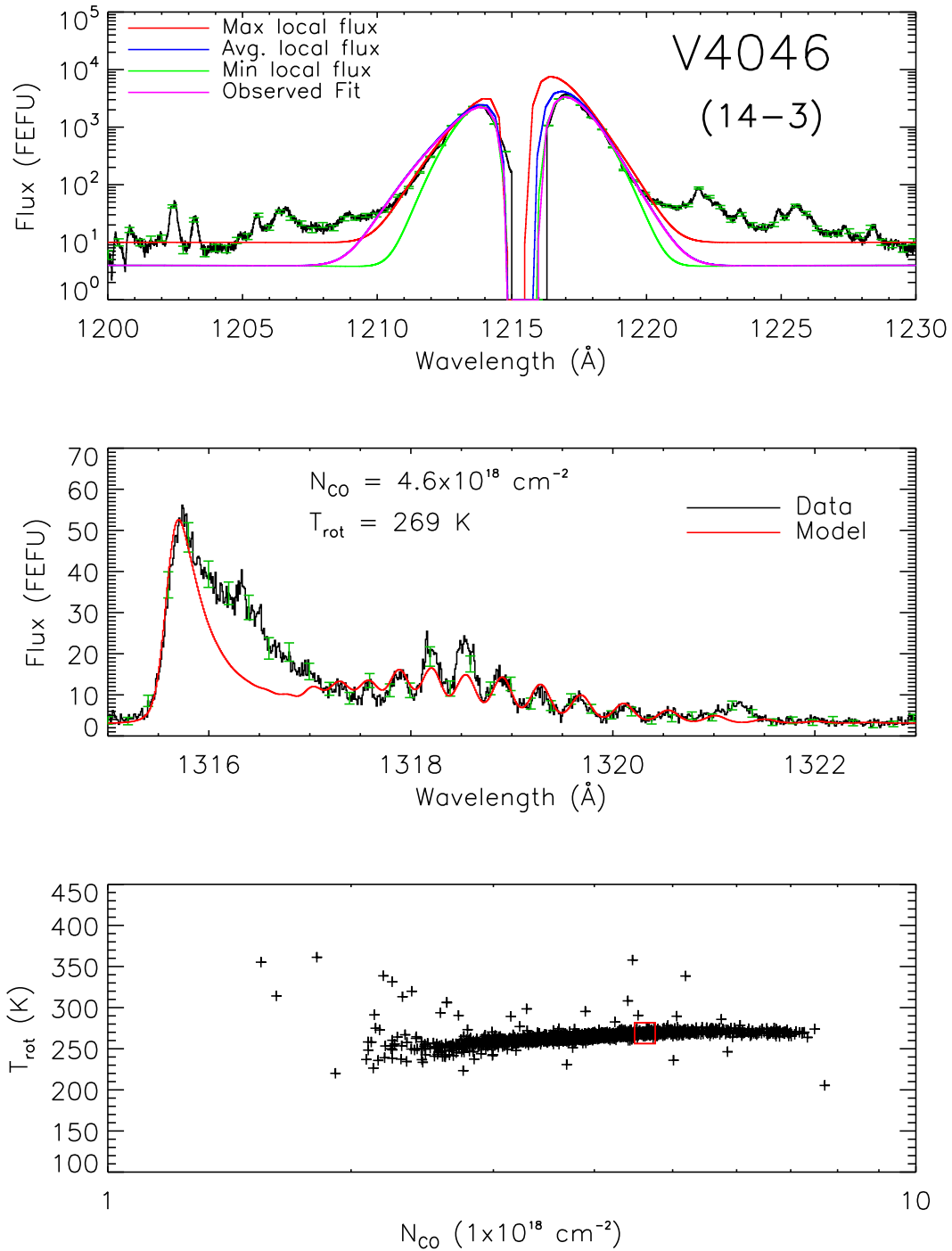
Figure 3.8: V4046 Sgr model results. Top: Lyα data overplotted with minimum, average, and maximum model Lyα profiles. Middle: CO (14 - 3) band with model from average T_{CO} and N_{CO}. Bottom: T_{CO} vs. N_{CO} for best fit models. The red square shows the values used in the middle plot.
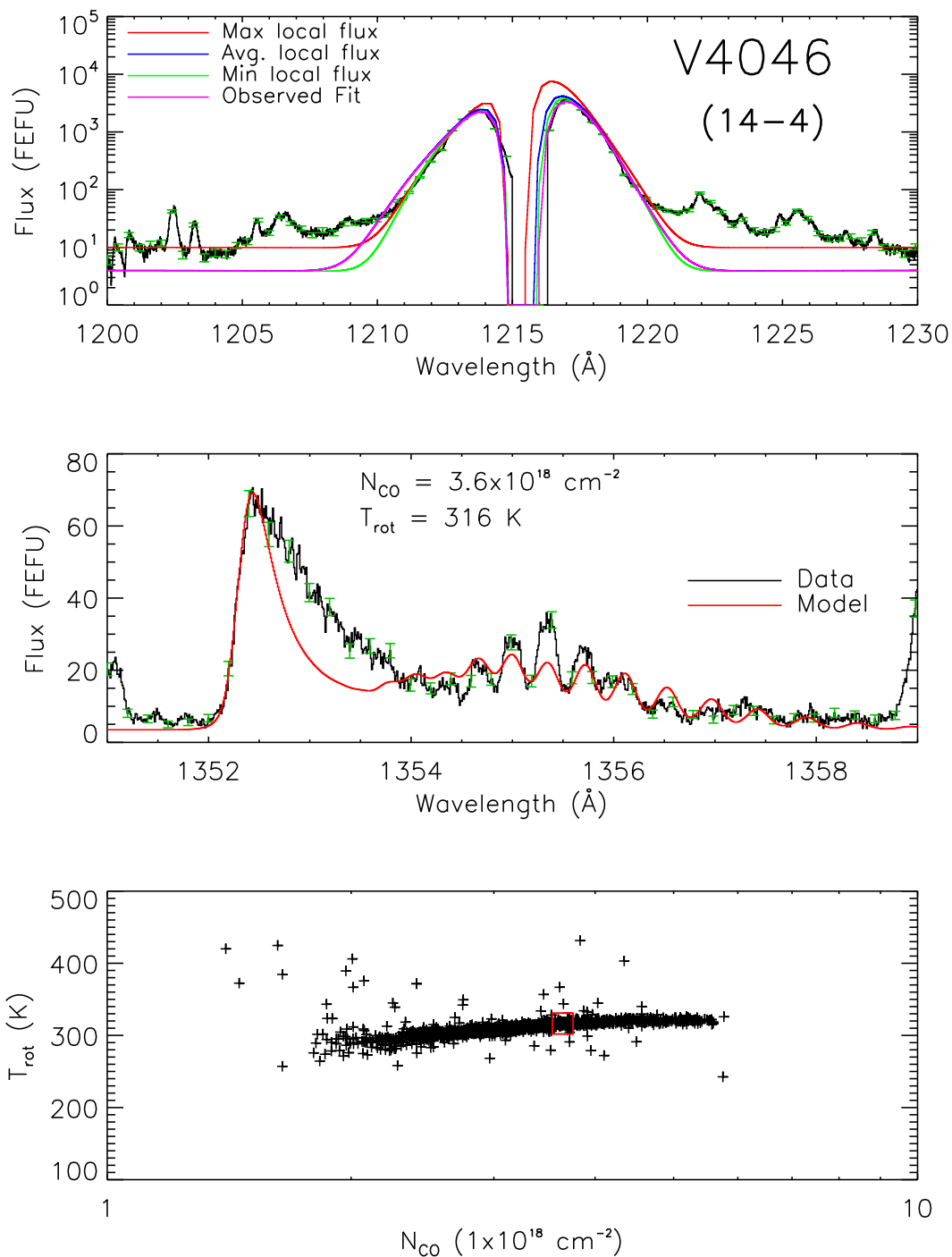
Figure 3.9: V4046 Sgr model results. Top: Lyα data overplotted with minimum, average, and maximum model Lyα profiles. Middle: CO (14 - 4) band with model from average T_{CO} and N_{CO}. Bottom: T_{CO} vs. N_{CO} for best fit models. The red square shows the values used in the middle plot.
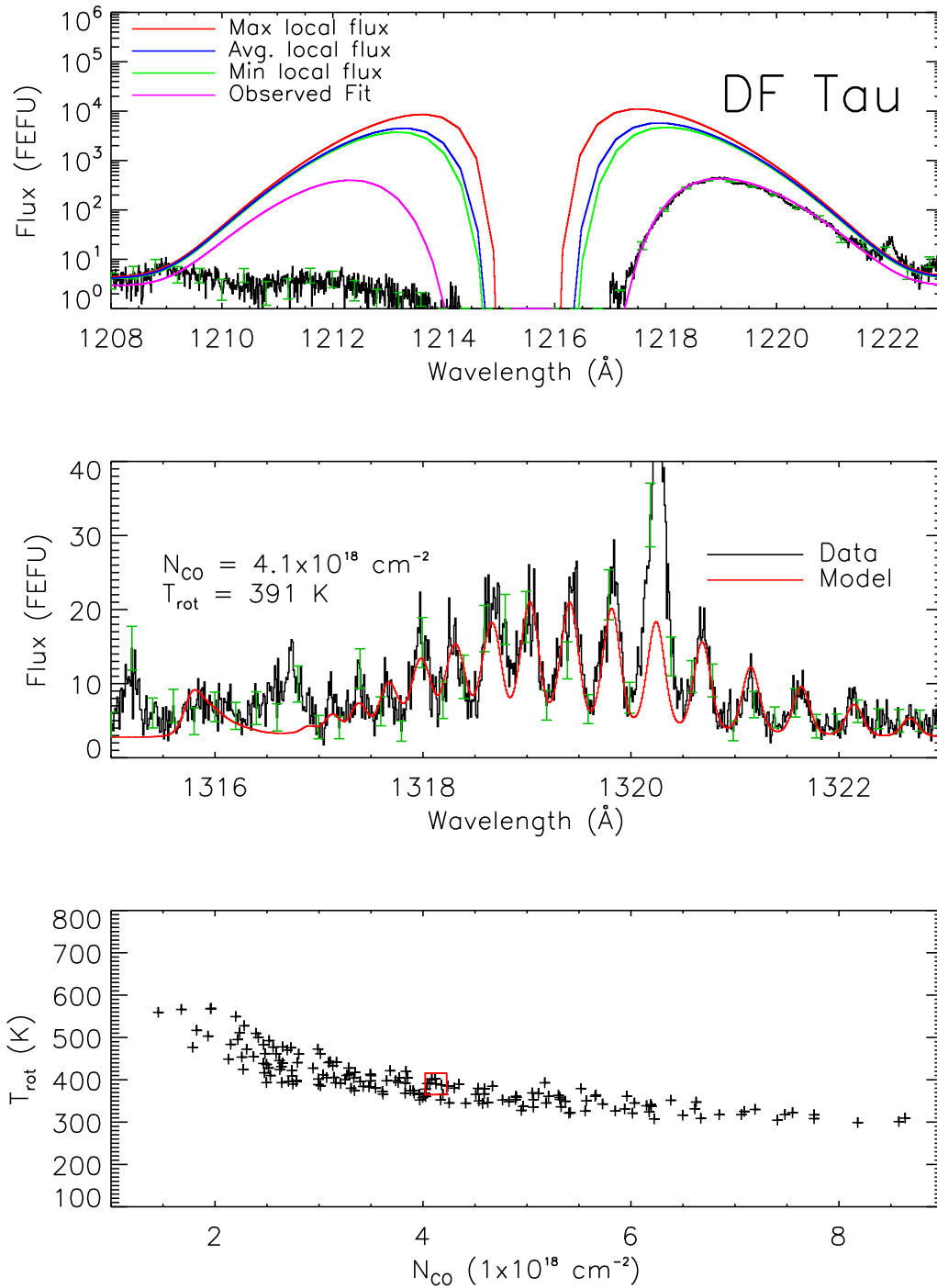
Figure 3.10: DF Tau model results. Top: Lyα data overplotted with minimum, average, and maximum model Lyα profiles. Middle: CO (14 - 3) band with model from average T_{CO} and N_{CO}. Bottom: T_{CO} vs. N_{CO} for best fit models. The red square shows the values used in the middle plot.
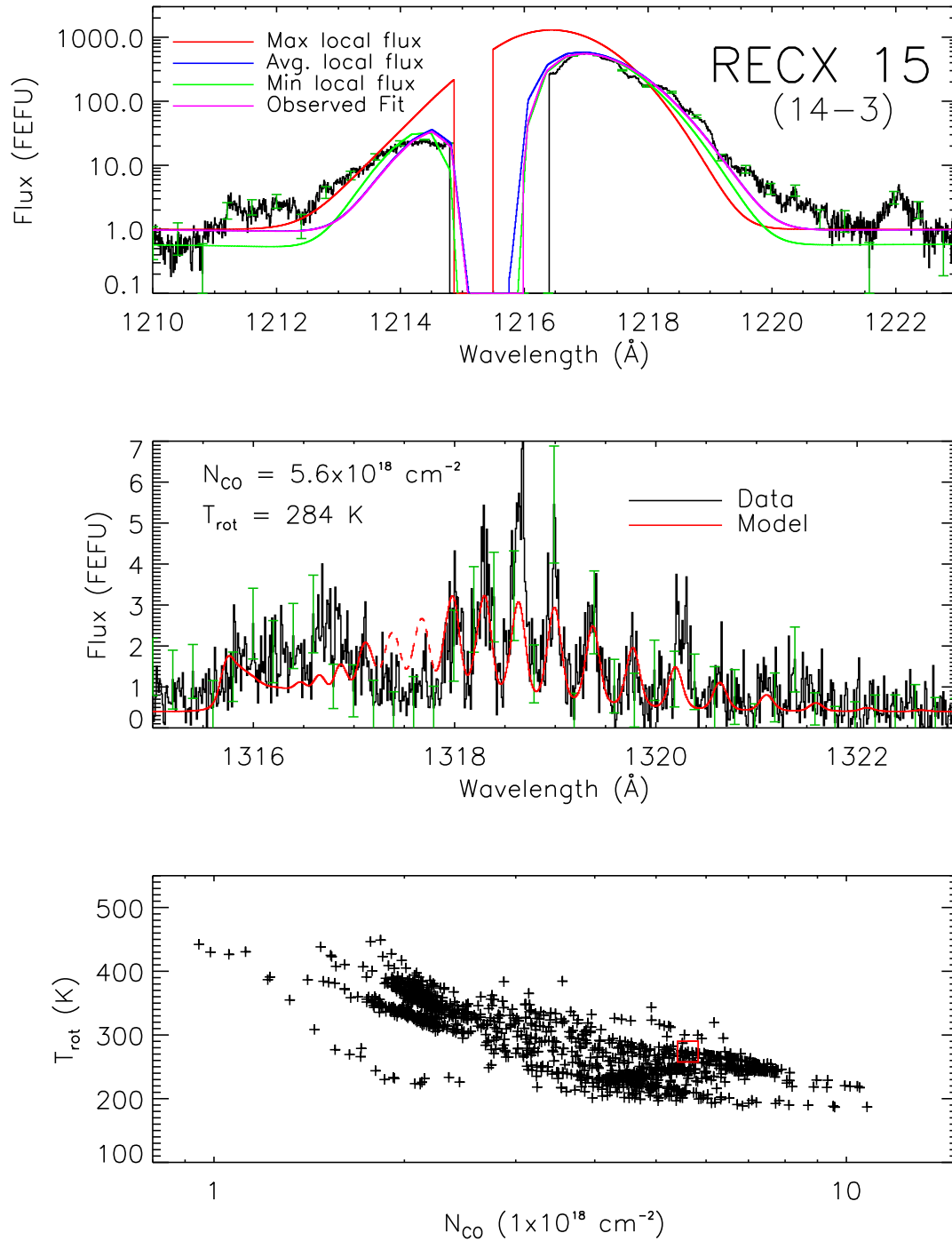
Figure 3.11: RECX 15 model results. Top: Lyα data overplotted with minimum, average, and maximum model Lyα profiles. Middle: CO (14 - 3) band with model from average T_{CO} and N_{CO}. Bottom: T_{CO} vs. N_{CO} for best fit models. The red square shows the values used in the middle plot.
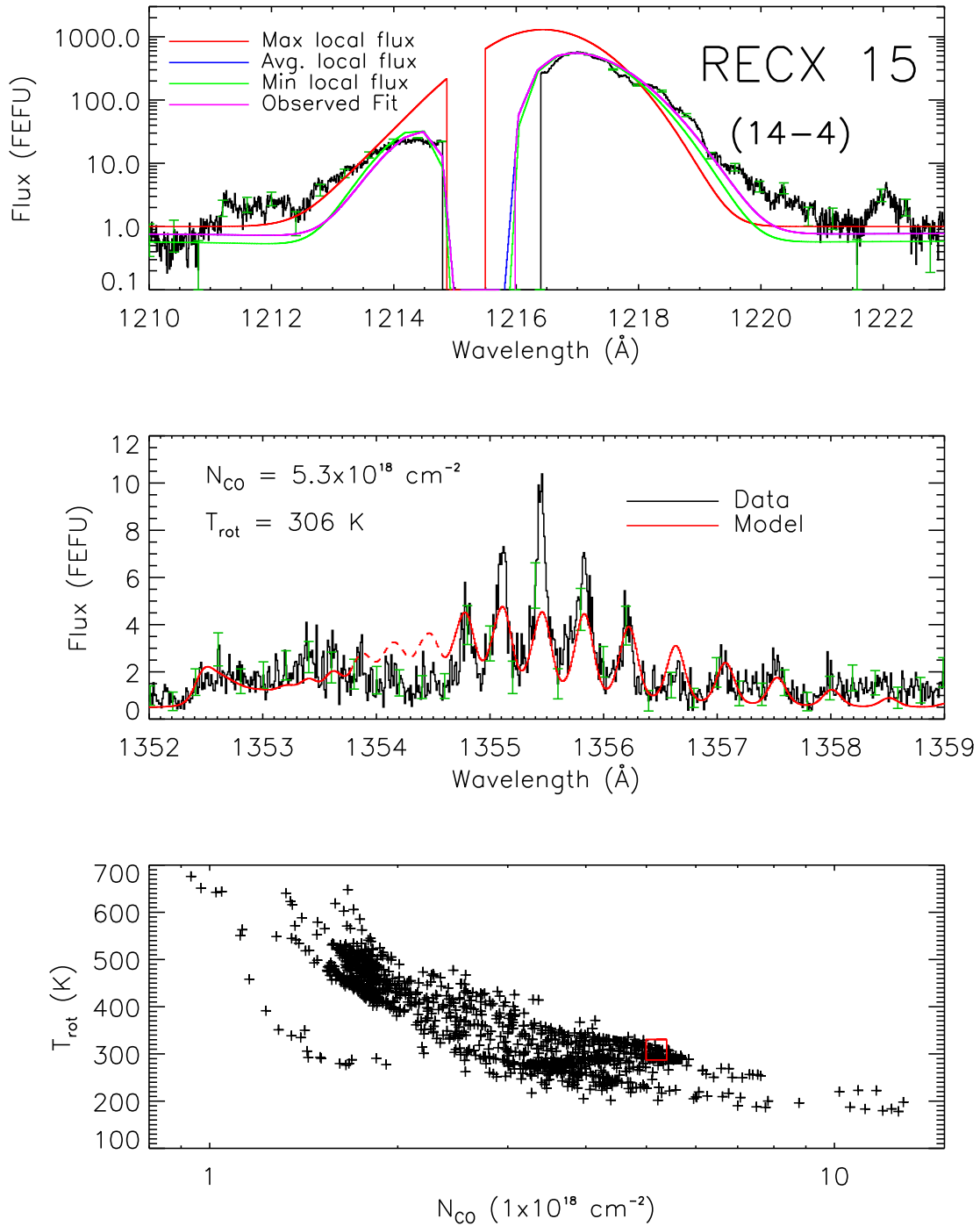
Figure 3.12: RECX 15 model results. Top: Lyα data overplotted with minimum, average, and maximum model Lyα profiles. Middle: CO (14 - 4) band with model from average T_{CO} and N_{CO}. Bottom: T_{CO} vs. N_{CO} for best fit models. The red square shows the values used in the middle plot.
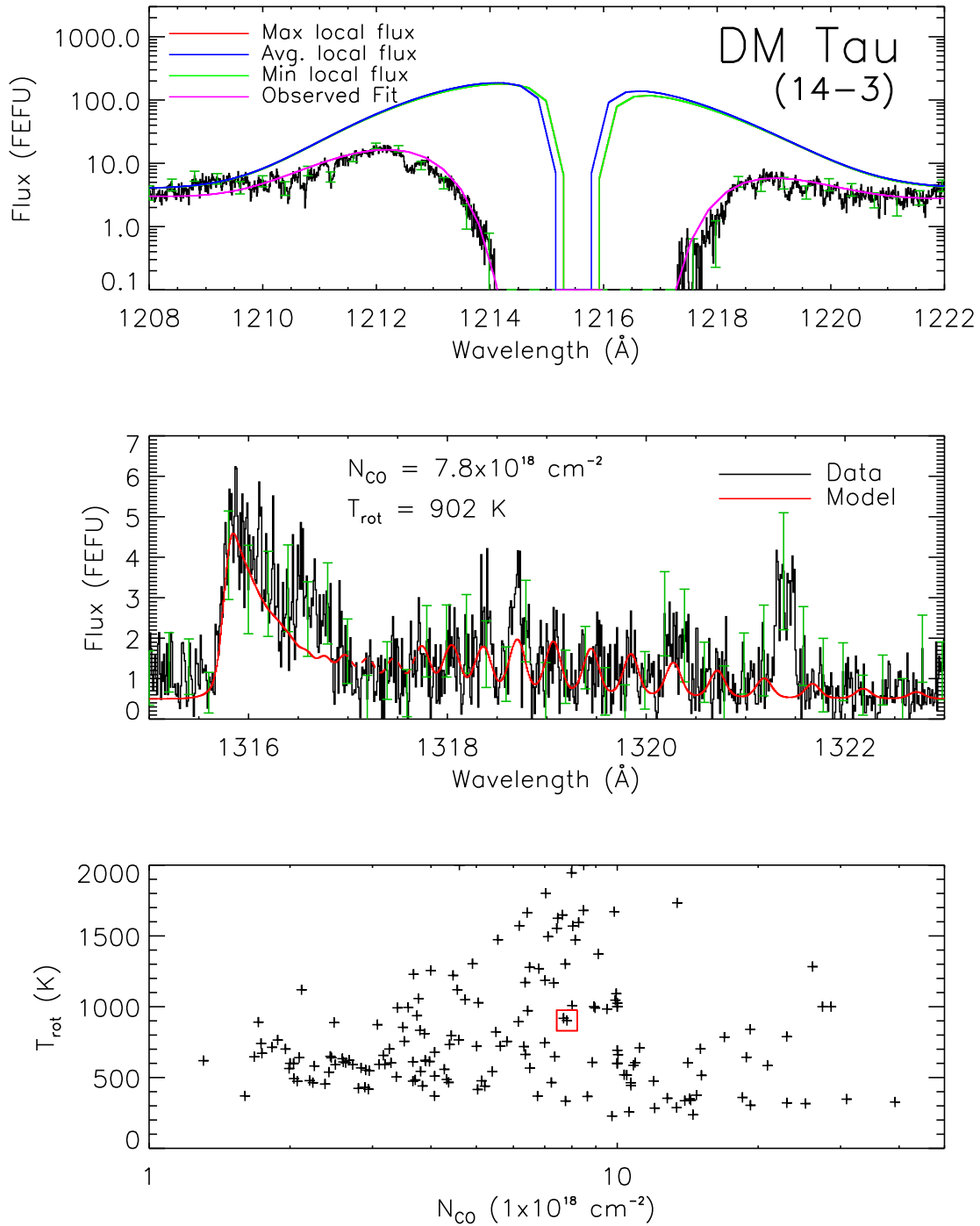
Figure 3.13: DM Tau model results. Top: Lyα data overplotted with minimum, average, and maximum model Lyα profiles. Middle: CO (14 - 3) band with model from average T_{CO} and N_{CO}. Bottom: T_{CO} vs. N_{CO} for best fit models. The red square shows the values used in the middle plot.
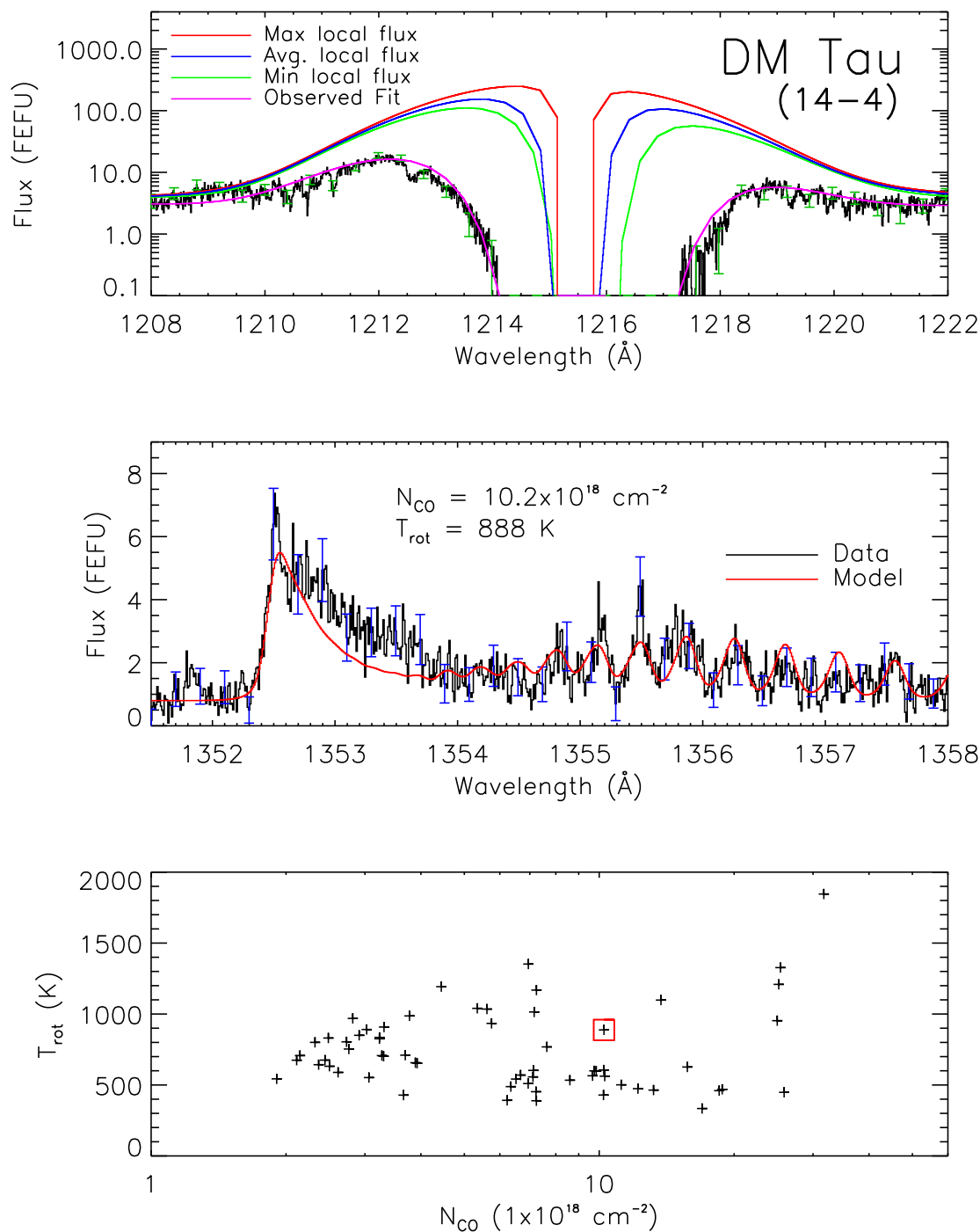
Figure 3.14: DM Tau model results. Top: Lyα data overplotted with minimum, average, and maximum model Lyα profiles. Middle: CO (14 - 4) band with model from average T_{CO} and N_{CO}. Bottom: T_{CO} vs. N_{CO} for best fit models. The red square shows the values used in the middle plot.
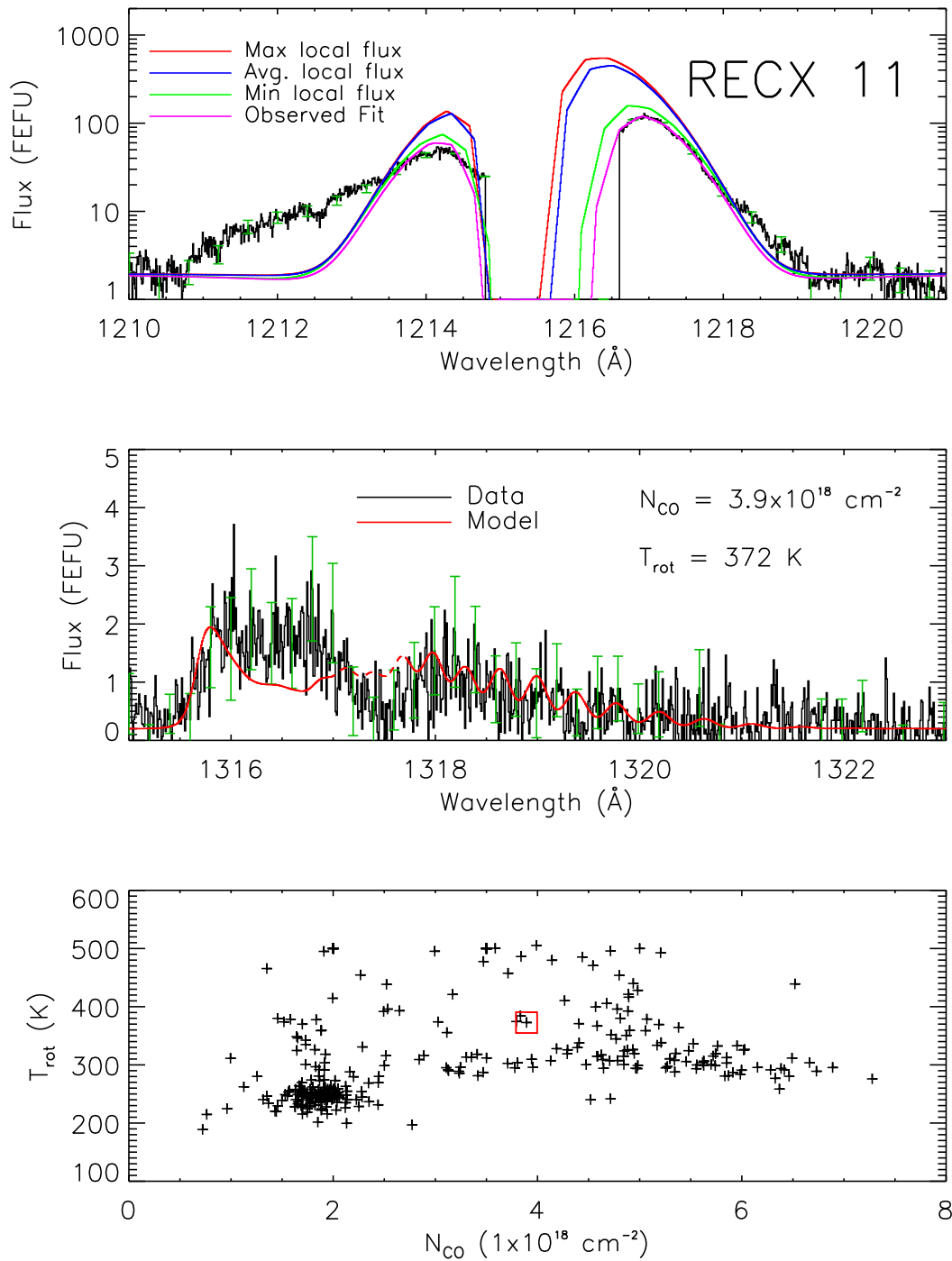
Figure 3.15: RECX 11 model results. Top: Lyα data overplotted with minimum, average, and maximum model Lyα profiles. Middle: CO (14 - 3) band with model from average T_{CO} and N_{CO}. Bottom: T_{CO} vs. N_{CO} for best fit models. The red square shows the values used in the middle plot.
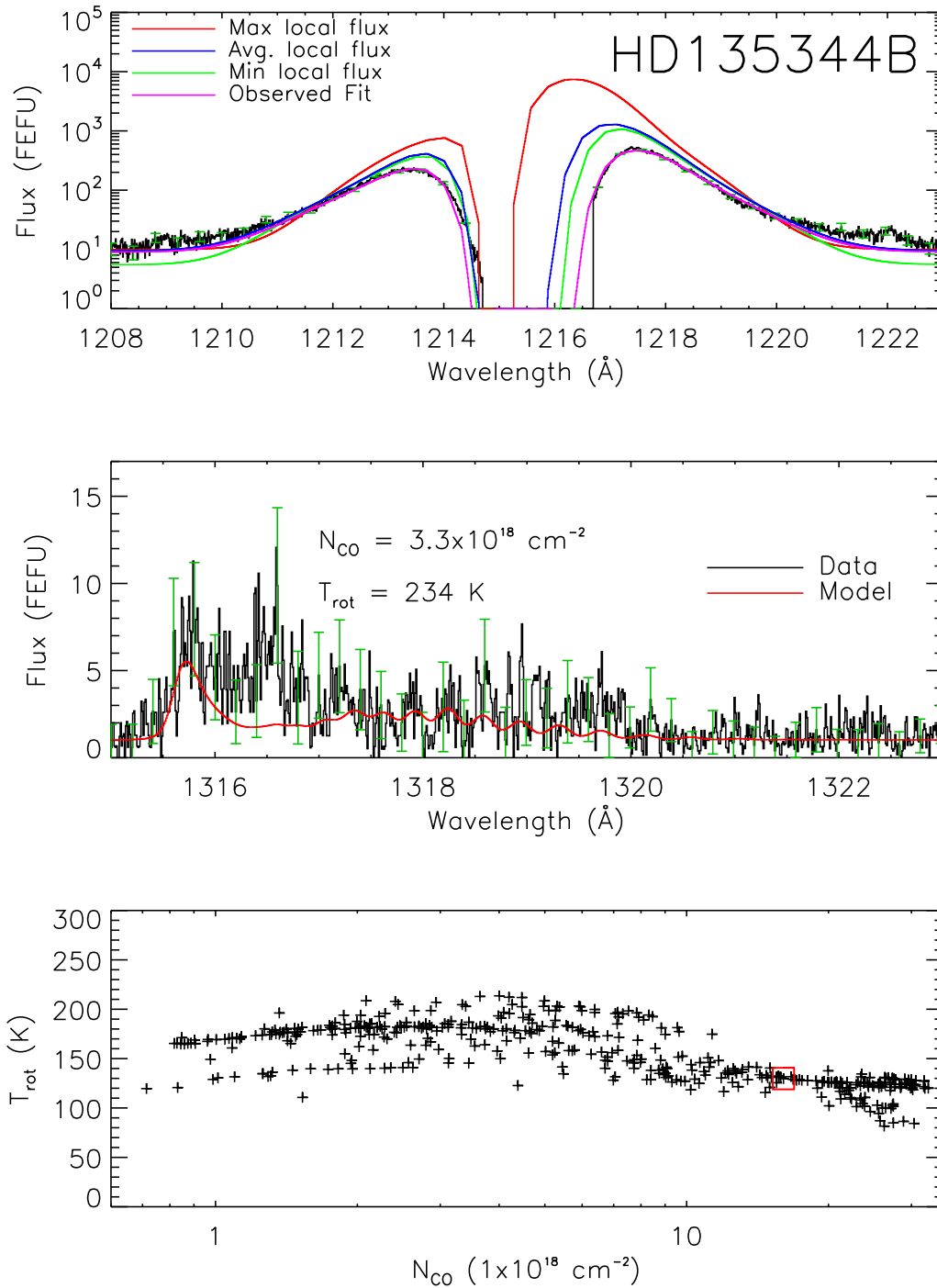
Figure 3.16: HD 135344B model results. Top: Lyα data overplotted with minimum, average, and maximum model Lyα profiles. Middle: CO (14 - 3) band with model from average T_{CO} and N_{CO}. Bottom: T_{CO} vs. N_{CO} for best fit models. The red square shows the values used in the middle plot.
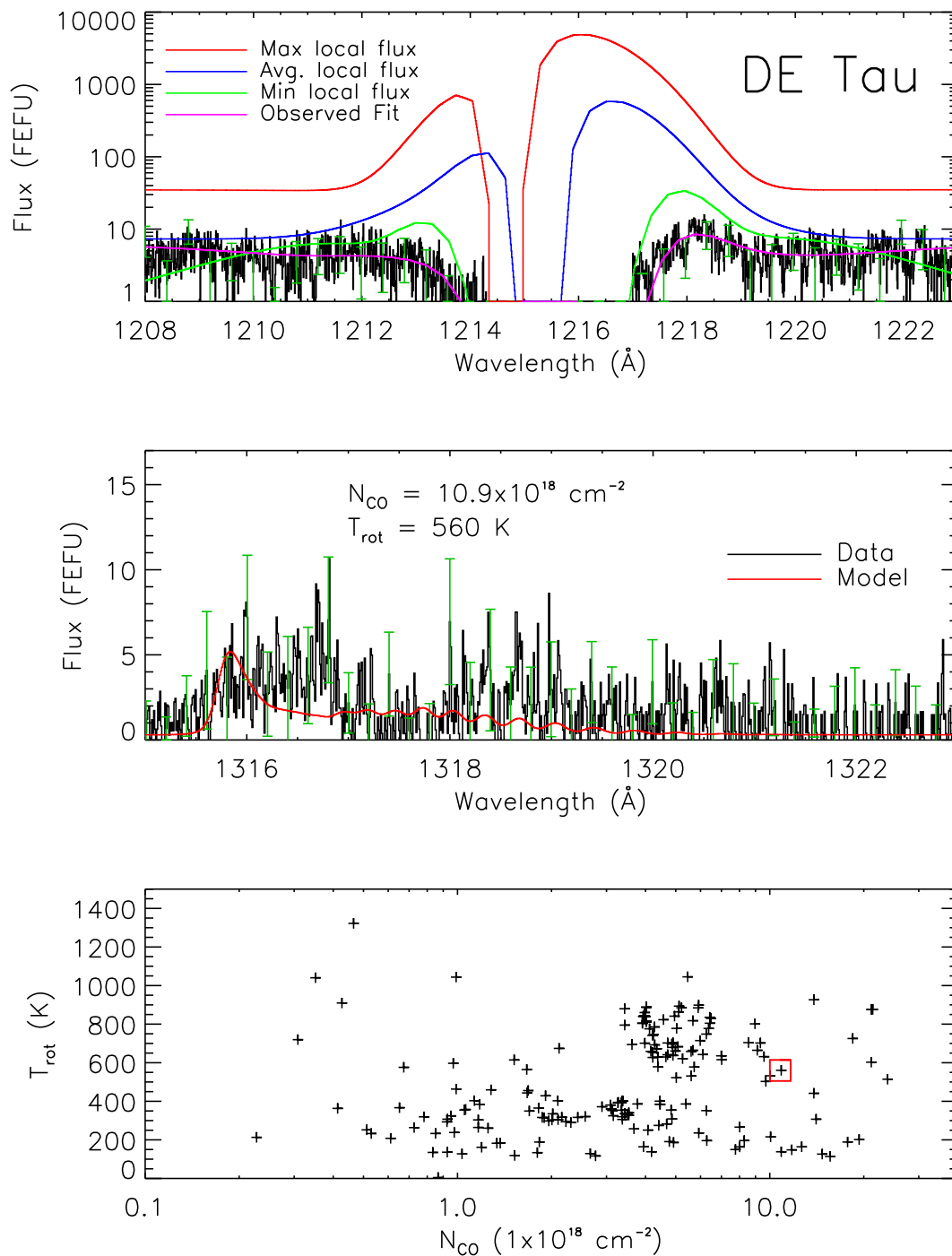
Figure 3.17: DE Tau model results. Top: Lyα data overplotted with minimum, average, and maximum model Lyα profiles. Middle: CO (14 - 3) band with model from average T_{CO} and N_{CO}. Bottom: T_{CO} vs. N_{CO} for best fit models. The red square shows the values used in the middle plot.

Table 3.7: Best-fit CO parameters

Object	Band	Continuum (FEFU)	b_{broad} (km s^{-1})	$\log(N_{CO})$ (cm^{-2})	$T_{CO}(K)$	$v_r(kms^{-1})$	χ^2_ν
V4046 Sgr	14 - 3	3.12	26.65 ± 0.78	18.54 ± 0.35	283.29 ± 77.95	-2.64	2.38 - 5.2
V4046 Sgr	14 - 4	3.50	30.33 ± 3.09	18.45 ± 0.31	336.99 ± 94.48	-6.40	5.18 - 7.55
DF Tau	14 - 3	2.77	21	18.55 ± 0.39	433.74 ± 134.89	27	< 1.08
RECX 15	14 - 3	0.40	15.97 ± 0.87	18.50 ± 0.53	317.76 ± 131.08	1.00	< 1.14
RECX 15	14 - 4	0.50	19.99 ± 1.00	18.54 ± 0.57	427.04 ± 248.93	1.00	1.7 - 2.04
DM Tau	14 - 3	0.50	18.53 ± 4.48	19.05 ± 0.93	1113.93 ± 886.07	35.00	< 1.18
DM Tau	14 - 4	0.80	16.72 ± 3.28	18.89 ± 0.61	1089.92 ± 755.76	26.17	< 1.14
RECX 11	14 - 3	0.20	53.39 ± 33.39	18.36 ± 0.50	347.16 ± 158.21	18.00	< 1.13
HD 135344B	14 - 3	1.02	40.63 ± 14.37	18.58 ± 0.93	147.56 ± 65.96	5.00	< 1.13
DE Tau	14 - 3	0.30	25.59 ± 19.69	18.35 ± 1.03	1002.25 ± 997.75	30.00	< 1.14
HN Tau	14 - 3	1.80	15.00 ± 0.00	19.62 ± 1.06	887.13 ± 396.91	30.00	0.51 - 0.66
DR Tau	14 - 3	15.20	20.00	< 18.65	350.00	30.00	< 1.17
DK Tau	14 - 3	4.60	20.00	< 17.85	350.00	30.00	< 1.14
LkCa 15	14 - 3	1.30	20.00	< 17.95	350.00	30.00	< 1.14
GM Aur	14 - 3	2.50	20.00	< 18.05	350.00	55.00	< 1.14

Table 3.8: Best-fit Lyα parameters

Object	Band	$I_1(0)$ (FEFU)	σ_1 (km s^{-1})	v_2 (km s^{-1})	$I_2(0)$ (FEFU)	σ_2 (km s^{-1})	$C_{Ly\alpha}$ (FEFU)
V4046 Sgr	14 - 3	10122 ± 3531	263 ± 40	-72 ± 35	5232 ± 2840	368 ± 31	7.00 ± 3.00
V4046 Sgr	14 - 4	9986 ± 3313	265 ± 40	-73 ± 36	5083 ± 2809	368 ± 32	7.00 ± 3.00
DF Tau	14 - 3	52084 ± 943	374 ± 0	-	-	-	4.50
RECX 15	14 - 3	16^{+29}_{-16}	265^{+292}_{-265}	208 ± 28	906 ± 146	224 ± 10	0.80 ± 0.20
RECX 15	14 - 4	29^{+38}_{-29}	263^{+290}_{-263}	207 ± 28	909 ± 149	224 ± 10	0.80 ± 0.20
DM Tau	14 - 3	18^{+34}_{-18}	339^{+365}_{-339}	-133 ± 20	270 ± 64	437 ± 14	4.00
DM Tau	14 - 4	52 ± 48	435 ± 268	-138 ± 11	257 ± 53	433 ± 13	4.00
RECX 11	14 - 3	1376 ± 1	197 ± 0	-	-	-	2.00
HD 135344B	14 - 3	2487 ± 1109	346 ± 52	118 ± 151	2293 ± 2168	158 ± 95	0.80 ± 0.20
DE Tau	14 - 3	4835 ± 4590	249 ± 59	-13 ± 78	1693^{+1914}_{-1693}	225 ± 152	1.13 ± 0.45
HN Tau	14 - 3	81 ± 48	429 ± 50	-	-	-	1.5 ± 0.5
DR Tau	14 - 3	2458 ± 452	407 ± 3	-	-	-	8.99 ± 1.01
DK Tau	14 - 3	2599 ± 497	281 ± 5	-	-	-	9.85 ± 4.65
LkCa 15	14 - 3	275 ± 54	335 ± 13	-	-	-	4.00 ± 2.00
GM Aur	14 - 3	910 ± 170	402 ± 20	-	-	-	1.92 ± 1.28

Table 3.9: Best-fit Lyα parameters (continued)

Object	Band	v_{out} (km s^{-1})	N_{out} ($10^{19} cm^{-2}$)	N_{ISM} ($10^{19} cm^{-2}$)	Model Lyα Flux (10^{-12} ergs s^{-1} cm^{-2})	χ^2_ν
V4046 Sgr	14 - 3	-96 ± 15	3.07 ± 0.81	1.18 ± 0.42	43.39 ± 7.55	104 - 136
V4046 Sgr	14 - 4	-95 ± 15	3.09 ± 0.80	1.15 ± 0.43	43.00 ± 7.18	104 - 136
DF Tau	14 - 3	-36 ± 7	14.00 ± 1.51	49.03 ± 1.45	197.64 ± 3.34	< 1.08
RECX 15	14 - 3	-85 ± 36	1.10 ± 1.02	0.94 ± 0.21	2.12 ± 0.43	2.2 - 20
RECX 15	14 - 4	-86 ± 36	1.10 ± 1.04	0.94 ± 0.20	2.12 ± 0.44	< 20
DM Tau	14 - 3	119 ± 178	1.46 ± 1.27	41.89 ± 2.11	1.20 ± 0.11	< 1.16
DM Tau	14 - 4	-50 ± 1	1.59 ± 1.26	40.92 ± 1.93	1.17 ± 0.13	< 1.16
RECX 11	14 - 3	-99 ± 4	1.97 ± 0.14	3.32 ± 0.14	2.76 ± 0.00	< 13
HD 135344B	14 - 3	-99 ± 26	5.61 ± 2.71	7.12 ± 1.68	18.54 ± 9.23	0.76 - 7.1
DE Tau	14 - 3	-103 ± 56	11.45 ± 7.70	34.80 ± 8.39	13.72 ± 7.93	< 1.11
HN Tau	14 - 3	-388 ± 108	22.49 ± 12.05	33.72 ± 8.87	3.58 ± 1.95	< 1.1
DR Tau	14 - 3	-1102 ± 537	42.23 ± 39.85	55.67 ± 3.09	10.17 ± 1.81	< 1.06
DK Tau	14 - 3	-619 ± 778	5.77 ± 2.89	32.98 ± 0.90	7.41 ± 1.36	< 1.08
LkCa 15	14 - 3	-306 ± 214	0.50 ± 0.72	36.90 ± 4.24	0.94 ± 0.19	< 1.10
GM Aur	14 - 3	-156 ± 98	5.91 ± 3.21	29.89 ± 3.75	3.8 ± 0.08	< 1.15

second blueshifted Lyα component. A broad emission feature appears from 1205 - 1230 Å, which sits upon the continuum of the surrounding region. As shown in Figure 3.2, CO emission due to Lyα photons greater than 1220 Å is not seen; therefore I ignore this region of the Lyα profile.

The high S/N in the CO profiles makes it difficult for the simple Lyα profile to produce an exciting radiation spectrum which accommodates all features in the CO profile. The lack of knowledge about the core of the Lyα profile is chiefly responsible for discrepancies between the model flux and that of the observed spectrum. Flux in the 1316 - 1317 Å region is under-predicted; this is likely due to a more complicated absorbing outflow velocity distribution than I can reasonably model at present. Future work will include more complicated velocity profiles. Because in some cases I was unable to adequately reconstruct the Lyα red wing, some of the high-J CO lines between 1317.5 and 1319 Å are over or under-predicted.

In DF Tau there is far more red wing emission than the other targets, but this is not surprising given its high accretion rate (the accreting material causes predominantly redshifted emission). I use a spline interpolation of the red Lyα wing, due to weak H_2 absorption features on its red edge. Its blue wing is almost non-existent, so I used only a single Lyα emission component. The minor bandhead emission limits v_r; too high a velocity wipes out any Lyα photons to excite those states. The strong line at 1320.3 Å is underpredicted is due to H_2. I traced this line to its $B - X$ (3-0) pumping transition coincident with Lyα. Fits to H_2 lines at other wavelengths (1268.84 Å (3-1) P(18) and 1278.11 Å(3-2) R(16)) predict a flux which matches the excess flux at 1320.3, when appropriate branching ratios are applied. This further validates these methods and models, as any more or less H_2 in that line would contradict the best-fit CO profiles.

A spline interpolation was also necessary for the blue Lyα wing in RECX 15. Due to the complexity of this Lyα profile, it was challenging to fit the RECX 15 CO profiles. As with V4046, the minimum χ^2_ν values were still relatively high ($\sim 2 - 20$), and the lowest cluster of χ^2_νs was considered the best fits. The high-J line widths appear to be unresolved, which with the target's high inclination ($i \sim 60°$) would imply that the emitting CO lies at least several AU from the star. If I assume that rotational velocity dominates b_{broad}, then

$$r \sim \frac{GM_*}{b_{broad}^2} \qquad (3.7)$$

For b_{broad} <20 km s^{-1} and M_*=0.3 $M_\odot$, this would place the gas at > 2.7 AU.

For DM Tau, a spline-interpolated profile was used to fit both wings of the Lyα profile. The velocity for the outflow absorber mostly found positive values, due to the lower Lyα red wing. Physically, this could correspond to infalling material that absorbs the Lyα radiation. In both the (14 - 3) and (14 - 4) bands of DM Tau, the values of T_{CO}, N_{CO}, and b_{broad} agree within error bars. The required v_r to fit each band differs by ∼10 km s^{-1}, but this is within the resolution of COS. It could therefore be accounted for by errors in the wavelengths solution or the coaddition process.

3.4.2   Intermediate Detections

I distinguish three targets as "intermediate" detections. For these there is little emission above a continuum, and the S/N is low, but features are still evident to the eye. Bandhead and/or high-J line emission is seen in RECX 11, HD 135344B, and DE Tau, and arguably so in HN Tau. However, in these targets the S/N is low enough to make it difficult to constrain parameters as well as in the "strong" detection targets. I used the same methods as for the strong detection targets, although RECX 11 and HN Tau did not require a second Lyα emission component. In RECX 11 the blue wing is strongly blueshifted, but this emission lay far from the 1214.2 Å CO (14 - 0) bandhead, so I chose to ignore it in the fitting region. The S/N in the Lyα profile is high enough to limit the quality of fit to $\chi_\nu^2 > 9.3$. The CO high-J lines are not resolved, although whether this is physical or merely due to the lower S/N in the band is unknown. As a result, b_{broad} has a wide range of values. Similar features are seen with HD 135344B, but the temperature is more well-constrained to lower temperatures. The Lyα profile of DE Tau is highly absorbed, yet the (14 - 3) high-J lines are unmistakeable even amongst the noise.

3.4.3   Non-detections

For all CO non-detection targets, the low S/N did not merit an extra Lyα emission component. I demonstrate the limits of this method for targets with little Lyα and CO emission by modeling HN Tau in the same manner as the strong and intermediate detections. Figure 3.18 shows the results. Due to the low S/N in the Lyα profile, outflow values as high as -1200 km s^{-1} or more produce good fits. The resulting large N_{CO} values therefore cannot be trusted, and it is only possible to calculate upper limits on the non-detection targets. Therefore, instead of using the previous CO modeling method, I fit Lyα profiles and used them to generate CO model spectra for varying N_{CO} and other fixed values. I used $T_{CO} = 350$ K, more representative of the temperatures from the higher S/N targets. Similar logic drove us to choose $b_{broad} = 20$ km s^{-1}. As no strong bandhead or high-J lines were available to determine v_r, I set this to the stellar velocity.

Figure 3.19 shows histograms for the number of fits for a given N_{CO} that resulted in a χ^2_ν less than the 95.4% value for its χ^2 probability distribution. These histograms therefore provide a qualitative, if not thoroughly quantitative, representation of how much CO is "too much" to match the observed data. The higher column densities correspond to weaker Lyα profiles, where more CO is necessary to push the resulting (14 - 3) emission noticeably above the continuum. The highest N_{CO} values result from assuming that the Lyα emission seen is responsible for exciting the CO. However these targets have moderate extinction ($A_V = 0.6$ - 1.4), and thus some amount of N$_{ISM}$ must be present, resulting in a higher incident radiation field for the CO.

To limit N_{ISM} I use the A_V and N_{ISM} of DF Tau to form a rough extinction relation. Assuming that this relation would be similar for other targets in the Taurus-Auriga star forming region, I exclude N_{ISM} values less than half of this line at a given A_V. The necessity for this constraint demonstrates the weakness of the method in the case of highly extincted Lyα profiles. Well-defined fits in parameter space require both a strong Lyα profile and CO band emission. With almost no information about the Lyα profile, it is difficult to place limits on either the Lyα or CO emission. Even in the case of GM Aur and its well-defined Lyα profile, the negligable CO flux
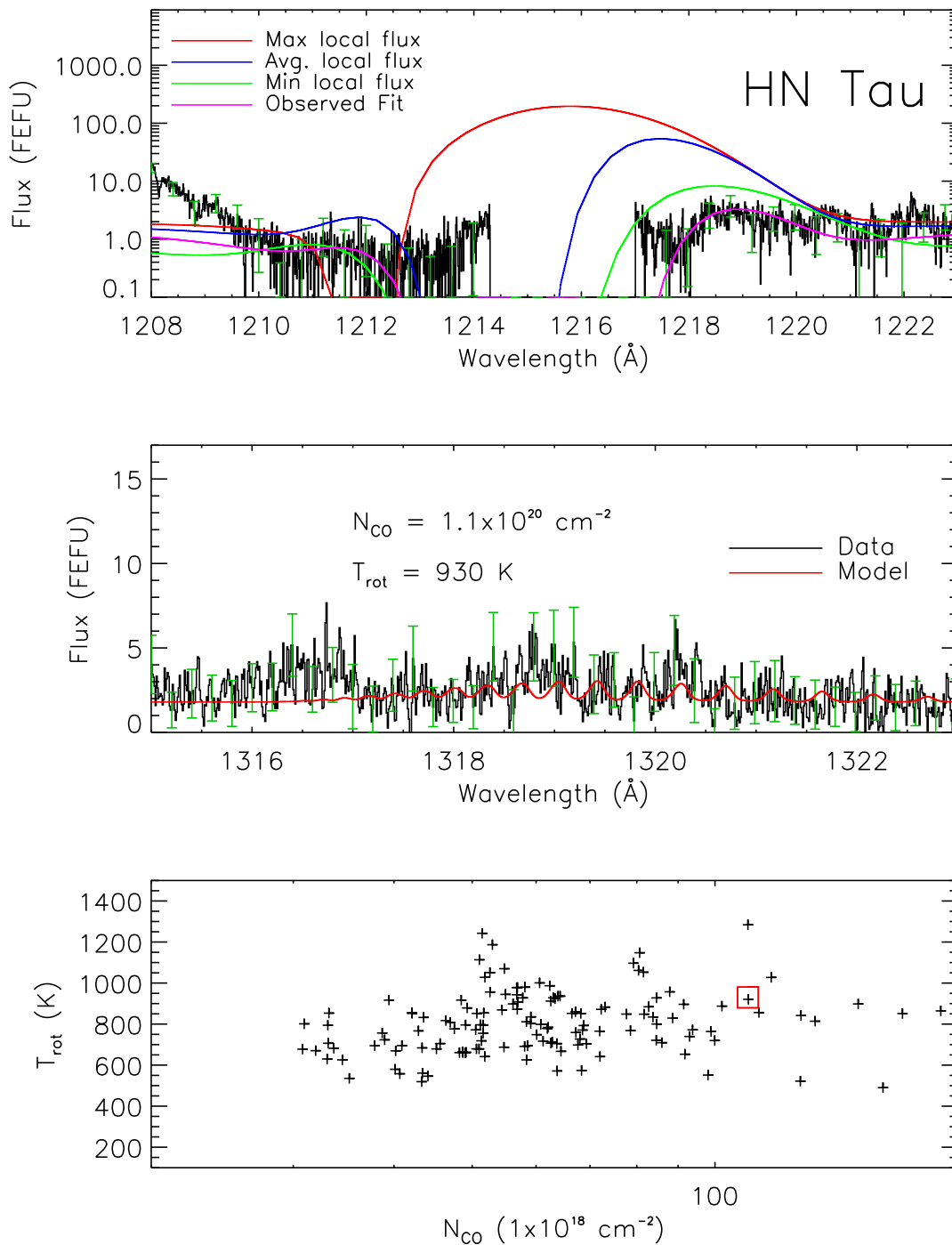
Figure 3.18: HN Tau model results. Top: Lyα data overplotted with minimum, average, and maximum model Lyα profiles. Middle: CO (14 - 3) band with model from average T_{CO} and N_{CO}. Bottom: T_{CO} vs. N_{CO} for best fit models.
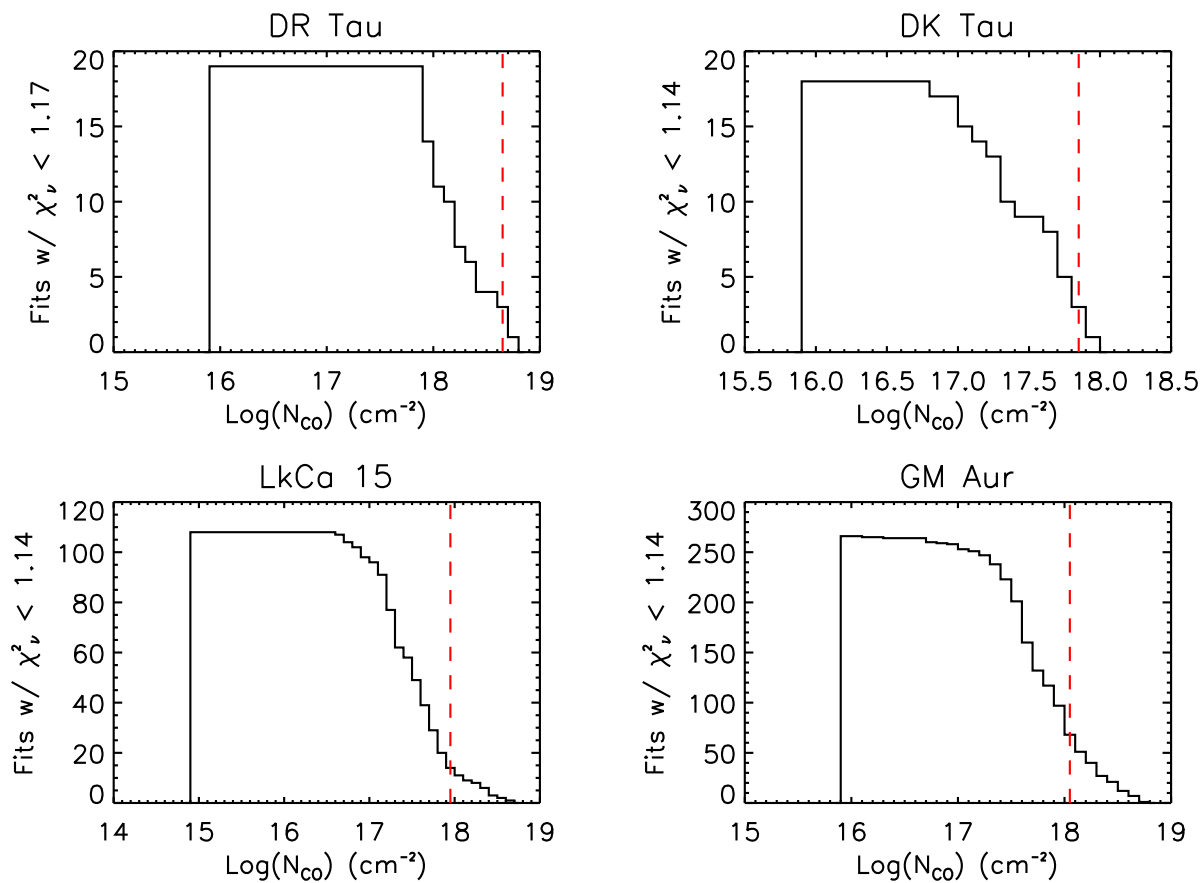
Figure 3.19: Histograms for upper-limit N_{CO} values in "non-detection" targets. These numbers come from models with χ^2_ν less than 95.4% from the χ^2 probability distribution.

makes it difficult to constrain Lyα parameters.

3.4.4   Band Fluxes

In addition to calculating CO temperature and column density, I integrate the flux in each of the bands. These fluxes provide additional information for correlations with target parameters from the literature. As described in §3.3.2, I avoid the red sides of the 1352 and 1390 Å bands due to strong O I] and Si IV contamination. Figures 3.20 through 3.23 show the bands, as well as the details for flux summation. Contaminating emission lines are noted at the top of each plot, with vertical red dashed lines continuing downward for identification in other targets. The horizontal black/blue/red line is placed at the continuum level, which I determine by averaging continuum flux in the surrounding area. The horizontal blue and red lines identify the low and high J state emission regions; for example, in the blue region of the (14 - 3) band, the Js for the R branch range from 1 to 15 (1315.68 - 1317.5 Å). The dashed orange lines above and below mark the 1-σ error bars for that continuum average. The regions around the CO bands contain potential absorption and emission from other atoms/molecules, and these errors account for that difference. The integrated flux values for the 1315, 1352, and 1390 Å bands are listed in Tables 3.4.4 - 3.4.4. The error bars are defined by the difference in flux between that calculated from the average and upper/lower continua.

Measuring fluxes in the 1713 Å band is more challenging than the other bands. Between the decreased sensitivity of COS at longer wavelengths and the presence of unknown absorption features, continuum levels are more difficult to determine. Still, it is possible to quantify flux values with larger error bars. Of particular note is the fact that these fluxes are larger than what would be expected purely from branching ratios, when compared with fluxes from the other Lyα-pumped bands. Figure 3.24 shows this graphically, with the dashed line representing the expected 1713 Å integrated flux for a given 1315 Å integrated flux. The amount of flux in excess of this amount is listed in Table 3.4.4. Thus, some process other than Lyα photo-excitation must be responsible for pumping the CO molecules. It is likely the result of C IV photo-excitation, which is capable
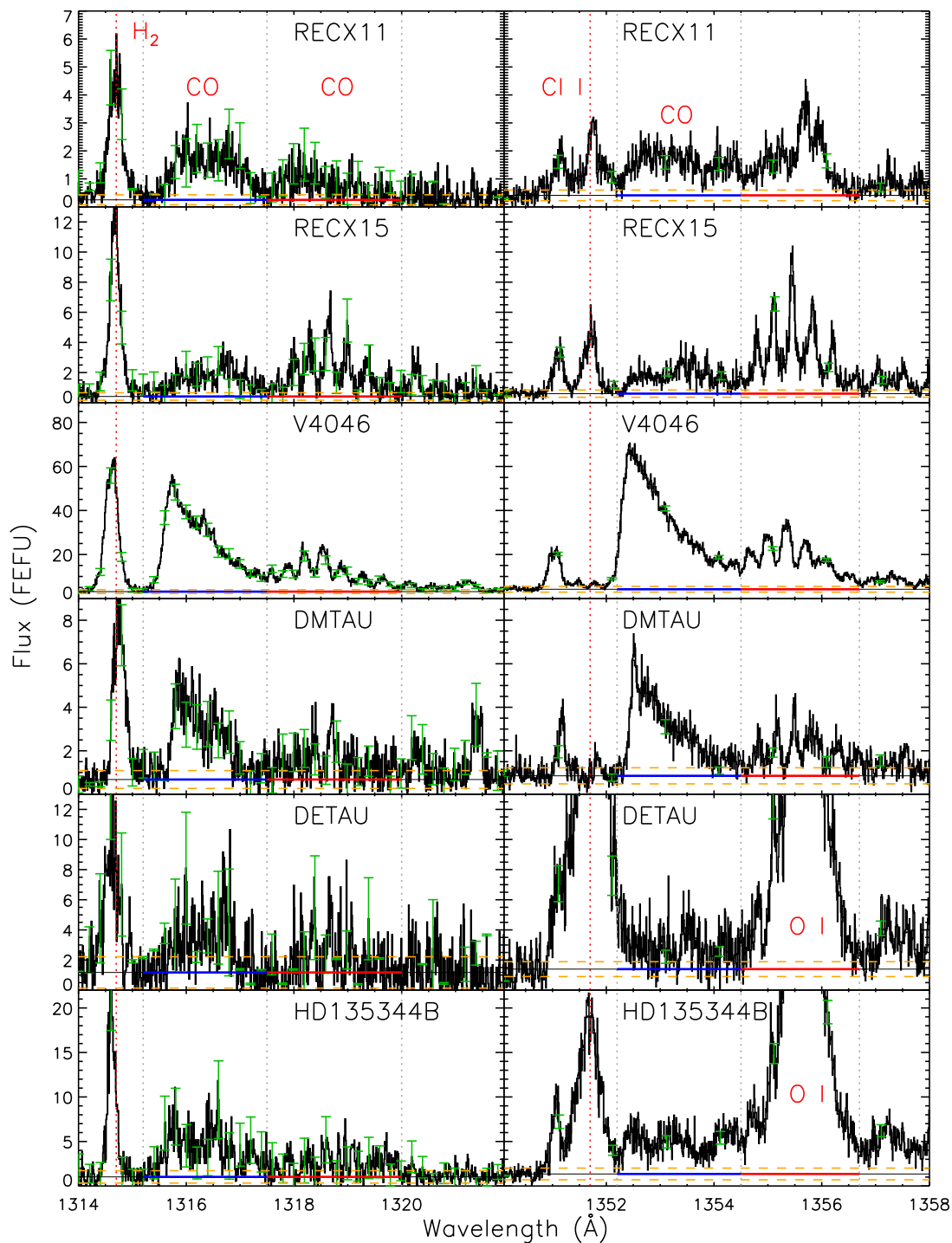
Figure 3.20: (v'=14,v"=3, left column) and (v'=14,v"=4, right column) transitions for targets as identified. The horizontal lines show continuum levels, with dashed orange lines indicating the upper and lower limits for summation. The solid blue and red lines mark the wavelength range for the blue and red bands as described in the text; vertical gray lines bound these regions. Vertical dashed red lines mark contaminating lines, labeled in the top of the plot. Each row shares the same flux axis.
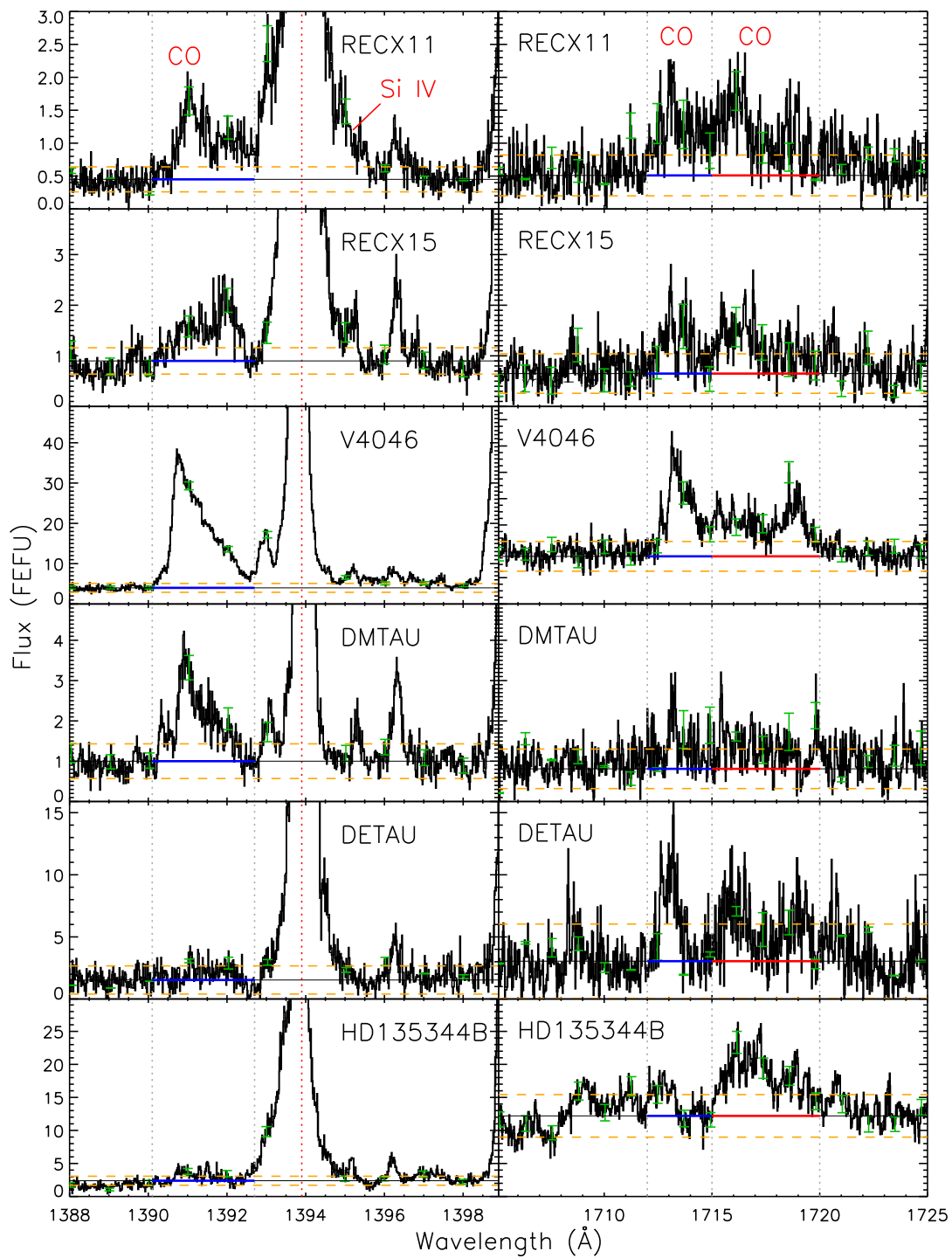
Figure 3.21: (v'=14,v"=5, left column) and (v'=14,v"=12, right column) transitions for targets from Figure 3.20, with same demarcations as Figure 3.20.
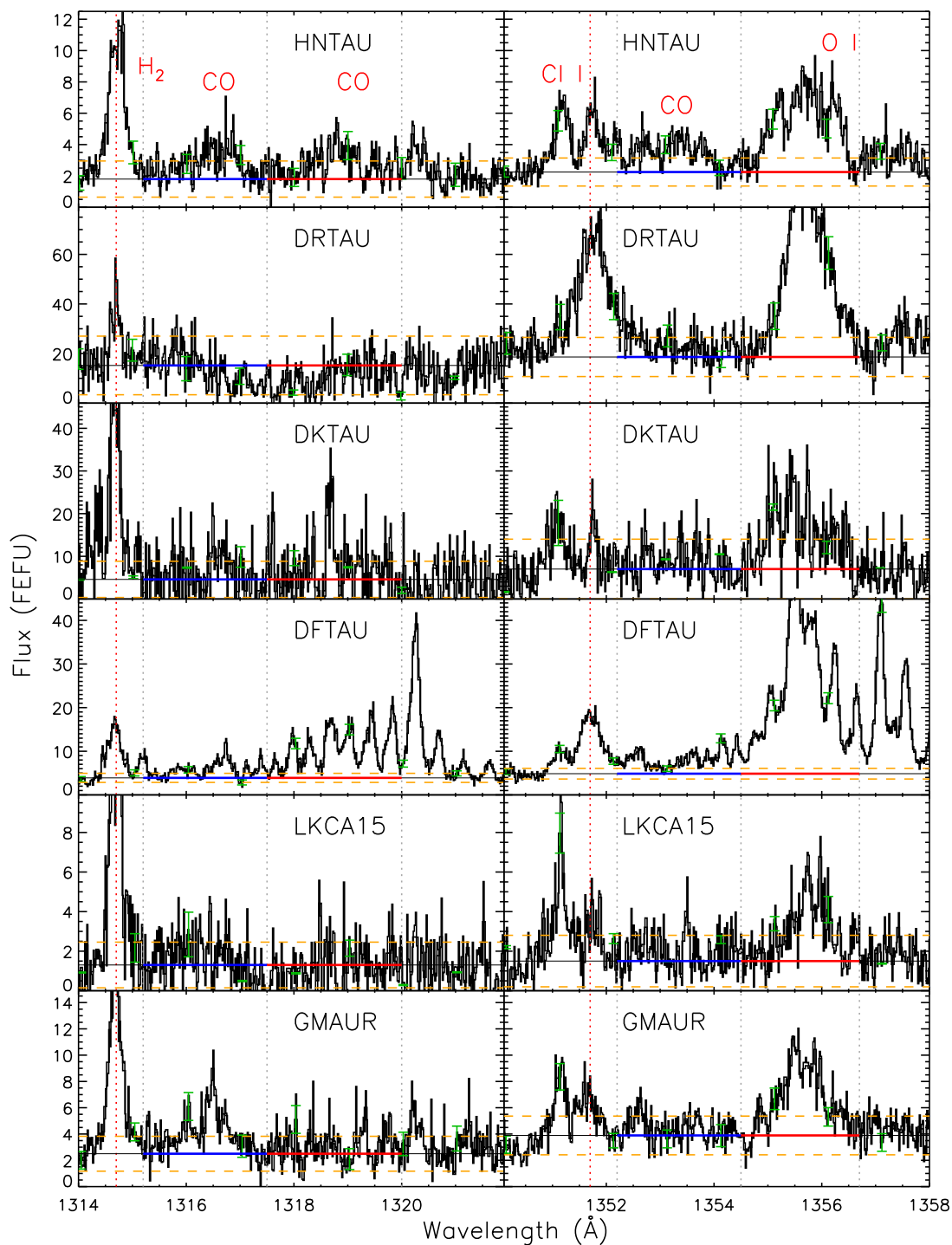
Figure 3.22: (v'=14,v"=3, left column) and (v'=14,v"=4, right column) transitions for second set of targets, with same demarcations as Figure 3.20.
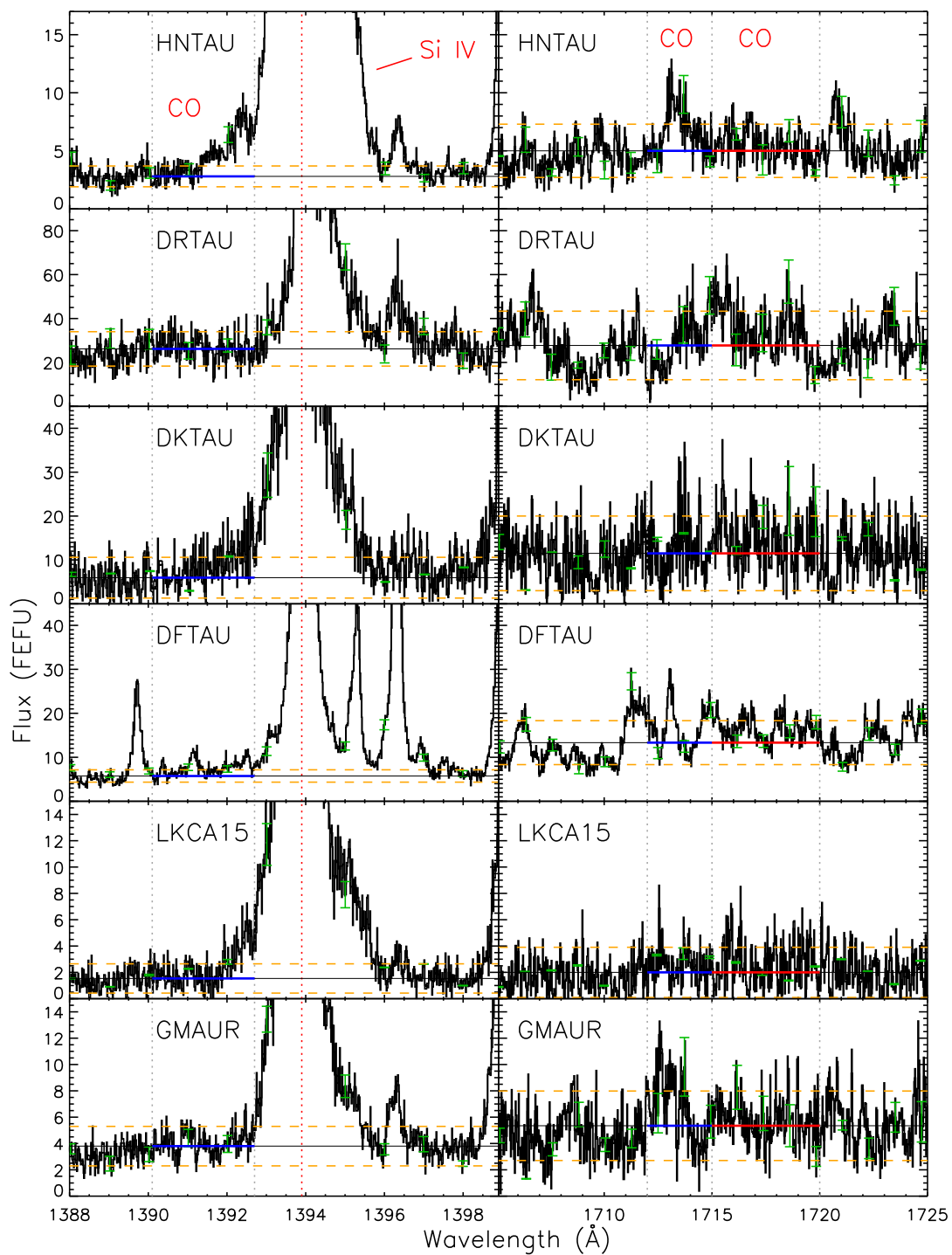
Figure 3.23: (v'=14,v"=5, left column) and (v'=14,v"=12, right column) transitions for second set of targets, with same demarcations as Figure 3.20.

Table 3.10: 1315 Å Band Summed Fluxes

Target	Continuum (FEFU)	Blue Flux (FEFU Å)	Red Flux (FEFU Å)
RECX11	0.25 ± 0.18	$2.36^{+0.41}_{-0.41}$	$1.21^{+0.45}_{-0.45}$
RECX15	0.41 ± 0.25	$2.41^{+0.57}_{-0.57}$	$3.68^{+0.63}_{-0.63}$
V4046	3.12 ± 0.86	$47.77^{+1.97}_{-1.97}$	$20.78^{+2.15}_{-2.15}$
DMTAU	0.68 ± 0.41	$3.63^{+0.94}_{-0.94}$	$1.85^{+1.03}_{-1.03}$
DETAU	1.18 ± 1.04	$3.61^{+2.39}_{-2.39}$	$1.71^{+2.61}_{-1.71}$
HD135344B	1.02 ± 0.70	$6.99^{+1.60}_{-1.60}$	$3.84^{+1.74}_{-1.74}$
HNTAU	1.80 ± 1.15	$2.12^{+2.65}_{-2.12}$	$2.33^{+2.88}_{-2.33}$
DRTAU	15.20 ± 11.82	$0.00^{+27.10}_{-0.00}$	$0.00^{+29.58}_{-0.00}$
DKTAU	4.60 ± 4.24	$3.52^{+9.77}_{-3.52}$	$7.02^{+10.58}_{-7.02}$
DFTAU	3.90 ± 1.04	$4.31^{+2.40}_{-2.40}$	$16.96^{+2.61}_{-2.61}$
LKCA15	1.30 ± 1.15	$0.65^{+2.66}_{-0.65}$	$0.00^{+2.88}_{-0.00}$
GMAUR	2.50 ± 1.33	$3.45^{+3.06}_{-3.06}$	$1.41^{+3.32}_{-1.41}$

Table 3.11: 1352 Å Band Summed Fluxes

Target	Continuum (FEFU)	Blue Flux (FEFU Å)
RECX11	0.41 ± 0.19	$2.63^{+0.44}_{-0.44}$
RECX15	0.60 ± 0.24	$2.61^{+0.55}_{-0.55}$
V4046	4.20 ± 1.30	$68.79^{+2.98}_{-2.98}$
DMTAU	0.85 ± 0.37	$4.44^{+0.85}_{-0.85}$
DETAU	1.39 ± 0.49	$3.45^{+1.14}_{-1.14}$
HD135344B	1.35 ± 0.66	$8.33^{+1.51}_{-1.51}$
HNTAU	2.25 ± 0.89	$2.81^{+2.06}_{-2.06}$
DRTAU	18.61 ± 7.89	$11.32^{+18.08}_{-11.32}$
DKTAU	7.02 ± 7.00	$3.02^{+16.13}_{-3.02}$
DFTAU	4.85 ± 1.22	$7.62^{+2.80}_{-2.80}$
LKCA15	1.50 ± 1.30	$1.17^{+3.00}_{-1.17}$
GMAUR	3.89 ± 1.47	$1.15^{+3.39}_{-1.15}$

Table 3.12: 1390 Å Band Summed Fluxes

Target	Continuum (FEFU)	Blue Flux (FEFU Å)
RECX11	0.45 ± 0.19	$1.45^{+0.49}_{-0.49}$
RECX15	0.90 ± 0.26	$1.38^{+0.68}_{-0.68}$
V4046	4.00 ± 1.10	$33.69^{+2.86}_{-2.86}$
DMTAU	1.00 ± 0.43	$2.37^{+1.12}_{-1.12}$
DETAU	1.53 ± 1.13	$0.92^{+2.95}_{-0.92}$
HD135344B	2.39 ± 0.68	$1.59^{+1.77}_{-1.59}$
HNTAU	2.80 ± 0.90	$4.35^{+2.33}_{-2.33}$
DRTAU	26.17 ± 7.83	$0.20^{+20.37}_{-0.20}$
DKTAU	5.96 ± 4.65	$6.92^{+12.10}_{-6.92}$
DFTAU	5.75 ± 1.40	$4.75^{+3.65}_{-3.65}$
LKCA15	1.54 ± 1.11	$1.98^{+2.88}_{-1.98}$
GMAUR	3.80 ± 1.50	$0.71^{+3.89}_{-0.71}$

of exciting the v'=0 level of CO. The resulting (v'=0,v''=3) transition creates a band of emission at 1712 Å. Indeed, cursory analysis shows that there is sufficient flux in the observed C IV lines to produce these levels of emission. If I attribute all the excess flux in this band to C IV-pumped emission, I can use branching ratios to predict flux in the 1597 Å (0 - 1) and 1653 Å (0 - 2) bands. These flux values are also listed in Table 3.4.4. It is difficult to model these (0 - v'') transitions as I have done for the (14 - v'') bands. Investigation of the CO transition databases shows that some transitions in the (0 - v'') bands are misidentified. Better laboratory measurements will be necessary to resolve this issue.

3.4.5   Long Wavelength Emission in ACS/STIS spectra

Ingleby et al. (2009) studied CTTS spectra from the *HST* instruments ACS and STIS, and identified excess emission at $\sim$1600 Å, above an accretion continuum. However, the measurements of significant CO (0 - 3) λ1713 Å flux implies that there should be flux in the other (0 - v'') bands; the (0 - 0), (0 - 1), and (0 - 2) bands are all intrinsically stronger. Figure 3.25 shows a representative target in their sample; in the top panel the ACS data is plotted along with COS data convolved to the ACS resolution. The bottom panel shows the COS data as observed. A plethora of H_2 lines, as well as the CO (0 - 3) band emission, are seen. This would imply that some of the $\sim$1600 Å flux must be due to CO. With ACS's <100 resolving power, these lines would blend together, along with any electron-impact excited emission. Therefore, the method of Ingleby et al. (2009) should be re-applied to account for this; further modeling of these individual components can doubtlessly provide additional correlations with accretion.

Another notable aspect in the COS spectrum is the increase in flux between 1540 - 1660 Å, as well as 1700 - 1750 Å. The emission features at $\sim$1550 and 1640 Å are due to the magnetospheric shock C IV and He II, respectively. Of particular interest to these studies are the features at 1600 Å and >1715 Å. Photo-excited CO contributes to both, while photon and collisional excitation H_2 emits below 1650 Å; both processes correlate with accretion. Some CTTS's accretion rates exhibit great variability, and thus it should not be surprising to see this emission variability. The
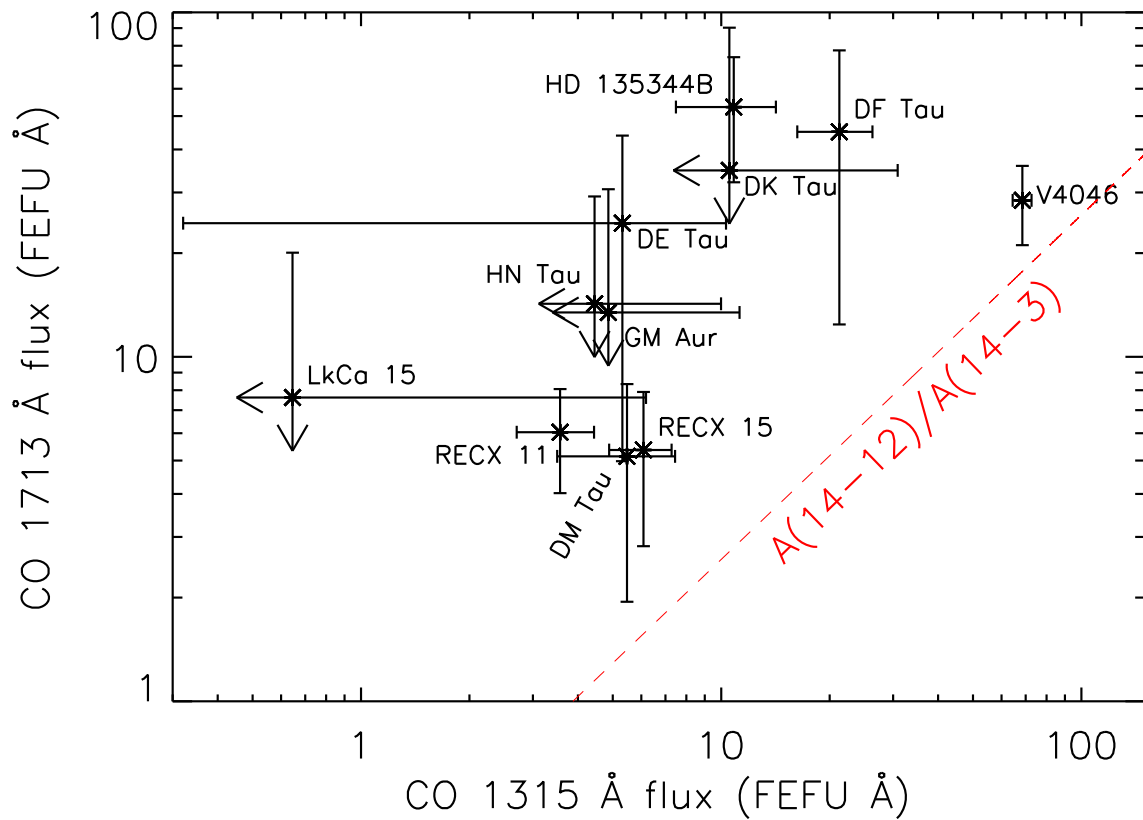
Figure 3.24: Summed fluxes for the 1713 Å band vs. the 1316 Å band, for each target. Arrows in place of an error bar indicate an upper limit for the value. The dashed red line shows the expected (14 - 12) flux expected from branching ratios for a given (14 - 3) flux.

Table 3.13: 1713 Å Band Summed Fluxes

Target	Continuum (FEFU)	14 - 12 (FEFU Å)	0 - 3 (FEFU Å)	0 - 1 (FEFU Å)	0 - 2 (FEFU Å)
RECX11	0.51 ± 0.31	$0.92^{+0.22}_{-0.22}$	$5.12^{+2.03}_{-2.03}$	$11.96^{+4.75}_{-4.75}$	$9.95^{+3.95}_{-3.95}$
RECX15	0.65 ± 0.39	$1.57^{+0.31}_{-0.31}$	$3.79^{+2.56}_{-2.56}$	$8.86^{+5.99}_{-5.99}$	$7.37^{+4.98}_{-4.98}$
V4046	3.62 ± 1.13	$17.70^{+1.06}_{-1.06}$	$10.77^{+7.44}_{-7.44}$	$25.16^{+17.39}_{-17.39}$	$20.91^{+14.46}_{-14.46}$
DMTAU	0.81 ± 0.49	$1.41^{+0.51}_{-0.51}$	$3.73^{+3.24}_{-3.24}$	$8.71^{+7.56}_{-7.56}$	$7.24^{+6.28}_{-6.28}$
DETAU	3.05 ± 2.99	$1.37^{+1.29}_{-1.29}$	$23.06^{+19.50}_{-19.50}$	$53.88^{+45.56}_{-45.56}$	$44.79^{+37.87}_{-37.87}$
HD135344B	12.20 ± 3.22	$2.80^{+0.86}_{-0.86}$	$50.31^{+21.02}_{-21.02}$	$117.55^{+49.11}_{-49.11}$	$97.72^{+40.82}_{-40.82}$
HNTAU	5.00 ± 2.29	$1.15^{+1.43}_{-1.15}$	$13.11^{+15.02}_{-13.11}$	$30.63^{+35.10}_{-30.63}$	$25.46^{+29.18}_{-25.46}$
DRTAU	27.74 ± 15.60	$0.00^{+14.63}_{-0.00}$	$74.62^{+102.79}_{-74.62}$	$174.36^{+240.17}_{-174.36}$	$144.94^{+199.65}_{-144.94}$
DKTAU	11.50 ± 8.51	$2.72^{+5.25}_{-2.72}$	$32.05^{+55.73}_{-32.05}$	$74.89^{+130.22}_{-74.89}$	$62.25^{+108.25}_{-62.25}$
DFTAU	13.32 ± 5.00	$5.49^{+1.29}_{-1.29}$	$39.50^{+32.60}_{-32.60}$	$92.29^{+76.17}_{-76.17}$	$76.72^{+63.32}_{-63.32}$
LKCA15	2.00 ± 1.91	$0.17^{+1.43}_{-0.17}$	$7.45^{+12.52}_{-7.45}$	$17.41^{+29.26}_{-17.41}$	$14.47^{+24.32}_{-14.47}$
GMAUR	5.35 ± 2.64	$1.25^{+1.65}_{-1.25}$	$12.20^{+17.29}_{-12.20}$	$28.50^{+40.40}_{-28.50}$	$23.69^{+33.58}_{-23.69}$

UV/Optical continuum, as well as Hα line emission, have been frequently used for this purpose; now with the combined high sensitivity and moderate resolution of COS, CTTS accretion can be further characterized.

3.5   Discussion

In addition to characterizing the temperature and column density of the UV-emitting CO, I wished to seek correlations with other previously measured properties of the CTTSs. What can be learned from the Lyα and CO fluxes. Can the UV CO be used as a unique diagnostic for CTTS disks? Do these best-fit Lyα profiles tell us anything new about these targets? Does this newly detected CO correspond with CO detected at other wavelengths? With these measurements of N_{CO} and T_{CO}, in concert with the observed CO fluxes, I can begin to answer these questions.

3.5.1   Observed Lyα and Band Fluxes

Summing the band fluxes as described in §3.4.4 gives us a check on the validity of these methods. The CO (14 - 3) and (14 - 4) summed blue fluxes are shown in Figure 3.26. Ideally, each point would fall on the red line, which shows the expected (14 - 4) flux for a given (14 - 3) flux. This is determined simply by the branching ratios between the two vibrational states. Branching ratios are defined by the ratio of the Einstein A coefficients for each ro-vibrational transition. After excitation by Lyα photons, CO that is in the v'=14 state of the upper A electronic level will decay down to ro-vibrational states of the X electronic level. The likelihood of the electron transitioning to a specific v" state depends on these A coefficients. These values are listed in Table 3.3. The band ratio is the ratio of an individual A coefficient and the sum of all A coefficients for the v'=14 transitions.

Thus the fact that most of the (14 - 3) fluxes fall below the red line means that there is less (14 - 4) flux than would be expected from standard molecular processes. Self-absorption could occur if the CO is optically thick. In this case any CO emission generated closer to the accretion shock would be absorbed by CO orbiting further away. I expect that the excess flux is due to the
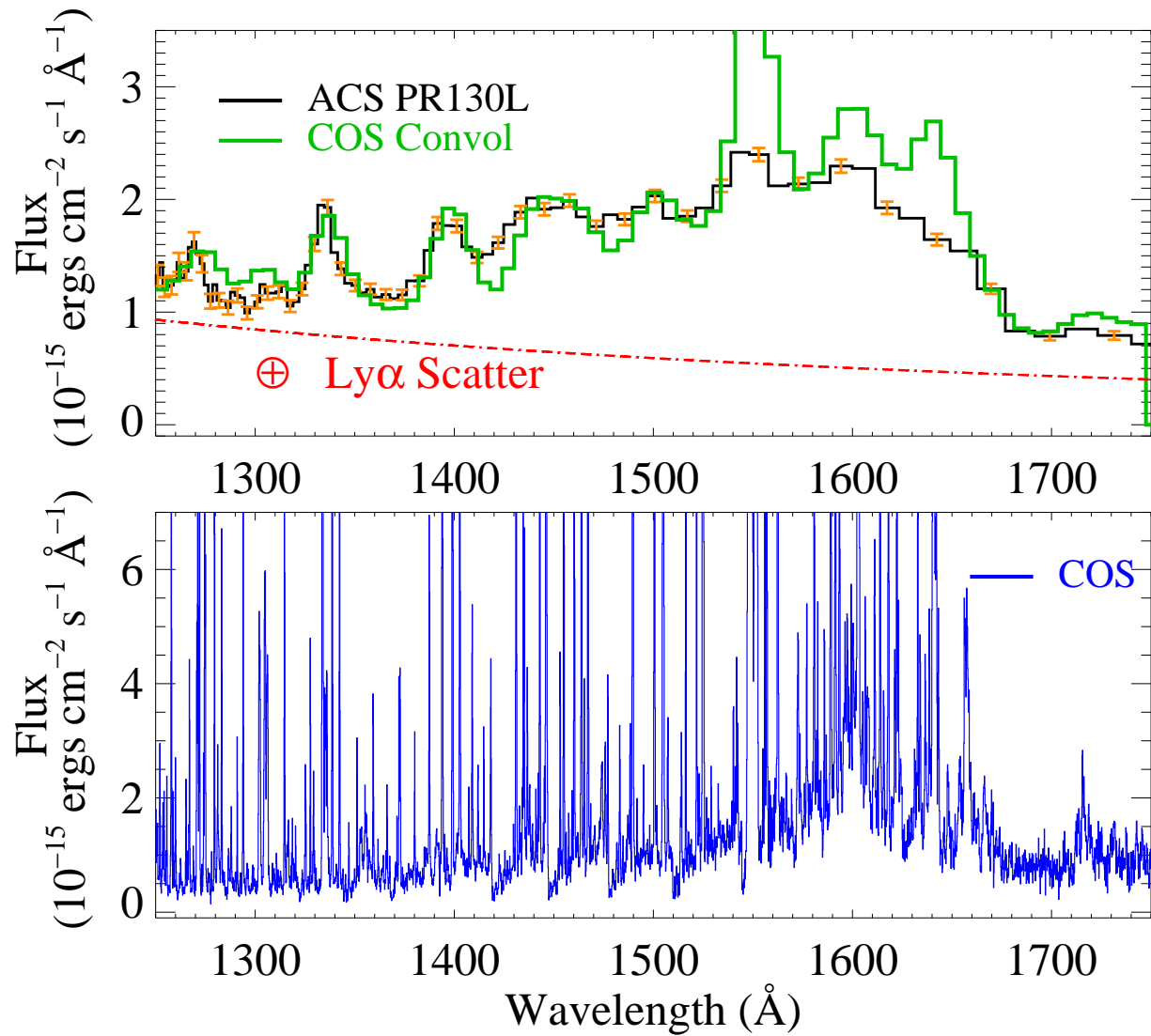
Figure 3.25: Top: ACS spectra and ACS-convolved COS spectra of a representative CTTS in the sample. Simulating Lyα scatter from the ACS grism was necessary to match the two spectrum. Bottom: COS spectra binned to two resolution elements.
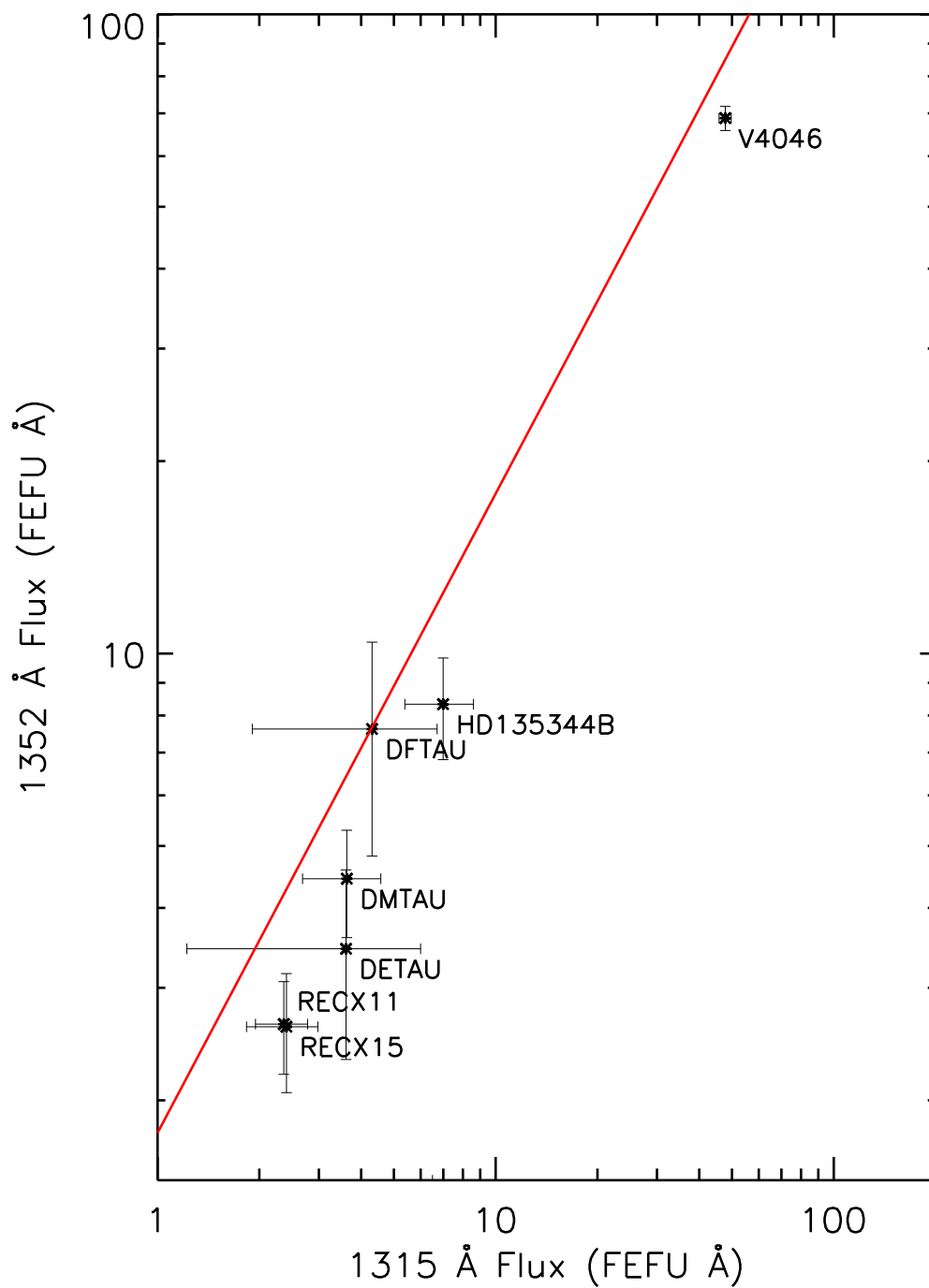
Figure 3.26: (14 - 4) band flux at 1352 Å vs. (14 -3) band flux at 1315 Å. The red line denotes the expected (14 - 4) flux based on the (14 - 3) band flux and branching ratios.

inclusion of the H_2 1316.55 Å emission line in the band summations. Further modeling of other H_2 lines would be necessary in order to quantify exactly how much this line contributes to the overall flux. This adds confidence to these methods that the CO emission I model is not further absorbed by any intervening CO.

I can also compare the observed CO band luminosities with the observed and modeled Lyα emission strength. Figure 3.27 shows both of these values versus the summed (14 - 3) band flux for each target. The Lyα luminosity is calculated by integrating the observed and model Lyα profiles and correcting for distance to each target. The five targets with lower limits of zero (14 - 3) band flux (GM Aur, DR Tau, DK Tau, LkCa 15, and HN Tau) are fixed at 10^{27} ergs s^{-1}. This is done to separate them from the targets with significant CO flux. For the CO detection targets the purely observed Lyα profiles, shown in Figures 3.3 and 3.4, correlate well with the (14 - 3) band flux. This in itself is somewhat surprising, as there should not necessarily be such a correlation; there is no physical reason why the combination of outflow and ISM material should absorb Lyα flux to result in this relation. Regardless, the correlation of model Lyα flux with CO emission is of course strong, as I use the (14 - 3) band profile to get Lyα profiles.

CTTS ages are difficult to estimate; the variety of initial conditions for star formations can lead to different properties (such as disk mass, size, and composition, SED properties, etc.) for two CTTSs of the same age. Noting the uncertainty in the age determination, the CO emission can be compared with the current range of ages available in the literature. This is shown in Figure 3.28. There is a slight trend towards more CO emission in older systems. V4046 Sgr, HD135344B, DM Tau, and GM Aur are all transitional objects with cleared holes in the center of their disks (Rodriguez et al., 2010; Brown et al., 2009; Calvet et al., 2005). DF Tau and DE Tau are outliers, but they have been known for their high accretion rates relative to their ages (Gullbring et al., 1998). Regardless, as of this analysis there appears to be a correlation between the UV-CO and age, with more CO UV emission appearing in more evolved systems.
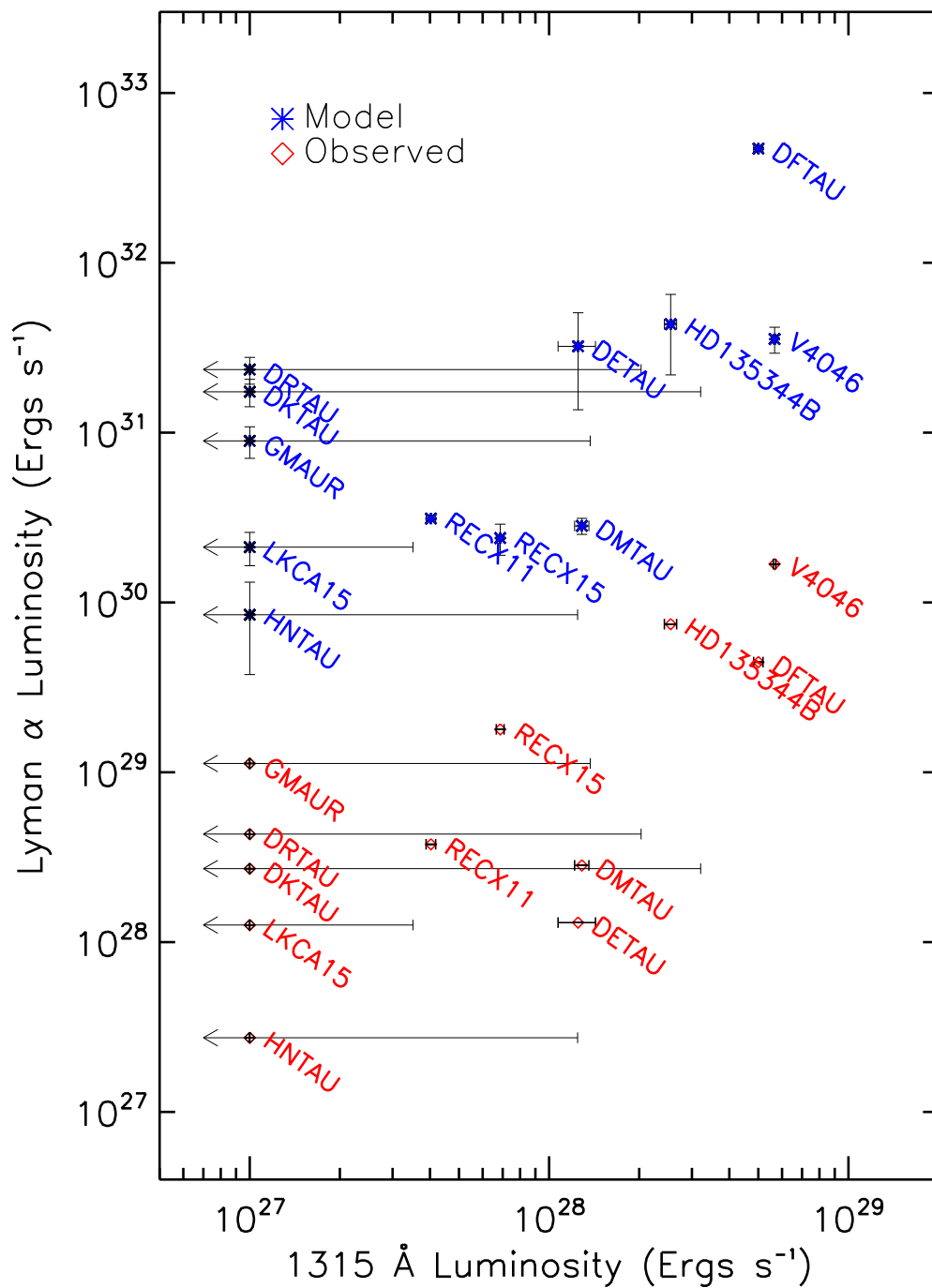
Figure 3.27: Distance-corrected summed fluxes for the Lyα profiles, vs. summed fluxes for the CO (14 - 3) band. Red is the summed data - only the result of outflow and ISM absorption. Blue is the full gaussian emission profile from the models. The CO "non-detections" are placed at 1x10^{27} Ergs s^{-1} with upper limit symbols to distinguish the positive detections in comparison with Lyα fluxes.
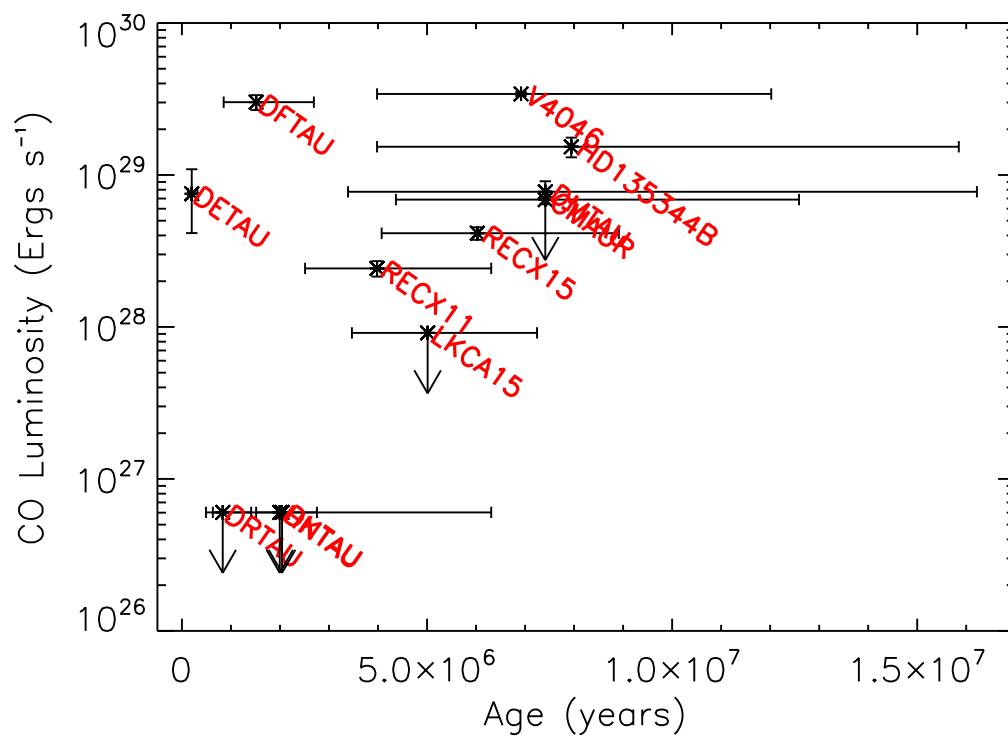
Figure 3.28: CO (14 - v") band luminosity vs. estimated ages. The CO luminosities were calculated by applying branching ratios to the (14 - 3) luminosities. Upper limits are placed on "non-detection" CO values.

3.5.2   Accretion Rate Correlations

The standard model of a CTTS disk includes a magnetospheric accretion shock near the surface of the protostar (Dullemond & Monnier, 2010). Disk material funnels along the star's magnetic field lines, compressing and heating up. As it does so it emits a strong FUV thermal continuum and hot gas emission lines. While the model for the Lyα profile may be oversimplified compared with the intrinsic line shape, the Lyα luminosity does correlate with accretion rates. These rates can be calculated from Hα profiles; the broader and brighter the emission, the higher the accretion rate. Veiling is another metric for accretion. Gas in the stellar atmosphere causes absorption lines, which can be "filled in" by the optical and UV continuum radiation created at the accretion shock. Thus the weaker the absorption lines are than expected, the higher the accretion rate. This is particularly useful in the case of the Paschen and Balmer continua (Gullbring et al., 1998). I find a best-fit linear correlation of:

$$\mathrm{L(Ly\alpha)}\ (10^{30}\mathrm{ergs\ s^{-1}}) = 2.58\pm0.01 + 17.73\pm0.35\mathrm{x}\dot{M}\ (10^{-8}\mathrm{M_\odot\ y}r^{-1})$$

with a correlation coefficient r of 0.83. The correlation between the modelled Lyα luminosity and these separately measured accretion rates lends credence to both the standard CTTS model and the overall method of analysis.

One might expect an increase in rotational temperature vs. accretion rate; higher accretion rates cause greater FUV continuum and Lyα emission, which in turn heats the gas to higher temperatures via photo-electric heating. The FUV photons could also populate higher J states in a way not possible by collisional processes alone. However, as seen in Figure 3.30, there appears to be no correlation between temperature and accretion rate. Temperatures for the non-detection targets were fixed at 300 K for their fitting procedure, and thus have no error bars. Over more than two orders of accretion rate magnitude, targets with strong CO and Lyα emission well constrain the temperature between 100 K and 500 K, with no apparent trend. This could be due to the distance of the CO from the star, but without more complicated modeling I have no reliable way of determining this. The calculated values for N_{CO} also do not appear to correlate with accretion
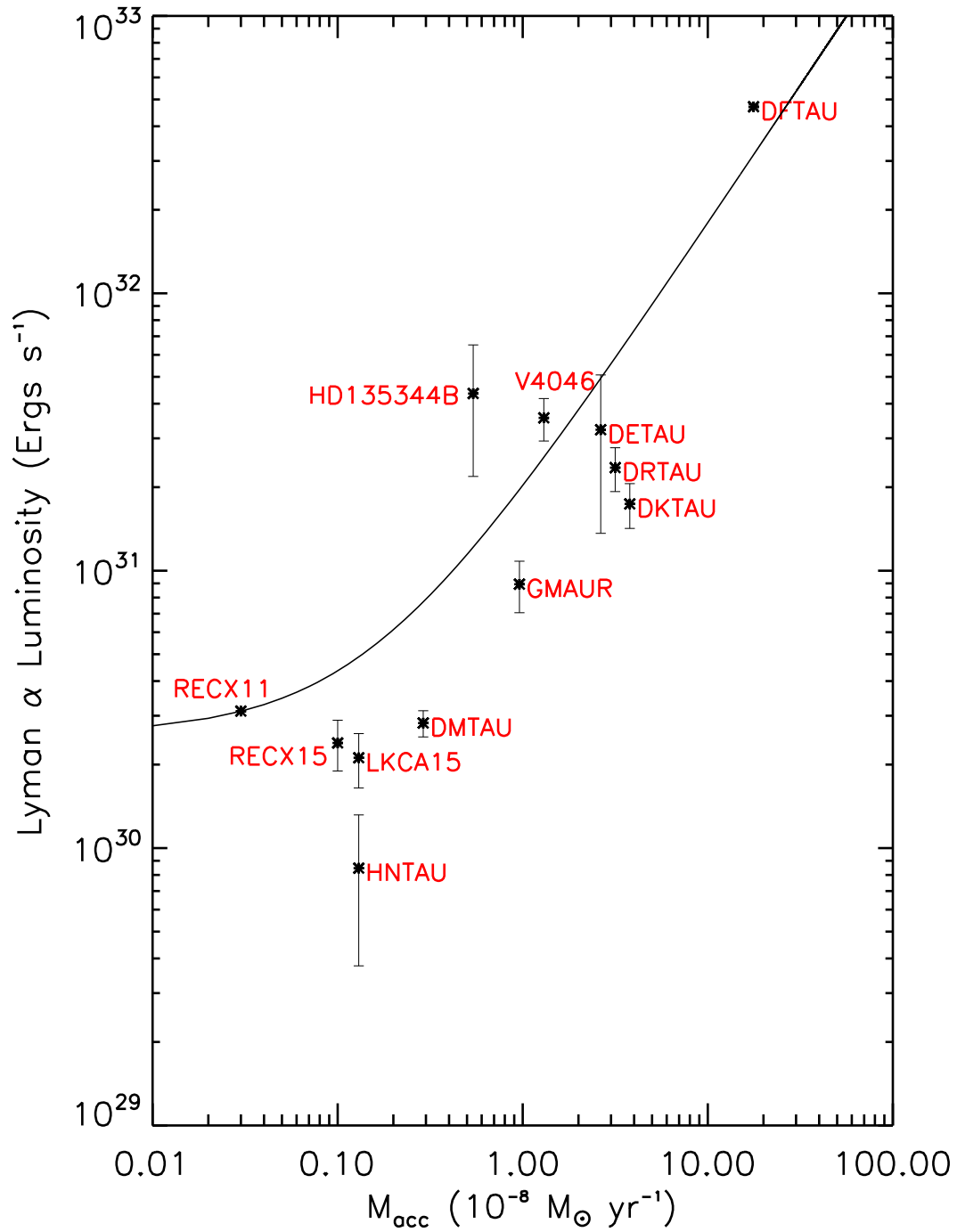
Figure 3.29: Model Lyα luminosites vs. accretion rates. The accretion rates are from literature sources, calculated by Hα emission and veiling measurements. The solid line indicates the best-fit linear correlation. The values and sources are listed in Table 3.2.

rates. Figure 3.30 shows this, with only N_{CO} upper limits shown for the non-detection targets.

In addition to integrating the CO Lyα pumped flux, I do the same with the H$_2$ pumped via the (1 - 2) P(5) transition at 1216.07 Å. I compute the total flux in this fluorescent progression by summing the H$_2$ (1 - 4) R(3) emission line at 1314.62 and multiplying by the branching ratio for the entire cascade from the (1 - 2) P(5) transition. The results are shown in Figure 3.31. I find a correlation of:

$$\text{L(CO) } (10^{28}\text{ergs s}^{-1}) = 4.33\pm0.22 + 2.75\pm0.19\text{x}\dot{M} \ (10^{-8}\text{M}_\odot \ yr^{-1})$$

with a correlation coefficient r of 0.45. The H$_2$ lines can be seen next to the CO (14 - 3) bands shown in Figures 3.3 and 3.4. These luminosities are representative of the amount of flux absorbed by CO and a fraction of the H$_2$ from the Lyα profiles. The correlation with accretion rate is not surprising, as the photo-exciting Lyα increases with accretion. Here it can be seen that the Lyα pumped H$_2$ emission is not vastly greater than that of the CO. It is certainly not at the level of multiple orders of magnitude, as one might expect from ISM CO/H$_2$ ratios (10^{-4}, Lacy et al. (1994)
.

Further investigation is necessary to understand this. The rest of the Lyα pumped H$_2$ transitions must be measured and modeled with the same method I have used with the CO. Only then can a self-consistent comparison be made between the two populations. With a combined knowledge of CO and H$_2$ emission, as well as the modeled Lyα profiles, the actual ratio between total column densities should be determinable. Figure 3.31 is illustrative of the relation between the UV emitting CO and H$_2$, but complete analysis of all emission features is required to better constrain the locations and physical conditions in the CO and H$_2$ populations responsible for UV emission.

3.5.2.1 A_V vs. N_H

Bohlin et al. (1978) sought an empirical relation between neutral hydrogen and color excess throughout the ISM. They obtained N_H by measuring the Lyα profile to 100 stars. Their targets
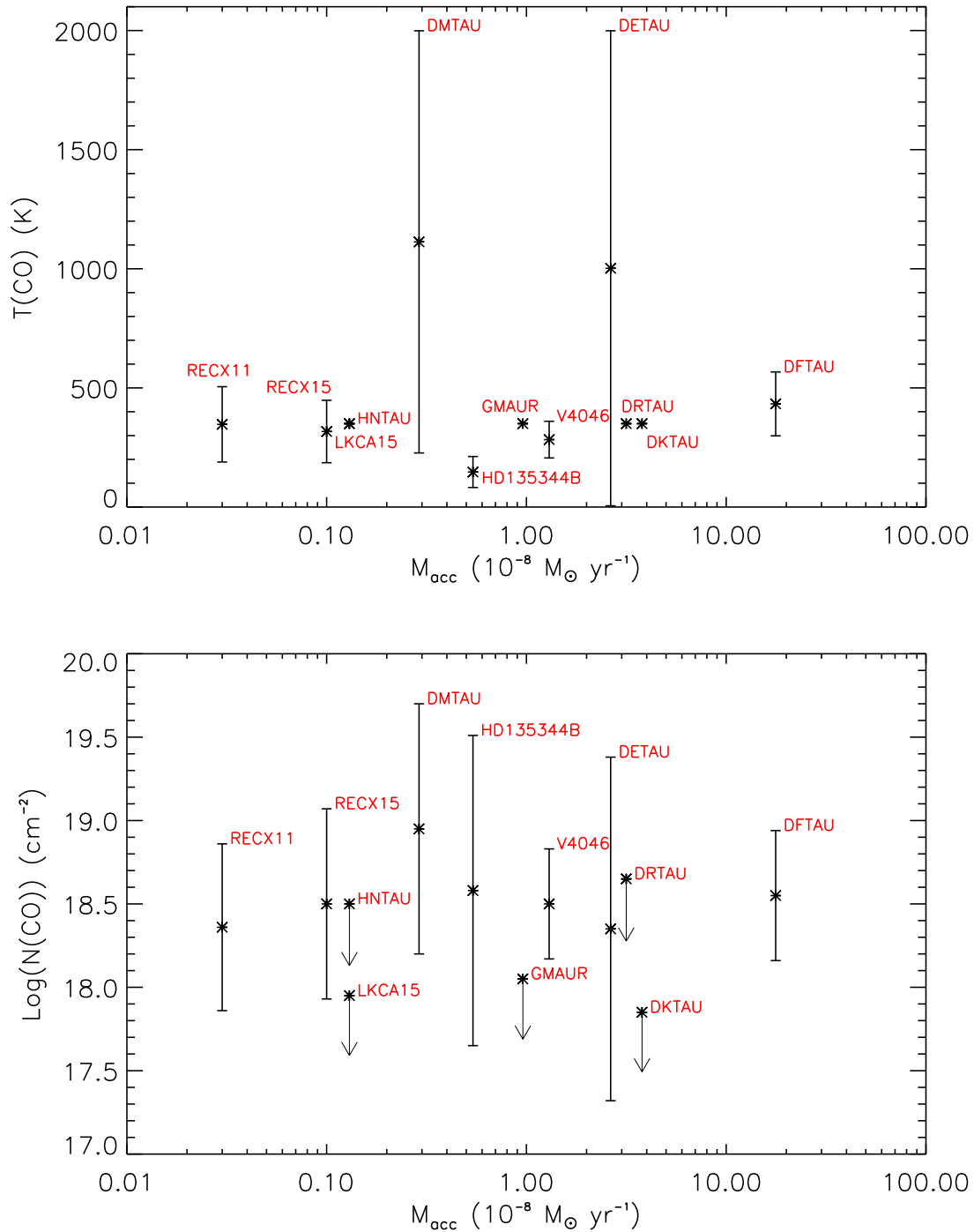
Figure 3.30: Model-derived T_{CO} and N_{CO} vs. accretion rates. T_{CO} for "non-detection" targets were fixed at 300 K, and only upper limits are placed on their N_{CO} values.

Figure 3.31: Luminosities of CO and H_2 transitions vs. accretion rates. The CO luminosities were calculated by applying branching ratios to the (14 - 3) luminosities. I sum the H_2 (1 - 4) R(3) emission line at 1314.62 Å and then apply the branching ratio to the (1 - 2) P(5) line which aborbs Lyα photons at 1216.07 Å. A linear correlation fit to the data is shown in black.

were bright, hot main sequence stars, so no outflow absorption was present. Including molecular and atomic hydrogen, they found the relation $< N(HI + H_2)/E(B-V) >= 5.8$ x 10^{21} atoms cm^{-2} mag^{-1}. For only H I, the relation was 4.8 x 10^{21} atoms cm^{-2} mag^{-1}. The fits of Lyα yield a range of possible values for the N_H towards each target. In Figure 3.32 I plot these values versus the A_V values used for analyzing each target. As $E(B-V)$ is simply A_V/R_V, I plot both of the Bohlin relations for $R_V = 4$, the value I used to de-redden the data.

DM Tau is the only target which falls to the left of the Bohlin relation; recent measurements of A_V for this target are approximately 0.5 (Calvet et al., 2005), but I used the original value of 0 from Kenyon & Hartmann (1995) for consistency between targets. Regardless, a trend of lower N_H for a given extinction is seen, relative to the standard interstellar relation. There are several possibilities in explaining this. A_V is notoriously difficult to measure for a CTTS, and its unreliability can have effects on other derived CTTS parameters such as extinction (Gullbring et al., 1998). Excess dust emission in the IR, as well as veiling in the UV and optical, can confuse attempts to identify the actual stellar blackbody. Due to the complex effects of disk evolution on the SED, it is difficult to quantify the amount of excess emission. Another cause could be a higher concentration of dust at a given N_H, due to the collapse of interstellar material.

3.5.3   Comparison with M-band observations

It is important to compare the UV-emitting CO with the CO observed in other wavebands, namely the infrared. The first M-band fundamental emission (v'=1,v"=0) has been seen in several of these targets (Najita et al., 2003). Table 3.14 lists information about the UV and IR detections for the target sample. Sorted by the strength of the Lyα pumped UV emission, I identify which targets show the UV (0 - 3) band emission, as well as whether or not M-band data has been collected. In addition to the fundamental emission, I list any detections of higher v transitions. These higher v levels are typically only identifiable when there is significant fundamental emission and high S/N. For the CO to be in these high v states, the gas must be collisionally excited at high temperature, or photo-excited (Bast et al., 2011).
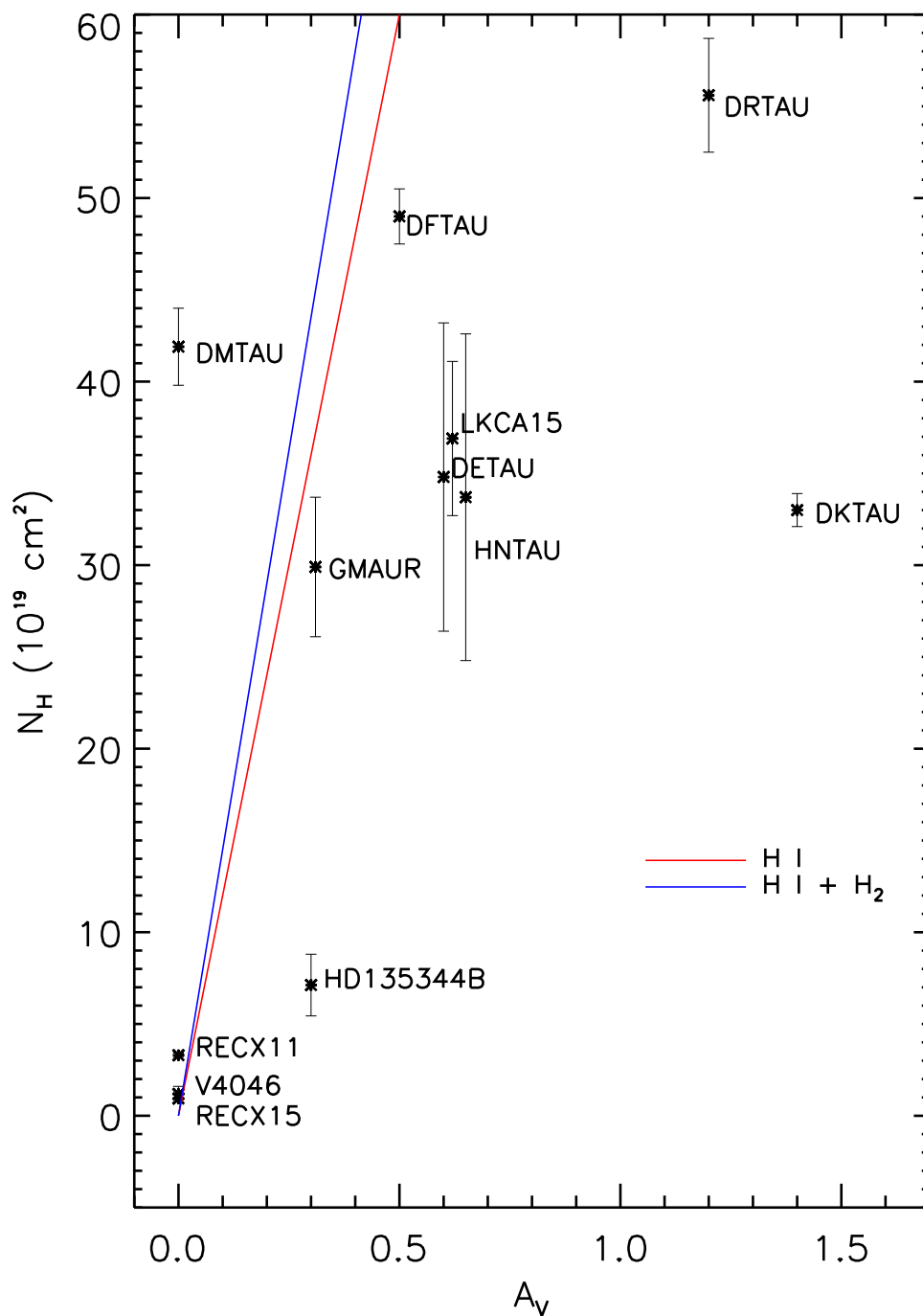
Figure 3.32: N_H values of ISM absorbing column from the Lyα models vs. A_V. Average N_H is calculated from the range of Lyα fits which produced the end set of CO profiles. A_V values are taken from the literature, listed in Table 3.2. The red and blue line are the N_H/A_V relations from Bohlin et al. (1978), for absorption from H I, as well as H I + H_2 respectively.

Photo-excitation could be responsible for populating these upper states. If so, then the M-band spectrum expected from the Lyα induced level populations can be determined. This may be difficult to detect above strong rovibrational emission due to thermal population, but in the high S/N targets it could be possible. These components are typically warm, at temperatures ranging from 500 K to 1000 K (Salyk et al., 2009; Bast et al., 2011; Najita et al., 2003). However, the photo-excited CO appears to be at lower temperatures, implying that the gas could be spatially separate. DM Tau and DE Tau have the highest temperatures in the sample, and yet these two targets show little or no M-band CO emission (Salyk et al., 2009; Greaves, 2005). DR Tau exhibits strong IR emission, but no noticeable UV emission (Salyk et al., 2008). There is much non-CO absorption in the DR Tau UV spectrum, making it difficult to understand this disparity.

Another oddity is the bias of the IR surveys; the targets were chosen for their bright M-band emission (Najita et al., 2003). This M-band emission usually correlates with accretion rates, as it is the UV continuum which pumps the CO, leading to the vibrational IR emission. However as I have shown, the CO UV emission correlates strongly with accretion as well. Therefore the lack of correlation between both emission processes must be explained. LyA pumped CO emission in the UV may also be tied to a lack of strong winds as neutral hydrogen opacities may otherwise be too high for the Lyα to reach the disk surface. In cases where the inclination is high, CO absorption of the UV continuum gives a line-of-sight quantification of the amount of input light into the cascade. With the current observations there is not enough information to explain such inconsistencies. More targets will be observed with COS, and proposals have been submitted to complete the survey of M-band data. With this complete set of data we should be able to begin to resolve these issues.

Table 3.14: 1713 Å CO UV/IR Detections

Target	Lyα CO	(0-3) CO	M data	M (1 - 0)	M (v' > 1)
V4046	Strong	yes	no	N/A	N/A
DF Tau	Strong	weak	NIRSPEC+CRIRES	Strong	strong
RECX15	Strong	yes	no	N/A	N/A
DM Tau	Strong	weak	NIRSPEC	No	no
RECX11	Intermediate	yes	no	N/A	N/A
DE Tau	Intermediate	yes	NIRSPEC	weak	no?
HD135344B	Intermediate	yes	NIRSPEC+CRIRES	yes	no
HN Tau	no	yes	NIRSPEC	weak	?
DR Tau	no	no	NIRSPEC+CRIRES	Strong	yes
DK Tau	no	no	NIRSPEC	yes	?
LkCa15	no	no	NIRSPEC	yes	no?
GM Aur	no	weak	NIRSPEC	weak(?)	no

Chapter 4

Conclusions

I've been pleased to work with so many wonderful stars through the years. This has been an amazing journey. I hope it continues.

-Keanu Reeves

In this thesis I have explored the phases of the ISM with FUV spectroscopy, both by developing a research program for a sounding rocket instrument, and by analyzing *HST*-COS data. I designed, assembled, calibrated and launched an instrument capable of high resolution FUV spectroscopy; while it was not succesful in obtaining useful science data, it is still a useful advancement of technology for studying ISM gas. In addition, I have examined CO emission in CTTSs, introducing new observational tests for current models of gas in protoplanetary disks.

4.1 DICE: Lessons Learned and Future Applications

I have presented a new instrument for measuring O VI absorption in the ISM. My goal was to achieve simultaneous high spectral resolution and throughput. The spectrograph efficiency surpasses that of an echelle mount, while accomplishing higher resolution than a Rowland mount system of a similar size. The use of holographically-ruled grooves decreases the scatter seen in a typical echelle, or a mechanically-ruled Rowland mount grating. This results in higher S/N for any scientific application. I have proved that a holographic grating solution can correct for the coma induced by the addition of a second optic into a Rowland mount spectrograph. Forcing the

magnifying optic to be spherical greatly increases ease of both fabrication and alignment. Removing constraints on astigmatism provided an additional metric for the alignment process.

Throughout the process of design and implimentation of DICE, I learned much that can be applied towards future developments of similar technology. I discovered that the physical size of the slit was the major limitation to resolution in this instrument, for a desired throughput. This could be mitigated by redesign of the slit mounting system, or utilizing a larger payload diameter to enable a larger telescope in front of the spectrograph. Future designs would benefit from a larger spectrograph entrance aperture. During optimization, I found that one of the major limiting factors of obtaining our desired spectral resolution was that of alignment tolerances. The three point spring mounts could only be adjusted manually by rotating the screws. Therefore the number of threads determined the amount of piston for a given screw rotation. A more complicated mounting system capable of finer position control would loosen such constraints on design.

Optical solutions similar to that of DICE would benefit future space-based observing platforms. The narrow bandpass lends itself to single experiments on sounding rockets, where only one or several atomic/molecular transitions can be studied. Larger diameter skins are an option for sounding rockets, thus a larger telescope is a possibility. Further design modifications utilizing a manipulable grating and/or magnifier could broaden the available bandpass for a general satellite mission. A holographic solution should be sought which would enable spectral focus over a larger bandpass by simply rotating the optics. With continued observing time, a satellite could accomodate less collecting area and hence an even smaller instrument. This option of a magnifying secondary spectrograph optic would enable high resolution in such a compact payload.

I have demonstrated the utility of wavelength-specific merit functions in the optimization of holgraphic recording source placement. During the optimization process it was clear that solutions could be found with varying spectral resolution over the bandpass; if the particular science requirements for an instrument design allow for lower resolutions in certain wavelength ranges, my numerical optimization tool can take this into account. Even higher spectral resolution will be possible when this technique is combined with detectors capable of higher spatial resolution and

coverage. Current MCP technology has demonstrated spatial resolutions as small as $\sim 17 \ \mu$m over a surface area of 47 mm, with potential for expansion to 100 mm (Vallerga et al., 2010). In addition, Apogee back illuminated CCDs can achieve pixels as small as $\sim 10 \mu$m over a 36mm surface area.

This instrument will be modified and re-flown as the Sub-orbital Local Interstellar Cloud Experiment (SLICE) in March 2012 and November 2012. Several more bright stars will be observed over the two flights, sampling additional sightlines through the ISM with an unsurpassed accuracy. There are many additional applications of this instrument, or one similarly designed, in the field of Astrophysics. This capability presents an excellent opportunity to study the different phases of the ISM with high resolution spectroscopy over a narrow bandpass. Of relevance to my CTTS studies, the DICE spectrograph equipped with a larger telescope could be used to measure H_2 absorption of O VI, as well as CO E - X and C - X emission.

Another important area in astrophysics is the Deuterium/Hydrogen (D/H) ratio. The deuterium produced during the Big Bang has slowly been reprocessed in stars, however just how much is still unanswered. Quantifying the D/H ratio at different epochs therefore places additional constraints on the Big Bang model. One of *FUSE*'s main goals was the measurement of the D/H ratio; however, even in many galactic targets, the Hydrogen lines are saturated, making it difficult to accurately determine column densities. Higher order lines of the Hydrogren Lyman series may be unsaturated, but were too narrow for *FUSE* to resolve. An optical solution similar to DICE, but in the waveband of these higher order Lyman lines, could resolve these lines and simultaneously measure Deuterium abundances.

One final problem that could be addressed with DICE-like resolution is the CO/H_2 ratio. As discussed previously, H_2 does not emit strongly so as to be detected from the ground, therefore CO is a commonly used tracer of interstellar and intergalactic gas. However, as the CO/H_2 ratio varies greatly in different environments, it is an unreliable metric for determining H_2 abundances. With high resolution FUV spectroscopy of short bandpasses, particularly around the 1088 CO lines, it would be possible to simultaneously measure CO and H_2 absorption along multiple sightlines. This would allow further characterization of CO in a variety of interstellar environments, strengthening

the utility of the CO/H_2 ratio in determining molecular mass elsewhere.

There are no current or proposed missions capable of such observations, making DICE and its unique optical design of great benefit to the astrophysics community as a whole.

4.2   The Present and Future of Molecular UV Emission in T Tauri Stars

In this study, I have characterized UV photo-excited CO emission in a sample of T Tauri stars. A simple model for the incident Lyα radiation field adequately reproduces the observed Lyα profile. My modeled profiles correlate with known accretion rates, agreeing with the overall picture that such radiation is produced at the funnel flow of a magnetospheric accretion shock. With this model for the Lyα emission and the assumption that the CO sees the same absorbing outflow H I column that the instrument does, I modeled the resulting CO (14 - v") bands. Both strong Lyα and CO emission are required in order to constrain N_{CO} to within 0.5 dex. Even so, these values are orders of magnitude greater than those expected from measured H_2 abundances and interstellar CO/H_2 ratios. These results prompt a number of future investigations.

Our measured CO temperatures differ from those of H_2 measured in previous studies by a factor of a few (Herczeg et al., 2002, 2004). This would imply that the CO is not co-spatial with the H_2, but further analysis is required to paint a detailed picture of the actual physical situation. Unfortunately, COS's moderate resolution blends together the individual CO low J lines, hiding information about the exact line widths. Such widths could constrain radial position of the gas, assuming the broadening is due to orbital velocity. However, H_2 shows a plethora of emission lines throughout its Lyman and Werner bands. There are some lines which are excited by Lyα in the same way as the CO we have studied (Yang et al., 2011). Unlike the CO, individual low J transitions are separated, yielding greater line width information about the H_2.

The H_2 emission must be analyzed in detail; fitting individual lines can determine which transitions are thermalized. For those lines that are, we can then create an independent check on the Lyα profiles from our CO analysis. If the Lyα profiles match, it would imply that both the CO and H_2 see the same incident radiation field. This would not necessarily mean the two are

co-spatial; if one is optically thin the other can be as far away as possible. However, this distance would be limited by the gas temperature and line widths. Further away from the star, a thermalized gas would be at lower temperatures. Also, the maximum width of a line provides an inner limit on the gas orbital radius. The combination of H_2 and CO analysis of these targets will help to constrain our overall understanding of the disk gas.

We also sought a way in which the UV-CO could act as a diagnostic of CTTS properties. We found that CO emission increases with both accretion rate and age. Combining our observational picture with models of inner disks, the UV-CO emission could be a useful indicator of disk evolution. In addition, we identified emission variance in several target spectra, when compared with spectra taken with ACS and STIS. As the UV variance of disk material corresponds directly to the accretion process, further comparison of these data between epochs can quantify the relation between the forming star and its disk. In addition to the electron and photo-excited H_2, calculations aimed at constraining the mass surface density of planet-forming disks (Ingleby et al., 2009) must be adapted to include the C IV-pumped (0 - v") band emission. This will be challenging, as the line databases for the (0 - v") bands are not as accurate as the (14 - v") bands. Some lines are misidentified; new laboratory measurements would be beneficial for this work.

Future observations will extend our study at several wavelengths. Ongoing COS observing programs will double the size of the disk sample presented in this thesis, and the new targets will be characterized in the same manner as this study. Some of the new targets, as well as several from this study, have not yet been observed in the IR. Proposals are currently under way to collect M-band CO data for these targets with CRIRES, an IR echelle spectrograph on the Very Large Telescope, as well as NIRSPEC on Keck. UV-emitting CO does not seem to correlate with the infrared-emitting CO. With a complementary set of UV and IR data, we will explore this relationship in order to better understand the physical parameters that govern each process. It will be necessary to model the IR emission spectrum expected from the cascade of Lyα excited CO. Sub-mm/mm-band imaging can also complement the UV-IR studies. With the advent of ALMA, high resolution images of the high-J CO transitions can be compared with shorter wavelength emission studies.

Overall, my studies of UV-emitting CO have changed our understanding of the warm molecular gas in protoplanetary disks. We now know that some disks do possess UV-emitting CO, which is photoexcited by accretion shock emission such as Lyα and C IV. It is measured at temperatures between $\sim$200 and 1000 K, and column densities of $\sim 10^{18}$ cm^{-2}. However, these results raise more questions than they answer. The disagreement of temperatures between the UV-CO, IR-CO, and UV-H$_2$ necessitates explanation from new modeling. My calculated N_{CO} values are of the same magnitude as the UV-emitting H$_2$, which strongly goes against observed dense cloud CO/H$_2$ ratios of $\sim 10^{-4}$ to 10^{-3}. However, it is as of yet unknown as to what this implies about the total molecular mass of the disk. The UV-emitting CO and H$_2$ could be a separate population from the majority of the gas in the disk. Again, further modeling and invesigation is required in order to solve these mysteries.

Bibliography

Akeson, R. L., et al. 2005, ApJ, 635, 1173

Andre, P., Ward-Thompson, D., & Barsony, M. 1993, ApJ, 406, 122

Andrews, S. M., & Williams, J. P. 2005, ApJ, 631, 1134

—. 2007, ApJ, 659, 705

Andrews, S. M., Wilner, D. J., Hughes, A. M., Qi, C., & Dullemond, C. P. 2009, ApJ, 700, 1502

Ardila, D. R., Basri, G., Walter, F. M., Valenti, J. A., & Johns-Krull, C. M. 2002, ApJ, 566, 1100

Artemenko, S. A., Grankin, K. N., & Petrov, P. P. 2010, Astronomy Reports, 54, 163

Barstow, M. A., Boyce, D. D., Barstow, J. K., Forbes, A. E., Welsh, B. Y., & Lallement, R. 2009, Ap&SS, 320, 91

Barstow, M. A., Boyce, D. D., Welsh, B. Y., Lallement, R., Barstow, J. K., Forbes, A. E., & Preval, S. 2010, ApJ, 723, 1762

Bary, J. S., Weintraub, D. A., & Kastner, J. H. 2003, ApJ, 586, 1136

Bast, J. E., Brown, J. M., Herczeg, G. J., van Dishoeck, E. F., & Pontoppidan, K. M. 2011, A&A, 527, A119+

Beasley, M., Boone, C., Cunningham, N., Green, J., & Wilkinson, E. 2004, Appl. Opt., 43, 4633

Beckwith, S. V. W., Sargent, A. I., Chini, R. S., & Guesten, R. 1990, AJ, 99, 924

Bergin, E., et al. 2004, ApJ, 614, L133

Bergin, E. A., et al. 2010, A&A, 521, L33+

Berkhuijsen, E. M., Haslam, C. G. T., & Salter, C. J. 1971, A&A, 14, 252

Bohlin, R. C., Savage, B. D., & Drake, J. F. 1978, ApJ, 224, 132

Bowyer, C. S., Field, G. B., & Mack, J. E. 1968, Nature, 217, 32

Brandeker, A., Jayawardhana, R., Khavari, P., Haisch, Jr., K. E., & Mardones, D. 2006, ApJ, 652, 1572

Brown, J. M., Blake, G. A., Qi, C., Dullemond, C. P., Wilner, D. J., & Williams, J. P. 2009, ApJ, 704, 496

Brown, J. M., et al. 2007, ApJ, 664, L107

Burgh, E. B., France, K., & McCandliss, S. R. 2007, ApJ, 658, 446

Burgh, E. B., McCandliss, S. R., Pelton, R., France, K., & Feldman, P. D. 2001, in Presented at the Society of Photo-Optical Instrumentation Engineers (SPIE) Conference, Vol. 4498, Society of Photo-Optical Instrumentation Engineers (SPIE) Conference Series, ed. O. H. Siegmund, S. Fineschi, & M. A. Gummin, 296–302

Calvet, N., & Gullbring, E. 1998, ApJ, 509, 802

Calvet, N., et al. 2005, ApJ, 630, L185

Cardelli, J. A., Clayton, G. C., & Mathis, J. S. 1989, ApJ, 345, 245

Chapman, N. L., Mundy, L. G., Lai, S., & Evans, N. J. 2009, ApJ, 690, 496

Chiang, E. I., & Goldreich, P. 1997, ApJ, 490, 368

Chol Minh, Y. C. Y., Kim, H., Lee, Y., Park, H., Kim, K., Park, Y., & Joon Kim, S. 2003, NA, 8, 795

Costa, V. M., Lago, M. T. V. T., Norci, L., & Meurs, E. J. A. 2000, A&A, 354, 621

Cox, D. P. 2005, ARA&A, 43, 337

Cox, D. P., & Reynolds, R. J. 1987, ARA&A, 25, 303

Cravens, T. E. 1997, Geophys. Res. Lett., 24, 105

—. 2000, ApJ, 532, L153

Cravens, T. E., Robertson, I. P., & Snowden, S. L. 2001, J. Geophys. Res., 106, 24883

D'Alessio, P., Canto, J., Calvet, N., & Lizano, S. 1998, ApJ, 500, 411

Dullemond, C. P., & Monnier, J. D. 2010, ARA&A, 48, 205

Dutrey, A., Guilloteau, S., & Guelin, M. 1997, A&A, 317, L55

Dutrey, A., et al. 2008, A&A, 490, L15

Eiroa, C., et al. 2002, A&A, 384, 1038

Eisner, J. A., Hillenbrand, L. A., White, R. J., Bloom, J. S., Akeson, R. L., & Blake, C. H. 2007, ApJ, 669, 1072

Eisner, J. A., et al. 2010, ApJ, 718, 774

Espaillat, C., Calvet, N., Luhman, K. L., Muzerolle, J., & D'Alessio, P. 2008, ApJ, 682, L125

Espaillat, C., et al. 2010, ApJ, 717, 441

Fitzgerald, M. P. 1968, AJ, 73, 983

France, K., Yang, H., & Linsky, J. L. 2011a, ApJ, 729, 7

France, K., et al. 2011b, ArXiv e-prints

Freyberg, M. J., & Egger, R. 1999, in Highlights in X-ray Astronomy, ed. B. Aschenbach & M. J. Freyberg, 278–+

Friedman, S. D., Conard, S. J., Sahnow, D. J., & McGuffey, D. B. 1994, in Presented at the Society of Photo-Optical Instrumentation Engineers (SPIE) Conference, Vol. 2283, Society of Photo-Optical Instrumentation Engineers (SPIE) Conference Series, ed. S. Fineschi, 252–260

Frisch, P. C., Grodnicki, L., & Welty, D. E. 2002, ApJ, 574, 834

Fuchs, B., Breitschwerdt, D., de Avillez, M. A., Dettbarn, C., & Flynn, C. 2006, MNRAS, 373, 993

Furlan, E., et al. 2006, ApJS, 165, 568

Garcia Lopez, R., Natta, A., Testi, L., & Habart, E. 2006, A&A, 459, 837

Gautier, III, T. N., Rebull, L. M., Stapelfeldt, K. R., & Mainzer, A. 2008, ApJ, 683, 813

Ghez, A. M., White, R. J., & Simon, M. 1997, ApJ, 490, 353

Grady, C. A., et al. 2009, ApJ, 699, 1822

Greaves, J. S. 2005, MNRAS, 364, L47

Green, J. C., Sarlin, S. P., & Cash, W. C. 1993, in Presented at the Society of Photo-Optical Instrumentation Engineers (SPIE) Conference, Vol. 1945, Society of Photo-Optical Instrumentation Engineers (SPIE) Conference Series, ed. P. Y. Bely & J. B. Breckinridge, 484–487

Guilloteau, S., Dutrey, A., Piétu, V., & Boehler, Y. 2011, ArXiv e-prints

Gullbring, E., Calvet, N., Muzerolle, J., & Hartmann, L. 2000, ApJ, 544, 927

Gullbring, E., Hartmann, L., Briceno, C., & Calvet, N. 1998, ApJ, 492, 323

Haisch, Jr., K. E., Lada, E. A., & Lada, C. J. 2001, ApJ, 553, L153

Hartmann, L., Calvet, N., Gullbring, E., & D'Alessio, P. 1998, ApJ, 495, 385

Heiles, C., & Troland, T. H. 2003, ApJ, 586, 1067

Henry, R. C., Fritz, G., Meekins, J. F., Friedman, H., & Byram, E. T. 1968, ApJ, 153, L11+

Herbig, G. H. 1960, ApJ, 131, 632

Herczeg, G. J., & Hillenbrand, L. A. 2008, ApJ, 681, 594

Herczeg, G. J., Linsky, J. L., Valenti, J. A., Johns-Krull, C. M., & Wood, B. E. 2002, ApJ, 572, 310

Herczeg, G. J., Linsky, J. L., Walter, F. M., Gahm, G. F., & Johns-Krull, C. M. 2006, ApJS, 165, 256

Herczeg, G. J., Wood, B. E., Linsky, J. L., Valenti, J. A., & Johns-Krull, C. M. 2004, ApJ, 607, 369

Herzberg, G. 1950, Molecular spectra and molecular structure. Vol.1: Spectra of diatomic molecules, ed. Herzberg, G.

Hobbs, L. M. 1974, ApJ, 191, 381

Hughes, A. M., Wilner, D. J., Qi, C., & Hogerheijde, M. R. 2008, ApJ, 678, 1119

Hughes, A. M., et al. 2009, ApJ, 698, 131

Hunter, W. R., Mikes, T. L., Anstead, R. J., & Osantowski, J. F. 1971, Appl. Opt., 10, 2199

Hurwitz, M., Sasseen, T. P., & Sirk, M. M. 2005, ApJ, 623, 911

Inaba, S., & Ikoma, M. 2003, A&A, 410, 711

Indebetouw, R., & Shull, J. M. 2004, ApJ, 605, 205

Ingleby, L., et al. 2009, ApJ, 703, L137

Isella, A., Carpenter, J. M., & Sargent, A. I. 2010, ApJ, 714, 1746

Isella, A., Testi, L., Natta, A., Neri, R., Wilner, D., & Qi, C. 2007, A&A, 469, 213

Jelinsky, P., Vallerga, J. V., & Edelstein, J. 1995, ApJ, 442, 653

Jenkins, E. B. 1978, ApJ, 219, 845

—. 2002, ApJ, 580, 938

Jensen, E. L. N., & Akeson, R. L. 2003, ApJ, 584, 875

Jensen, E. L. N., & Mathieu, R. D. 1997, AJ, 114, 301

Johns-Krull, C. M., & Gafford, A. D. 2002, ApJ, 573, 685

Kastner, J. H., Zuckerman, B., Hily-Blant, P., & Forveille, T. 2008, A&A, 492, 469

Kenyon, S. J., & Hartmann, L. 1995, ApJS, 101, 117

Kobayashi, N., & Tokunaga, A. T. 2000, ApJ, 532, 423

Koutroumpa, D., Acero, F., Lallement, R., Ballet, J., & Kharchenko, V. 2007, A&A, 475, 901

Koutroumpa, D., Lallement, R., Kharchenko, V., & Dalgarno, A. 2009, Space Sci. Rev., 143, 217

Kraus, A. L., & Hillenbrand, L. A. 2009, ApJ, 704, 531

Kurucz, R. L. 1993, kurucz.harvard.edu

Lacy, J. H., Knacke, R., Geballe, T. R., & Tokunaga, A. T. 1994, ApJ, 428, L69

Lada, C. J. 1987, in IAU Symposium, Vol. 115, Star Forming Regions, ed. M. Peimbert & J. Jugaku, 1–17

Lada, C. J., & Wilking, B. A. 1984, ApJ, 287, 610

Lallement, R., Welsh, B. Y., Vergely, J. L., Crifo, F., & Sfeir, D. 2003, A&A, 411, 447

Lawson, W. A., Crause, L. A., Mamajek, E. E., & Feigelson, E. D. 2001, MNRAS, 321, 57

—. 2002, MNRAS, 329, L29

Lawson, W. A., Lyo, A., & Muzerolle, J. 2004, MNRAS, 351, L39

Lissauer, J. J., Hubickyj, O., D'Angelo, G., & Bodenheimer, P. 2009, Icarus, 199, 338

Lisse, C. M., et al. 1996, Science, 274, 205

Lorenzetti, D., Larionov, V. M., Giannini, T., Arkharov, A. A., Antoniucci, S., Nisini, B., & Di Paola, A. 2009, ApJ, 693, 1056

Luhman, K. L. 2004, ApJ, 617, 1216

Luhman, K. L., Allen, P. R., Espaillat, C., Hartmann, L., & Calvet, N. 2010, ApJS, 186, 111

Lupu, R. E., Feldman, P. D., Weaver, H. A., & Tozzi, G. 2007, ApJ, 670, 1473

Mamajek, E. E., Lawson, W. A., & Feigelson, E. D. 1999, ApJ, 516, L77

Marcy, G. W., & Butler, R. P. 1995, in Bulletin of the American Astronomical Society, Vol. 27, American Astronomical Society Meeting Abstracts, 1379–+

McCammon, D., & Sanders, W. T. 1990, ARA&A, 28, 657

McCammon, D., et al. 2002, ApJ, 576, 188

McKee, C. F., & Ostriker, E. C. 2007, ARA&A, 45, 565

Megeath, S. T., Hartmann, L., Luhman, K. L., & Fazio, G. G. 2005, ApJ, 634, L113

Men'shchikov, A. B., & Henning, T. 1997, A&A, 318, 879

Monin, J., Clarke, C. J., Prato, L., & McCabe, C. 2007, Protostars and Planets V, 395

Najita, J., Carr, J. S., & Mathieu, R. D. 2003, ApJ, 589, 931

Najita, J. R., Strom, S. E., & Muzerolle, J. 2007, MNRAS, 378, 369

Najita, J. R., et al. 2009, ApJ, 697, 957

Noda, H., Namioka, T., & Seya, M. 1974, Journal of the Optical Society of America (1917-1983), 64, 1031

Oegerle, W. R., Jenkins, E. B., Shelton, R. L., Bowen, D. V., & Chayer, P. 2005, ApJ, 622, 377

Osterman, S., et al. 2010, ArXiv e-prints

Perryman, M. A. C., et al. 1997, A&A, 323, L49

Piétu, V., Dutrey, A., & Guilloteau, S. 2007, A&A, 467, 163

Pontoppidan, K. M., Blake, G. A., van Dishoeck, E. F., Smette, A., Ireland, M. J., & Brown, J. 2008, ApJ, 684, 1323

Pontoppidan, K. M., Salyk, C., Blake, G. A., Meijerink, R., Carr, J. S., & Najita, J. 2010, ApJ, 720, 887

Pott, J., Perrin, M. D., Furlan, E., Ghez, A. M., Herbst, T. M., & Metchev, S. 2010, ApJ, 710, 265

Przygodda, F., van Boekel, R., Àbrahàm, P., Melnikov, S. Y., Waters, L. B. F. M., & Leinert, C. 2003, A&A, 412, L43

Quast, G. R., Torres, C. A. O., de La Reza, R., da Silva, L., & Mayor, M. 2000, in IAU Symposium, Vol. 200, IAU Symposium, 28P–+

Ramsay Howat, S. K., & Greaves, J. S. 2007, MNRAS, 379, 1658

Redfield, S. 2009, Space Sci. Rev., 143, 323

Redfield, S., & Linsky, J. L. 2008, ApJ, 673, 283

Ricci, L., Robberto, M., & Soderblom, D. R. 2008, AJ, 136, 2136

Ricci, L., Testi, L., Natta, A., Neri, R., Cabrit, S., & Herczeg, G. J. 2010, A&A, 512, A15+

Robertson, I. P., & Cravens, T. E. 2003, Journal of Geophysical Research (Space Physics), 108, 8031

Rodriguez, D. R., Kastner, J. H., Wilner, D., & Qi, C. 2010, ApJ, 720, 1684

Salyk, C., Blake, G. A., Boogert, A. C. A., & Brown, J. M. 2007, ApJ, 655, L105

—. 2009, ApJ, 699, 330

Salyk, C., Pontoppidan, K. M., Blake, G. A., Lahuis, F., van Dishoeck, E. F., & Evans, II, N. J. 2008, ApJ, 676, L49

Sargent, B. A., et al. 2009, ApJS, 182, 477

Sauter, J., et al. 2009, A&A, 505, 1167

Savage, B. D., & Lehner, N. 2006, ApJS, 162, 134

Sfeir, D. M., Lallement, R., Crifo, F., & Welsh, B. Y. 1999, A&A, 346, 785

Shelton, R. L. 1999, ApJ, 521, 217

Sicilia-Aguilar, A., et al. 2009, ApJ, 701, 1188

Smith, N., Bally, J., Licht, D., & Walawender, J. 2005, AJ, 129, 382

Snell, R. L., Carpenter, J. M., & Heyer, M. H. 2002, ApJ, 578, 229

Snowden, S. L., Egger, R., Finkbeiner, D. P., Freyberg, M. J., & Plucinsky, P. P. 1998, ApJ, 493, 715

Snowden, S. L., McCammon, D., & Verter, F. 1993, ApJ, 409, L21

Stempels, H. C., & Gahm, G. F. 2004, A&A, 421, 1159

Thalmann, C., et al. 2010, ApJ, 718, L87

Vallerga, J., Raffanti, R., Tremsin, A., Siegmund, O., McPhate, J., & Varner, G. 2010, in Society of Photo-Optical Instrumentation Engineers (SPIE) Conference Series, Vol. 7732, Society of Photo-Optical Instrumentation Engineers (SPIE) Conference Series

Vallerga, J., & Slavin, J. 1998, in Lecture Notes in Physics, Berlin Springer Verlag, Vol. 506, IAU Colloq. 166: The Local Bubble and Beyond, ed. D. Breitschwerdt, M. J. Freyberg, & J. Truemper, 79–82

van Boekel, R., et al. 2004, Nature, 432, 479

Vasyunin, A. I., Wiebe, D. S., Birnstiel, T., Zhukovska, S., Henning, T., & Dullemond, C. P. 2011, ApJ, 727, 76

Watson, A. M., & Stapelfeldt, K. R. 2004, ApJ, 602, 860

Watson, D. M., et al. 2009, ApJS, 180, 84

Watson, W. D. 1972, ApJ, 176, 103

Welsh, B. Y., & Lallement, R. 2008, A&A, 490, 707

Welsh, B. Y., Lallement, R., Vergely, J., & Raimond, S. 2010, A&A, 510, A54+

White, R. J., & Ghez, A. M. 2001, ApJ, 556, 265

Whittet, D. C. B., Gerakines, P. A., Hough, J. H., & Shenoy, S. S. 2001, ApJ, 547, 872

Williamson, F. O., Sanders, W. T., Kraushaar, W. L., McCammon, D., Borken, R., & Bunner, A. N. 1974, ApJ, 193, L133

Wolfire, M. G., McKee, C. F., Hollenbach, D., & Tielens, A. G. G. M. 1995, ApJ, 453, 673

Yang, H., Linsky, J. L., & France, K. 2011, ApJ, 730, L10+

Appendix A

Glossary of Terms

AU - Astronomical Unit

ACS - Advanced Camera for Surveys

Al - Aluminum

AMR - Adaptive Mesh Refinement

CHIPS - Cosmic Hot Interstellar Plasma Spectrometer

CNM - Cold Neutral Medium

CO - Carbon Monoxide

COS - Cosmic Origins Spectrograph

CTTS - Classical T-Tauri Star

EUV - Extreme Ultraviolet

EUVE - Extreme Ultraviolet Explorer

FEFU - Femto-Erg Flux Unit

FEM - Finite Element Modeling

FUV - Far Ultraviolet

FUSE - Far Ultraviolet Spectroscopic Explorer

GHRS - Goddard High Resolution Spectrograph

HST - Hubble Space Telescope

IUE - International Ultraviolet Experiment

IR - Infrared

ISM - Interstellar Medium

LB - Local Bubble

LC - Local Cavity

LiF - Lithium Fluoride

LHB - Local Hot Bubble

LISM - Local Interstellar Medium

LTE - Local Thermodynamic Equilibrium

MAST - Multimission Archive at STSci

MRI - Magneto Rotational Instability

NTTS - Naked T-Tauri Star

pc - parsec

ROSAT - Rontgen Satellite

SED - Spectral Energy Distribution

STIS - Space Telescope Imaging Spectrograph

SWCX - Solar Wind Charge Exchange

TDC - Time to Digital Converter

WNM - Warm Neutral Medium

WTTS - Weak-lined T-Tauri Star

UV - Ultraviolet

YSO - Young Stellar Object